INFORMATION TO USERS

This manuscript has been reproduced from the microfilm master. UMI films the text directly from the original or copy submitted. Thus, some thesis and dissertation copies are in typewriter face, while others may be from any type of computer printer.

The quality of this reproduction is dependent upon the quality of the copy submitted. Broken or indistinct print, colored or poor quality illustrations and photographs, print bleedthrough, substandard margins, and improper alignment can adversely affect reproduction.

In the unlikely event that the author did not send UMI a complete manuscript and there are missing pages, these will be noted. Also, if unauthorized copyright material had to be removed, a note will indicate the deletion.

Oversize materials (e.g., maps, drawings, charts) are reproduced by sectioning the original, beginning at the upper left-hand corner and continuing from left to right in equal sections with small overlaps.

Photographs included in the original manuscript have been reproduced xerographically in this copy. Higher quality 6" x 9" black and white photographic prints are available for any photographs or illustrations appearing in this copy for an additional charge. Contact UMI directly to order.

Bell & Howell Information and Learning
300 North Zeeb Road, Ann Arbor, MI 48106-1346 USA
800-521-0600

UMI®

Aeroelastic Oscillations of a Delta Wing with Bonded Piezoelectric Strips

by

Swapna Shrivastava

November 1998

A thesis submitted to the Faculty of Graduate Studies and Research in partial fulfilment of the requirements of the degree of Master of Engineering.

Department of Mechanical Engineering
McGill University
Montréal, Québec, Canada

Abstract

Piezoelectric materials offer an alternative method for active control of aeroelastic oscillations, that is potentially cheaper, lighter, and more effective than conventional control methods. In this thesis, the aeroelastic oscillations of a delta wing under the combined effects of unsteady, supersonic aerodynamic loading and bonded piezoelectric strips are studied.

The delta wing is modelled as a cantilevered triangular plate undergoing small transverse oscillations. Using the structural model developed here, the natural frequencies of the wing are obtained. A hybrid analytical-numerical method is developed for the unsteady supersonic aerodynamics of the wing, in order to determine the unsteady pressure distribution and the generalized aerodynamic forces on the wing. It is shown that the method adopted here to obtain the pressure distribution is more accurate than the analytical method based on *frequency expansion*, and computationally more efficient than the numerical methods using the *Mach Box* approach. Finally, in the presence of bonded piezoelectric strips, the transient and dynamic responses of the wing are studied without and with aerodynamic loading, respectively.

It is found that with particular combinations of voltages and the number of piezoelectric strips, the amplitude of the aeroelastic oscillations can be reduced. These required combinations change as the periodic frequency of wing oscillation is varied. Additionally, the piezoelectric actuators aligned with the span are more effective than the chord-aligned piezoelectric actuators, which produce little or no reduction in the oscillations. It is further found that even a small number of strips can effectively reduce the magnitude of the oscillations.

Sommaire

Les matériaux piézo-électriques offrent une méthode alternative pour la commande active des oscillations aéroélastiques. Cette méthode est potentiellement moins coûteuse, plus simple, et plus efficace que les méthodes de commande conventionnelles. Dans cette thèse, les oscillations aéroélastiques d'une aile delta sous les effets combinés des charges aérodynamiques non-stationnaires supersoniques et des bandes piézo-électriques sont étudiées.

L'aile delta est modélisée comme une plaque triangulaire en porte-à-faux soumise à des petites oscillations transversales. En utilisant le modèle structural développé ici, les fréquences naturelles de l'aile sont obtenues. Une méthode hybride analytique–numérique est développée pour l'aérodynamique supersonique non-stationnaire de l'aile, dans le but de calculer la distribution des pressions non-stationnaires, ainsi que les forces aérodynamiques généralisées sur l'aile. Il est montré que la méthode adoptée ici pour obtenir la distribution des pressions est plus exacte que la méthode analytique basée sur l'expansion des fréquences, et plus efficace du point du vue des calculs numériques que les méthodes *Mach Box*. Finalement, en présence des bandes piézo-électriques, les réponses dynamiques et transitoires de l'aile sont étudiées, sans et respectivement, avec les charges aérodynamiques.

On a trouvé qu'avec certaines combinaisons des voltages et des bandes piézo-électriques, l'amplitude des oscillations aéroélastiques peut être réduite. Ces combinaisons changent quand la fréquence périodique de l'oscillation de l'aile varie. De plus, les bandes piézo-électriques alignées dans la direction de l'envergure sont plus efficaces que celles alignées avec la corde, qui produisent très peu ou pas de réduction dans les oscillations. On trouve que même un très petit nombre des bandes piézo-électriques peut effectivement réduire l'amplitude des oscillations.

Acknowledgements

I wish to extend my sincere gratitude to my research supervisors, Prof. A. K. Misra and Prof. D. Mateescu, for their guidance, understanding, and support throughout the course of this program. I am grateful to them for providing full financial support which enabled me to pursue this degree.

I would also like to thank my supervisors at Bombardier Aerospace, past and present, Mr. Hany Sadek, Mr. Clinton Tanner, Mr. Anthony Linsdell and Mr. Arthur McClements, for their understanding and flexibility while I was finishing this thesis.

Thanks to my friend, Dr. Ruxandra Botez, for translating the English abstract of this thesis into French. I am also appreciative of Ms. Mary Fiorilli and Ms. Anna Cianci of the Department of Mechanical Engineering for their help with administrative details throughout my entire stay at McGill University.

I wish to express my heartfelt thank you to my parents, Prof. S. K. Shrivastava and Mrs. P. Shrivastava, and my brother, Prateek Shrivastava, for their love, support and encouragement without which I would not have been able to complete this thesis. Finally, I am grateful to my husband, Stephen Garrioch, for his help in editing this thesis, and thank him for his love and encouragement.

Table of Contents

Page

List of Figures

Page

Page

List of Tables

Nomenclature

a = speed of sound

a_i = width of ith piezoelectric strip polarized in y-direction

b_i = width of ith piezoelectric strip polarized in x-direction

c = chord of delta wing

$[C]$ = structural damping matrix

C_p = coefficient of pressure

$\hat{C}_p$ = reduced coefficient of pressure

d_{31} = piezoelectric constant relating voltage to strain for x-aligned PVDF strips

d_{32} = piezoelectric constant relating voltage to strain for y-aligned PVDF strips

D = flexular rigidity

E = Young's Modulus

f = shape function of PVDF strip polarized in x-direction

g = shape function of PVDF strip polarized in y-direction

h = small transverse motion of wing

h_i = thickness of the ith piezoelectric strip

h_p = thickness of the wing

$\hat{h}$ = small reduced transverse motion of wing

$[I]$ = unit matrix

k = non-dimensional frequency

K_i = gain

$[K]$ = stiffness matrix

l = length of semi-span of delta wing

L = Lagrangian

m = mass per unit area

M = number of clamped-free shape functions

$\overline{M}$ = Moment

M_∞ = free-stream Mach number

$[M]$ = mass matrix

N = number of free-free shape functions

p = pressure

P = power

$\{q\}$ = generalized displacements

$\{\tilde{q}\}$ = complex generalized displacements

$\{\dot{q}\}$ = generalized velocities

$\{\ddot{q}\}$ = generalized accelerations

$\{q_{rs}^{c}\}$ = cosine component of the generalized displacements

$\{q_{rs}^{s}\}$ = sine component of the generalized displacements

$\{Q_{aero}\}$ = generalized forces due to aerodynamic loading

$\{Q_{piezo}\}$ = generalized forces due to the presence of piezoelectric strips

R_t = total number of PVDF strips

R_x = number of PVDF strips aligned in the x-direction

R_y = number of PVDF strips aligned in the y-direction

t = time

T = kinetic energy

u = pertubation velocity

$\hat{u}$ = reduced pertubation velocity

U = stream velocity

V = potential energy

V_{ix} = voltage applied across the thickness of the ith strip oriented in the x-direction

V_{iy} = voltage applied across the thickness of the ith strip oriented in the y-direction

$\hat{V}_{ix}^{c}$ = cosine component of V_{ix}

$\hat{V}_{ix}^{s}$ = sine component of V_{ix}

$\hat{V}_{iy}^{c}$ = cosine component of V_{iy}

$\hat{V}_{iy}^{s}$ = sine component of V_{iy}

w = transverse displacement of the wing

$\overline{w}$ = vertical pertubation velocity or upwash

$\hat{w}$ = reduced vertical pertubation velocity

$\hat{W}$ = reduced vertical velocity

$y = x_2 / x_1$

(x, y) = coordinate-system used for structural modelling and dynamic analysis

(x_1, x_2) = coordinate-system used for aerodynamic analysis

(x_{1s}, x_{2s}) = source point

(x_i, y_i) = location of the bottom left corner of the ith PVDF strip

(X, Y) = non-dimensional coordinate-system used for aerodynamic analysis

α , β = plate material constants for damping

ε_l = longitudinal strain in the plate

ε_s = longitudinal strain in the piezoelectric strip

η = non-dimensional y-coordinate

ν = Poisson's ratio

ω_n = natural frequency

ω = frequency of periodic motion

φ = pertubation velocity potential

$\hat{\varphi}$ = reduced pertubation velocity potential

Φ_i = i^{th} clamped-free shape function

ρ = plate material density

$\hat{\psi}$ = small rolling rotation

Ψ_i = i^{th} free-free shape function

ξ = non-dimensional x-coordinate

θ = angular deflection

$\hat{\theta}$ = small pitching rotation

Subscripts

i = ith piezoelectric strip

p = plate

r = identifies shape function in the clamped-free direction

s = identifies shape function in the free-free direction

∞ = free airstream

Chapter 1

Introduction

Aeroelastic wing oscillations represent a major concern to the aircraft engineer. Vibrations from instabilities, such as flutter of wings, affect the maximum flight speed and the integrity of the aircraft. Flutter suppression is especially critical for supersonic wings and is a subject that has been studied extensively. At high speeds, flutter of the wings is greatly increased thereby increasing the risk of failure of the structure. Hence, control of this instability is very important in order to increase the flight envelope and improve the safety of the structure. Also, controlling aeroelastic oscillations helps provide smoother rides, and lower root loads.

Aeroelastic wing vibration can be controlled by both passive and active means. Passive control methods include: *static* and *dynamic mass balancing* on manual aircraft which involve use of high weight, low volume material placed in or on the control surfaces such as ailerons and elevators; use of more than two *power control units* on the control surfaces to provide stiffness; use of *flutter dampers* which involves a piston moving in hydraulic fluid to provide stiffness to the control surface; and *structural tailoring* of the wings, such as adjusting the geometric sweep. The problems associated with passive methods include added weight, hydraulic lags and cost. Conventional active control methods use the control surfaces of the wing as actuators. For example, advanced tailless fighter aircraft use ailerons as actuators. There are problems, however, associated with these active control methods. As the control surfaces are hydraulically operated, there is a hydraulic lag associated with conventional active control.

Present day researchers are looking at smart materials as an alternative to the conventional control surface actuation. These smart materials can control the oscillations due to flutter in supersonic wings by strain actuation. Smart materials like piezoelectric and piezoceramic materials are examples of strain actuators. These smart materials can easily be mechanically integrated on the surface of the wing in the form of thin layers or individual strips. They are lightweight, cheap, and easy to manufacture. Structures that incorporate these smart materials are called smart structures or adaptive structures.

As the title of the thesis suggests, the work presented herein is multi-disciplinary involving structural analysis of a delta wing, aerodynamic modelling, and lastly a combination of the two models to study the response of the delta wing under the combined aerodynamic and piezoelectric forces.

A survey of the available literature shows that work has been done around the world by researchers in one or more of the disciplines involved, namely, oscillations of wings, unsteady supersonic aerodynamics and active control of structures using piezoelectric materials. The available literature also shows that some work has been done in the field of flutter control of wings (for example swept-back wings) by means of smart materials using simple aerodynamic models. The author is unaware, however, of any literature on the subject of control of aeroelastic oscillations of a delta wing using smart materials.

In this thesis, the dynamic response of a delta wing under unsteady supersonic loading and in the presence of piezoelectric materials known as PVDF (polyvinylidene fluoride) is studied. Delta wings are wings of symmetrical triangular form used ordinarily on supersonic aircraft. For example, variations of the delta wing are found on the Concorde; military aircraft such as the Dassault-Breguet Mirage series, the Eurofighter; North American XB-70, MIG-21, SAAB 35 Draken; and also the Space Shuttle.

Due to the aeroelastic oscillations of the wing, there exists a danger of structural failure in flight at supersonic speeds. It is therefore imperative to find a way to actively control the aeroelastic oscillations in this type of a wing. Hence, the choice of the subject of research.

1.1 Literature Review

Following is the literature review on which the present work is based. The literature review is divided into four parts: the first part briefly discusses the available relevant literature on structural analysis of cantilevered triangular plates alone; the second highlights two methods available for solving for oscillatory flows on delta wings; the third section is more detailed as it introduces work done in the field of active control of structures using smart materials; and lastly some of the literature on active control of aeroelastic oscillations for various wing planforms and panels. is discussed.

Gustafson et al. (1953) carried out an experimental study of natural vibrations of cantilevered triangular plates of uniform thickness. They obtained experimental results for the lowest six frequencies of the delta wing planform of fixed span with increasing aspect ratios. They found that increasing the aspect ratio increased the frequency of each of the six modes of vibration. Andersen (1954) compared his numerical results to those obtained by Gustafson et al. (1953). Andersen (1954) used the *Ritz Approximate* method to approximate the deflection of symmetric (isosceles triangles) and unsymmetric (right-angle triangles) cantilevered plates. He determined the natural frequencies for the lowest two modes of the cantilevered unsymmetric plate.

Pines et al. (1955) developed a numerical approach based on the *Mach Box* method to obtain generalized forces on an oscillating flexible wing in supersonic flow with both supersonic and subsonic edges. Their procedure is limited to Mach numbers of 1.414 and higher. Improving on the work done by Pines et al. (1955), Chipman (1976) analytically refined the *Mach Box* approach, greatly increasing the accuracy of the supersonic oscillatory pressure-distribution. An analytical approach based on the *Frequency Expansion* method has been developed by Carafoli et al. (1969), Mateescu (1969,1970), and Carafoli and Mateescu (1970). This method determines the pressure distribution along the delta wing with subsonic or supersonic leading edges executing oscillations in a uniform flow. However this method based on the *Frequency Expansion* approach can be accurately applied only for the case of very low oscillation frequencies. The hybrid analytical-

numerical method developed in this work for the unsteady aerodynamics of oscillating delta wing eliminates this restriction.

Extensive work — analytical and experimental — has already been done in the field of active control using smart materials. Work on structural vibration control using piezoelectric films or piezoceramic strips bonded to beams, plates and shells is found in the literature. Only some of this available literature on structural vibration control is discussed here.

Early studies carried out by Bailey and Hubbard (1985), Burke and Hubbard (1987), Crawley and de Luis (1987), and Miller and Hubbard (1988) demonstrated the feasibility of providing modal damping using smart materials to beam-like structures. They also discussed the effects of various PVDF strip shapes on the modal control generated.

Studies have been carried out on plate-like structures as well. The active damping control of structural vibration of a one-dimensional plate was analysed and tested by Chiang and Lee (1989). They showed experimentally that the critical first mode can be damped out successfully using smart materials. Lee et al. (1989) incorporated the piezoelectric effects into laminated plates and showed that critical damping of a one-dimensional cantilevered plate can be achieved theoretically using a sensor/actuator combination. Venneri and Wada (1993) studied the effect on the robustness of the structures when adaptive structures are introduced into the structural design. Shen (1994) applied intelligent constrained layers to control bending vibration of composite and isotropic plates. He showed that the vibration amplitude of controllable modes can be reduced significantly for simply-supported isotropic plates. Van Poppel and Misra (1992) successfully developed a state-space feedback control law using piezoelectric film actuators for large structures modelled as cantilevered rectangular plates. They also used the pole-placement technique to calculate the required gains.

Active control using smart materials has been extended to flutter suppression for panels and certain wing planforms as well. Paige et al. (1993) examined an analytical model of a square anisotropic panel accommodating the effects of strain actuators, supersonic aerody-

namics, and gust. They found that a small number of actuators can provide flutter suppression and that increasing the number beyond a certain level produces little improvement. They also demonstrated that actively controlled panels can exhibit superior flutter performance as compared to passively controlled panels. Reich et al. (1994) described the functional requirements and design of an aeroelastic model for wind tunnel investigations of vibration and flutter suppression using piezoelectric actuation. Lin et al. (1995) conducted experiments on both open-loop and closed-loop control of an active flexible wing. The wing planform chosen by them resembled that of a military transport aircraft. Suleman and Venkayya (1996) studied a finite element formulation of flutter control of laminated composite panels with piezoelectric sensors and actuators. Nam et al. (1996) showed that piezoelectric actuators can passively control the flutter of a composite swept wing model by stiffening the model.

1.2 Scope of the Investigation

While considerable research work exists regarding active control of other wing planforms using piezoelectric materials, to the best of the author's knowledge, there is no published literature dealing with suppression of delta wing oscillations using piezoelectric materials. An active control model for a delta wing is needed to extend this promising new approach for aeroelastic flutter suppression to a wing planform that is commonly-used for supersonic aircraft. The development of an active control model necessitates a convenient, efficient, and accurate aerodynamic model that can be easily combined with the structural-piezoelectric model of the delta wing. The aerodynamic and structural-piezoelectric models are developed in this investigation.

Specifically, the objective of this thesis is to study the aeroelastic oscillations of a delta wing in the presence of bonded piezoelectric strips. The dynamic response of the delta wing in the presence of these strips is found using a combination of analytical and numerical techniques. To find the dynamic response of the delta wing, the research was carried out in three major steps:

- modelling of the uncontrolled, unloaded structure;
- modelling of the uncontrolled but aerodynamically loaded structure; and
- modelling of the structure in the presence of aerodynamic and piezoelectric loading.

The present thesis consists of a full exposition of the three modelling steps, plus a presentation of the results. The following paragraphs summarize the five remaining chapters:

Chapter 2 starts with the system description of the delta wing and lists assumptions made in the structural analysis. In this chapter, the wing is modelled as an unloaded, undamped, and uncontrolled cantilevered triangular plate and the formulations expressing the dynamics of this plate are written using an energy approach. These formulations appear in the form of mass and stiffness matrices. The natural frequencies of the free system are obtained and the state-space equation for the system is introduced.

In Chapter 3 a hybrid analytical-numerical aerodynamic model to determine the unsteady pressure distribution over the delta wing is developed. It is shown that the method adopted here to obtain the pressure distribution is more accurate than the *Frequency Expansion* method. As well, a solution under steady flow is obtained and validated against published results to gain confidence in the methodology adopted. The coupling between the structural model of the wing and the unsteady supersonic aerodynamic loading is carried out to obtain generalized forces due to this aerodynamic loading.

Chapter 4 introduces the piezoelectric control action into the structural model. Analytical expressions for interaction between the delta wing modelled as a triangular cantilevered plate and the piezoelectric material are obtained. A finite number of these strain actuators are bonded to the wing as trapezoidal strips. The generalized forces due to the interaction of the piezoelectric strips with the delta wing are determined in this chapter. At the end of the chapter, a concise state-space expression is obtained for the controlled dynamics of the unloaded delta wing using the PVDF actuators.

Chapter 5 consists of two main parts. The first part is an analysis of the dynamic system.

In this section, the methodology to obtain the transient response of the delta wing in the presence of the PVDF actuators alone is discussed. The aerodynamic loading is introduced on the structural-piezoelectric model to study the dynamic response of the wing under their combined forces. The second section presents and discusses the results.

In the final chapter, a summary of results and conclusions is given. Also, a brief discussion on the limitations of this study and recommendations for future work are presented.

Chapter 2

Structural Modelling of the Uncontrolled Wing

This chapter describes the numerical structural modelling of the delta wing without aerodynamic loading or piezoelectric damping. The chapter starts with a description of the physical model of the wing. The undamped, uncontrolled structural model of the delta wing is developed using the energy approach, starting from first principles, in the second section of this chapter. In the third section, the eigenvalue problem of this free system is solved. The final section contains an introduction to the external forces acting on the wing that are considered in this thesis.

2.1 System Description

The delta wing is assumed to be a plate because its length and width are much greater than its thickness. Hence, the problem is a two-dimensional one and the delta wing is modelled as a triangular plate in this thesis. Furthermore, it is assumed that the fuselage is rigid and the wing is rigidly clamped to the fuselage. The width of the fuselage is assumed to be small compared to the length of the plate and therefore the effects of the fuselage on the flow can be neglected. The wing is symmetrical on either side of the fuselage.

The (x, y) coordinate system is defined as shown in Figure 1. The undeformed plate has the x-axis along the trailing edge of the wing and the y-axis is along the width of the wing. The semi-span of the wing, l, is along the x-axis and the chord, c, is measured along the y-axis. The z-axis is taken to be positive downward.

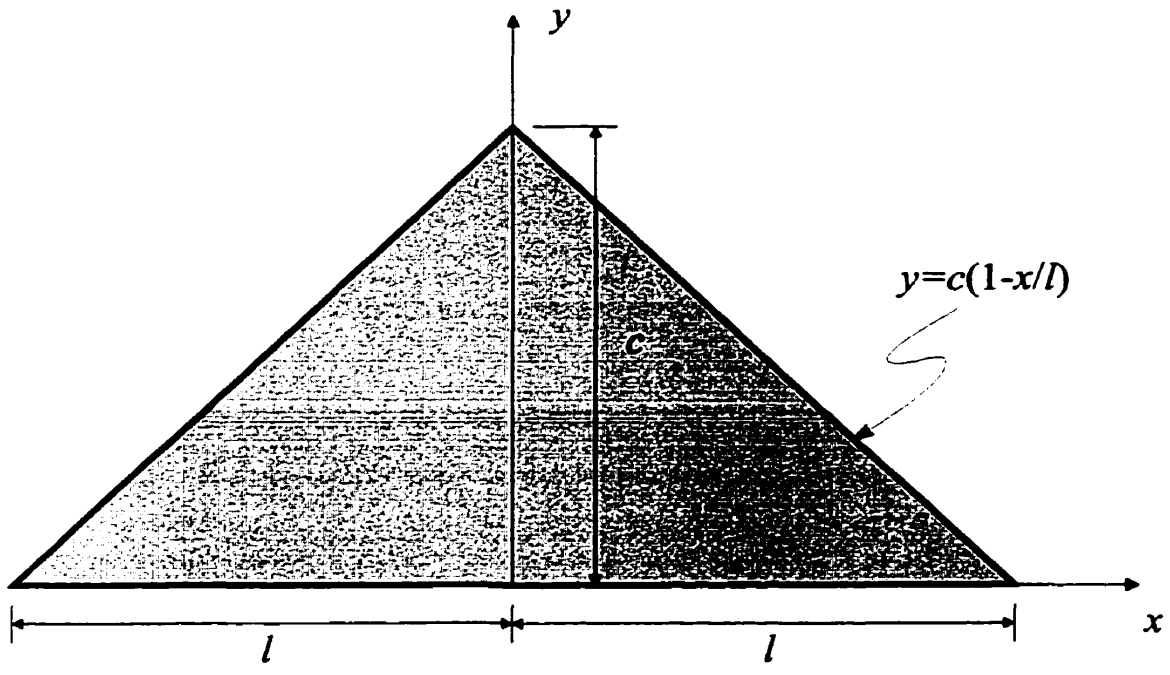

Figure 2.1: Delta Wing Modelled as a Triangular Plate

2.2 The Structural Model

The structural model of the delta wing is developed in this section. Due to symmetry, only one side of the delta wing is modelled for structural analysis. Hence a cantilevered triangular plate is modelled in this chapter and the following assumptions are made:

1. The plate is thin and of uniform thickness, h.

2. For a thin plate, the following well-known approximations called the *Kirchoff's approximations* (Meirovitch, 1967) are made:

   - Normals to the undeformed middle plane remain straight, normal, and inextensible during the deformation, so that transverse normal and shearing strains may be neglected in deriving the plate kinematic relations.

   - Transverse normal stresses are small compared with the other normal stress

components, so that they may be neglected in the stress-strain relations.

- Only small transverse displacements w (in the z-direction) exist. This deflection, w, of the plate is small compared with the plate thickness h.

3. The plate is composed of a homogenous, isotropic material.

The case of an unloaded, uncontrolled, undamped cantilevered triangular plate is considered first. This case will be referred to as a 'free-system' in this thesis. To derive the mass and stiffness matrices of the system using the energy approach, we start with the general expressions for the kinetic and potential energies obtained using Assumption 2 (also called the *thin-plate theory*) which are respectively given by Meirovitch (1967) as:

$$T = \frac{1}{2}\int_A m\left(\frac{\partial w}{\partial t}\right)^2 dA \tag{2.1}$$

$$V = \frac{D}{2}\int_A \left[\left(\frac{\partial^2 w}{\partial x^2} + \frac{\partial^2 w}{\partial y^2}\right)^2 - 2(1-\nu)\left\{\left(\frac{\partial^2 w}{\partial x^2}\frac{\partial^2 w}{\partial y^2}\right) - \left(\frac{\partial^2 w}{\partial x \partial y}\right)^2\right\}\right] dA \tag{2.2}$$

where w is the transverse displacement of an arbitrary point of the cantilevered plate; m is the mass per unit area; and ν is Poisson's ratio. The flexular rigidity of the plate, D, is given by

$$D = \frac{E_p h_p^3}{12(1-\nu^2)} \tag{2.3}$$

where E_p is the Young's modulus of the plate material and h_p is the thickness of the plate.

The two energy expressions can be used to obtain a boundary value problem that describes the free vibration of the plate.

2.2.1 Discretization of the Wing

A closed-form solution of the free (or forced) vibration problem *may not* exist owing to the non-uniform mass and stiffness distribution of a triangular plate. Therefore an approximate solution of the eigenvalue problem of the plate is obtained here. The approximate method used is a scheme for replacing the continuous system by an equivalent discrete one. We will use the *Assumed Modes Method* to generate the mass and stiffness matrices of the discretized system.

As stated by Meirovitch (1967), the *Assumed Modes Method* assumes a solution of boundary-value problems in the form of the following equation:

$$w(x, y, t) = \sum_{r=1}^{M} \sum_{s=1}^{N} \Phi_r(x)\Psi_s(y)q_{rs}(t) \tag{2.4}$$

where w is the transverse displacement expanded in terms of a set of shape functions; q_{rs} is the generalized displacement; Φ_r and Ψ_s are shape functions in clamped-free and free-free directions, respectively; and M and N are the number of clamped-free and free-free shape functions, respectively. Since this is an energy-based formulation, the shape functions need to satisfy only the geometric boundary conditions and not necessarily all the dynamic boundary conditions. In other words, the chosen shape functions are admissible functions. The *Assumed Modes Method* uses equation (2.4) in conjunction with Lagrange's equations of motion to obtain a formulation leading to an approximate solution of the associated eigenvalue problem. Equation (2.4) can be substituted in the kinetic and potential energy equations to generate approximate mass and stiffness matrices. As a first step, the mass and stiffness matrices for the free-system will be determined.

In non-dimensional form, equation (2.4) can be written as,

$$w(\xi, \eta, t) = \sum_{r=1}^{M} \sum_{s=1}^{N} \Phi_r(\xi)\Psi_s(\eta)q_{rs}(t) \tag{2.5}$$

where the non-dimensional coordinates, ξ and η, in x- and y-directions respectively are defined as

$$\xi = \frac{x}{l}$$
$$\eta = \frac{y}{c\left(1 - \frac{x}{l}\right)} \tag{2.6}$$

where l and c have been defined previously.

The clamped-free shape functions for the plate are chosen in the form

$$\Phi_r(\xi) = \xi^{r+1} \tag{2.7}$$

The free-free shape functions for the plate are of the form

$$\Psi_s(\eta) = [(1-\xi)^2(-\eta + 1/2)]^{s-1} \tag{2.8}$$

When $s = 1$, the shape function is the translational rigid body mode and is equal to,

$$\Psi_1(\eta) = 1.0 \tag{2.9}$$

The rotational free-free rigid body mode corresponds to $s = 2$ and reads,

$$\Psi_2(\eta) = (1-\xi)^2(-\eta + 1/2) \tag{2.10}$$

Our goal is to write the kinetic and potential energies in matrix form respectively as

$$T = \frac{1}{2}\{\dot{q}\}^T[M]\{\dot{q}\} \tag{2.11}$$

and,

$$V = \frac{1}{2}\{q\}^T[K]\{q\} \tag{2.12}$$

where $\{\dot{q}\}$ are the generalized velocities, $[M]$ is the mass matrix, and $[K]$ is the stiffness matrix.

We now substitute equations (2.5)-(2.8) in the kinetic and potential energy expressions (equations (2.1) and (2.2)). The kinetic energy expression becomes,

$$T = \frac{1}{2}\rho h_p c l \sum_{r=1}^{M}\sum_{s=1}^{N}\sum_{k=1}^{K}\sum_{p=1}^{P} \dot{q}_{rs}\dot{q}_{kp} \int_0^1\int_0^1 (1-\xi)\Phi_r(\xi)\Psi_s(\eta)\Phi_k(\xi)\Psi_p(\eta)d\xi d\eta \tag{2.13}$$

where ρ is the plate material density.

Only a finite number of modes are modelled and, thus, the summations in equation (2.13) are carried out for only a finite number of terms. The $[M]$ and $[K]$ matrices will now be square matrices of size $(M \times N)$ by $(M \times N)$.

The generalized velocity vector is written as

$$\{\dot{q}_{rs}\} = \left\{ \dot{q}_{11}\ \dot{q}_{12} \cdots \dot{q}_{1N} \cdots \dot{q}_{21}\ \dot{q}_{22} \cdots \dot{q}_{2N} \cdots \dot{q}_{M1}\ \dot{q}_{M2} \cdots \dot{q}_{MN} \right\}^T \tag{2.14}$$

Let $i = 1,2,\ldots..,\ MN$, where $MN = M \times N$; then the generalized velocity vector can also be written as

$$\{\dot{q}_i\} = \left\{ \dot{q}_1\ \dot{q}_2 \cdots \cdots \dot{q}_{MN} \right\}^T \tag{2.15}$$

Equations (2.14) and (2.15) are related via the following change of indices:

$$i = (r-1) \times N + s \tag{2.16}$$

This relationship is also used by van Poppel and Misra (1992). Similarly, the change of indices for the generalized velocity $\dot{q}_{kp}$ in equation (2.13) is given by

$$\dot{q}_{kp} \dashrightarrow \dot{q}_j$$

where

$$j = (k-1) \times N + p \tag{2.17}$$

Therefore, any '*rs*' pair in equation (2.13) corresponds to '*i*' and any '*kp*' pair corresponds to '*j*'. This transforms a 4-dimensional system into a 2-dimensional system, so that equation (2.13) is rewritten as,

$$T = \frac{1}{2}\rho h_p c l \sum_{i=1}^{MN}\sum_{j=1}^{MN} \dot{q}_i \dot{q}_j \int_0^1\int_0^1 (1-\xi)\Phi_r(\xi)\Psi_s(\eta)\Phi_k(\xi)\Psi_p(\eta)d\xi d\eta \tag{2.18}$$

or,

$$T = \frac{1}{2}\sum_{i=1}^{MN}\sum_{j=1}^{MN} m_{ij}\dot{q}_i\dot{q}_j \tag{2.19}$$

where m_{ij} are the elements of the mass matrix and are defined as

$$m_{ij} = \rho h_p c l \int_0^1\int_0^1 (1-\xi)\Phi_r(\xi)\Psi_s(\eta)\Phi_k(\xi)\Psi_p(\eta)d\xi d\eta \tag{2.20}$$

Thus, the mass matrix of a cantilevered triangular plate is determined by expanding the displacement function in terms of the generalized displacements, $\{q_{rs}\}$, and then by setting equations (2.1) and (2.11) equal.

The stiffness matrix is determined by a similar procedure: the displacement function, w, is expanded in terms of generalized displacements, substituted into the potential energy expressions and then (2.2) and (2.12) are equated. We get an expression for the potential energy, V, which can be written as,

$$V = \frac{D}{2}\int_0^1\int_0^1 \Bigg((1-\xi)\left(\frac{\partial^2 w}{\partial \xi^2}\right)^2 + 4\eta \frac{\partial^2 w}{\partial \xi^2}\frac{\partial^2 w}{\partial \xi \partial \eta}$$
$$+ \frac{2}{(1-\xi)}\left\{ [2\eta^2 + k^2(1-\nu)]\left(\frac{\partial^2 w}{\partial \xi \partial \eta}\right)^2 + (\eta^2 + \nu k^2)\frac{\partial^2 w}{\partial \xi^2}\frac{\partial^2 w}{\partial \eta^2} + 2\eta \frac{\partial^2 w}{\partial \xi^2}\frac{\partial w}{\partial \eta} \right\}$$
$$+ \frac{4}{(1-\xi)^2}\left\{ [2\eta^2 + k^2(1-\nu)]\frac{\partial w}{\partial \eta}\frac{\partial^2 w}{\partial \xi \partial \eta} + (\eta^3 + k^2\eta)\frac{\partial^2 w}{\partial \eta^2}\frac{\partial^2 w}{\partial \xi \partial \eta} \right\}$$
$$+ \frac{1}{(1-\xi)^3}\left\{ 2[2\eta^2 + k^2(1-\nu)]\left(\frac{\partial w}{\partial \eta}\right)^2 + 4(\eta^3 + (1-\nu)k^2\eta)\frac{\partial w}{\partial \eta}\frac{\partial^2 w}{\partial \eta^2} \right.$$
$$\left. + (\eta^4 + k^4 + 2(1-\nu)k^2\eta^2)\left(\frac{\partial^2 w}{\partial \eta^2}\right)^2 \right\} \Bigg) \frac{c}{l^3} d\xi d\eta \qquad (2.21)$$

or,

$$V = \frac{1}{2}\sum_{i=1}^{MN}\sum_{j=1}^{MN} k_{ij} q_i q_j \qquad (2.22)$$

where k_{ij} are the elements of the stiffness matrix which are given in Appendix A.

Hence, both the mass matrix, $[M]$, and the stiffness matrix, $[K]$, for the cantilevered triangular plate have been obtained.

2.3 Natural Frequencies of the Wing

In this section, the eigenvalue problem of the free vibrating plate is solved. In other words, the plate is assumed to have no external forces present. Solving the eigenvalue problem is synonymous with obtaining its natural frequencies.

We start with Lagrange's equations for a conservative system to evaluate the plate frequencies. These equations are

$$\frac{d}{dt}\left(\frac{\partial L}{\partial \dot{q}_i}\right) - \frac{\partial L}{\partial q_i} = 0 , \qquad i = 1, 2, ..., MN \tag{2.23}$$

where the Lagrangian, L, is defined by

$$L = T - V \tag{2.24}$$

and q_i are the generalized displacements. Inserting equations (2.19) and (2.22) into this equation and simplifying we get the equation of motion of a free vibrating system which is of the form

$$[M]\{\ddot{q}\} + [K]\{q\} = 0 \tag{2.25}$$

This yields an eigenvalue problem which can be written as

$$\lambda[M]\{q\} = [K]\{q\} \tag{2.26}$$

where

$$\lambda = \omega_n^2 \tag{2.27}$$

and where ω_n is the natural frequency of the delta wing.

A simple program can be written in MATLAB to determine the natural frequencies of the

free-system as described by equation (2.26) using the mass and stiffness matrices. The eigenvalues for various modes of vibration of the free-system are obtained and validated against published results in Chapter 5.

For later reference, equation (2.25) can be written in its state-space form, namely,

$$\{\dot{x}\} = [A]\{x\} \tag{2.28}$$

where the state vector is constructed from the generalized displacements and their first derivatives as

$$\{x\} = \begin{Bmatrix} \{q\} \\ \{\dot{q}\} \end{Bmatrix} \tag{2.29}$$

Also, the matrix $[A]$ is of size $2MN$ x $2MN$ and is written as

$$[A] = \begin{bmatrix} [0] & [I] \\ -[M]^{-1}[K] & [0] \end{bmatrix} \tag{2.30}$$

where $[I]$ is the identity matrix of size MN x MN.

The structural model for the delta wing has now been formulated using the energy approach. The next section introduces the external forces that are considered to act on the wing.

2.4 Generalized Forces

When the system is subjected to external forces that do not have an associated potential energy it is called a non-conservative system. The Lagrange's equations for this non-conservative system are

$$\frac{d}{dt}\left(\frac{\partial L}{\partial \dot{q}_i}\right) - \frac{\partial L}{\partial q_i} + \frac{\partial \mathcal{F}}{\partial \dot{q}_i} = Q_i , \qquad i = 1, 2, ..., MN \tag{2.31}$$

where L is again the Lagrangian and is defined by equation (2.24), Q_i are called generalized forces associated with the generalized displacements q_i, and $\mathcal{F}$ is the *Rayleigh's dissipation function*. This function takes into account the energy dissipation in the structure with the assumption that it can be modelled through viscous damping.

The general expression for the dynamics of a plate can now be obtained from equation (2.31) in the following matrix form:

$$[M]\{\ddot{q}(t)\} + [C]\{\dot{q}(t)\} + [K]\{q(t)\} = \{Q\} \tag{2.32}$$

where $[M]$, [C] and $[K]$ are the mass, structural damping and stiffness matrices, respectively, and $\{Q\}$ is the generalized force action vector. It should be noted that this equation is similar to equation (2.25). All the matrices of the above equation, which are generated analytically and eventually evaluated numerically, must represent as closely as possible the actual dynamics of the cantilevered triangular plate and hence the delta wing. The mass and stiffness matrices were generated in section 2.2.

The structural damping is written as

$$[C] = \alpha[M] + \beta[K] \tag{2.33}$$

where α and β are plate material constants. This model corresponds to *Rayleigh damping*. Matrix $[A]$ from equation (2.30) now becomes

$$[A] = \begin{bmatrix} [0] & [I] \\ -[M]^{-1}[K] & -[M]^{-1}[C] \end{bmatrix} \tag{2.34}$$

The external forcing action vector consists of two components: the unsteady, supersonic aerodynamic loading and the controlling action of the piezoelectric strips. This combination is represented mathematically as

$$\{Q\} = \{Q_{aero}\} + \{Q_{piezo}\} \tag{2.35}$$

where $\{Q_{aero}\}$ and $\{Q_{piezo}\}$ are the generalized forces due to the supersonic, unsteady aerodynamic loading and the controlling action of the PVDF strips, respectively.

Substituting equation (2.35) in equation (2.32), the final equation for the dynamic system becomes

$$[M]\{\ddot{q}\} + [C]\{\dot{q}\} + [K]\{q\} = \{Q_{aero}\} + \{Q_{piezo}\} \tag{2.36}$$

Thus, the mathematical model for the delta wing in supersonic flow under the influence of piezoelectric material is given by equation (2.36). The expressions for $\{Q_{aero}\}$ and $\{Q_{piezo}\}$ are derived in Chapters 3 and 4 respectively.

The unsteady, supersonic aerodynamic loading will be introduced on the delta wing and $\{Q_{aero}\}$ will be obtained in the next chapter.

Chapter 3

Aerodynamic Modelling

In the first section of this chapter, the *Basic Linearized Theory* for supersonic potential flow is presented as the basis for determining the pressure distribution on the delta wing in unsteady supersonic flow. In the second section, steady flow over the wing is introduced to gain confidence in the developed methodology. In the third section, the pressure distributions calculated using the method developed in this research and using an existing method are compared. In the final section, the generalized forces due to this unsteady supersonic aerodynamic loading are derived.

3.1 Basis for Aerodynamic Modelling

As discussed in Chapter 2, the delta wing is assumed to be a triangular plate and the wing is symmetric with respect to the centreline. To simplify the aerodynamic analysis, the (x_1, x_2) coordinate system shown in Figure 3.1 is used. The following simple conversion from the (x, y) coordinate system described in Chapter 2 to the (x_1, x_2) coordinate system is made:

$$\begin{aligned} x_1 &= y - c \\ x_2 &= x \end{aligned} \tag{3.1}$$

where c is the central chord of the wing. The following conical coordinates y and z will also be used for convenience:

$$y = \frac{x_2}{x_1}, \qquad z = \frac{x_3}{x_1} \tag{3.2}$$

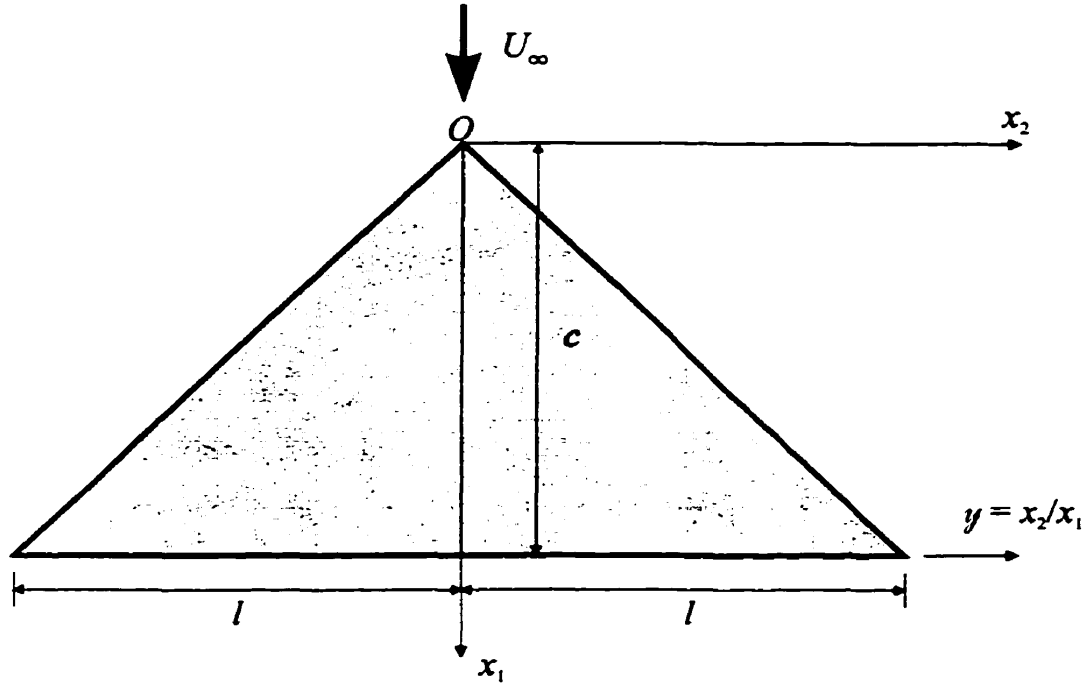

Figure 3.1: System Description for Aerodynamic Modelling

where the coordinate x_3 is normal to the plane Ox_1x_2.

As seen in Figure 3.1, the semi-span of the wing, l, is along the y-axis and the chord, c, is along the x_1-axis. Also, the air flow velocity is denoted by U_∞. The subscript ∞ is used to denote the undisturbed free airstream.

3.1.1 Basic Linearized Theory

The airstream in which the wing is situated is initially assumed to be uniform and characterized by the airspeed U_∞ with small time-dependent pertubations generated by the wing oscillations around its mean position. Effects of viscosity and heat conduction are neglected. The air however is assumed to be compressible. Any shock waves formed by the motion are assumed to be weak so that the flow may be considered as irrotational and isentropic.

With the assumptions stated above, the unsteady motion of the wing is defined by the following general expression of the basic unsteady linearized equation for a 3-D case

$$(1-M_\infty^2)\frac{\partial^2\varphi}{\partial x_1^2}+\frac{\partial^2\varphi}{\partial x_2^2}+\frac{\partial^2\varphi}{\partial x_3^2}=\frac{M_\infty^2}{U_\infty^2}\frac{\partial^2\varphi}{\partial t^2}+2\frac{M_\infty^2}{U_\infty}\frac{\partial^2\varphi}{\partial x_1\partial t} \tag{3.3}$$

where φ is the pertubation velocity potential and is a function of space and time; t is time; and M_∞ is the free airstream Mach number which is defined as

$$M_\infty=\frac{U_\infty}{a_\infty}$$

The derivation of equation (3.3) is given in Carafoli et al. (1969) and Doe (1985). Equation (3.3) becomes

$$(1-M_\infty^2)\frac{\partial^2\varphi}{\partial x_1^2}+\frac{\partial^2\varphi}{\partial x_2^2}+\frac{\partial^2\varphi}{\partial x_3^2}=0 \tag{3.4}$$

when the flow is steady and then φ is a function of space alone.

With the present approximations, the expression for the coefficient of pressure, C_p, is given in Carafoli et al. (1969) as

$$C_p=\frac{p-p_\infty}{\frac{1}{2}\rho_\infty U_\infty^2}=-\frac{2}{U_\infty^2}\left(\frac{\partial\varphi}{\partial t}+\frac{U_\infty^2}{c}\frac{\partial\varphi}{\partial x_1}\right) \tag{3.5}$$

where p is pressure and ρ_∞ is free airstream density. This expression is used in the present study as well.

3.1.2 Problem Formulation and Solutions

The delta wing with supersonic leading edges is assumed to execute harmonic oscillations of low frequency defined by the equation of the unsteady wing surface

$$x_3 = x_1 P(x_1, x_2) e^{i\omega t} \tag{3.6}$$

where ω is the frequency of periodic motion and $P(x_1, x_2)$ is a function of the space coordinates, which can be represented as a sum of homogenous polynomials $P_n(x_1, x_2)$ of various orders in x_1 and x_2.

As a result, the velocity potential $\varphi(x_1, x_2, x_3, t)$ of this unsteady flow is also a periodic function with the same frequency ω, which has to satisfy the potential equation (3.3). By using the reduced potential $\hat{\varphi}$ defined by the potential transformation as given in Carafoli et al. (1969), we can write

$$\varphi(x_1, x_2, x_3, t) = U_\infty c e^{i(\omega t + k x_1)} \hat{\varphi}(x_1, x_2, x_3) \tag{3.7}$$

where c is the wing chord, k is given as

$$k = -\frac{\omega c}{U_\infty} \frac{M_\infty^2}{B^2} \quad , \tag{3.8}$$

and where B is defined as

$$B = \sqrt{M_\infty^2 - 1} \tag{3.9}$$

The unsteady potential equation (3.3) is reduced to the following differential equation independent of time,

$$-B^2\hat{\varphi}_{x_1x_1} + \hat{\varphi}_{x_2x_2} + \hat{\varphi}_{x_3x_3} - \lambda^2\frac{M_\infty^2}{B^2}\hat{\varphi} = 0 \tag{3.10}$$

where $\hat{\varphi}_{x_1x_1}$, $\hat{\varphi}_{x_2x_2}$ and $\hat{\varphi}_{x_3x_3}$ are second-order derivatives of the reduced potential, $\hat{\varphi}$, with respect to x_1, x_2 and x_3, respectively, and where

$$\lambda = \frac{\omega c}{U_\infty} \tag{3.11}$$

The coefficient of pressure for an oscillatory flow over the delta wing is now written in terms of the reduced potential as

$$C_p(x_1, x_2, x_3, t) = \hat{C}_p(x_1, x_2, x_3)e^{i\omega t} \tag{3.12}$$

where

$$\hat{C}_p(x_1, x_2, x_3) = -2e^{ikx_1}\left[i(k+\lambda)\hat{\varphi} + \frac{\partial\hat{\varphi}}{\partial x_1}\right] \tag{3.13}$$

$\hat{C}_p$ is referred to as the reduced coefficient of pressure over the wing. When φ is differentiated with respect to x_1, we get

$$u = \frac{1}{c}\frac{\partial\varphi}{\partial x_1} = U_\infty e^{ikx_1}\left[ik\hat{\varphi}(x_1, x_2, x_3) + \frac{\partial\hat{\varphi}(x_1, x_2, x_3)}{\partial x_1}\right]e^{i\omega t} \tag{3.14}$$

and when φ is differentiated with respect to time, we get

$$\frac{\partial\varphi}{\partial t} = U_\infty^2 i\lambda e^{ikx_1}\hat{\varphi}(x_1, x_2, x_3)e^{i\omega t} \tag{3.15}$$

The boundary conditions on the oscillatory wing can be expressed taking into account equation (3.6), as

$$\bar{w} = \frac{\partial\varphi}{\partial x_3} = U_\infty e^{i\omega t}\left(\frac{\partial P}{\partial x_1} + \frac{i\omega}{U_\infty}P\right) \tag{3.16}$$

where $\bar{w}$ represents the vertical pertubation velocity, or upwash. The bar over w is to distinguish this notation of the upwash from that of the wing displacement, w, as used in Chapter 2. A reduced upwash (as given in Carafoli et al., 1969) is now introduced. This upwash is defined on the plane wing, that is $x_3 = 0$, as

$$\hat{w}(x_1, x_2) = \frac{\partial \hat{\Phi}}{\partial x_3} = e^{-ikx_1} \hat{W}(x_1, x_2) \tag{3.17}$$

where $\hat{W}(x_1, x_2)$ is the reduced vertical velocity on the wing, defined by

$$\hat{W}(x_1, x_2) = \frac{\partial P}{\partial x_1} + i\lambda P \tag{3.18}$$

In Carafoli et al. (1969), it is assumed that k is small and $e^{\pm ikx_1}$ in equation (3.17) is approximately written as

$$e^{\pm ikx_1} \approx 1 \pm ikx_1$$

In other words, in the expansion of $e^{\pm ikx_1}$, k^2 and higher order terms are neglected. But in the present work the higher order terms in the expansion of $e^{\pm ikx_1}$ are *not* neglected. Hence more accurate results can be expected.

Consider the case of the wing executing harmonic oscillations in translation and rotation defined as

$$\begin{aligned} h(t) &= c\hat{h}e^{i\omega t}, \\ \theta(t) &= \hat{\theta}e^{i\omega t}, \\ \psi(t) &= \hat{\psi}e^{i\omega t} \end{aligned} \tag{3.19}$$

where $h(t)$ denotes small vertical translational oscillations, $\theta(t)$ denotes small pitching rotation about the x_2-axis, and $\psi(t)$ denotes small rolling rotation about the x_1-axis. In this case the equation of the wing surface can be expressed as

$$x_3 = h - x_1\theta + x_2\psi = e^{i\omega t}(c\hat{h} - x_1\hat{\theta} + x_2\hat{\psi}) \tag{3.20}$$

and therefore,

$$P(x_1, x_2) = c\hat{h} - x_1\hat{\theta} + x_2\hat{\psi} \tag{3.21}$$

Substituting equation (3.21) into (3.18), the reduced vertical velocity on the wing becomes

$$\hat{W}(x_1, x_2) = [-\hat{\theta} + i\lambda(c\hat{h} - \hat{\theta}x_1 + \hat{\psi}x_2)] \tag{3.22}$$

where λ is defined in equation (3.11).

The next step is to determine the supersonic pulsating source for the system as shown by Mateescu (1989). For this let (x_1, x_2) be the receiving point and (x_{1s}, x_{2s}) be the sending point as shown in Figure 3.2.

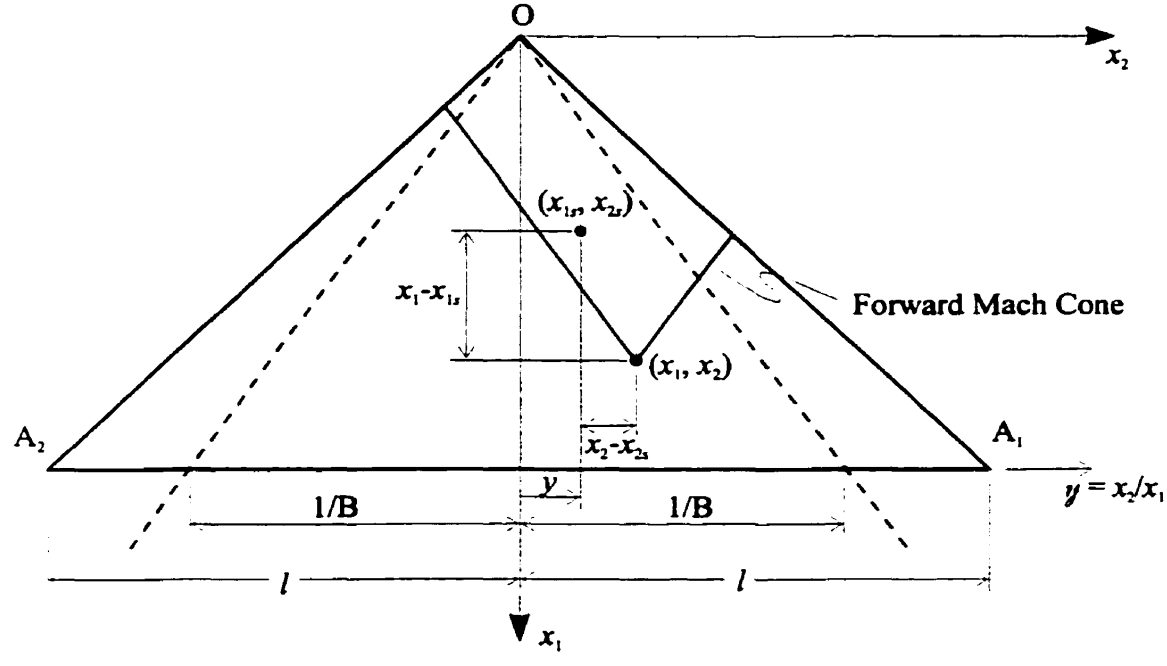

Figure 3.2: Sending and Receiving Points Inside the Mach Cone for a Plane Flow.

The potential of the reduced pulsating source placed at (x_{1s}, x_{2s}) is of the form

$$\hat{\varphi}(x_1, x_2) = \hat{\varphi}_1(R) \tag{3.23}$$

where

$$R = \sqrt{(x_1 - x_{1s})^2 - B^2(x_2 - x_{2s})^2} \tag{3.24}$$

Substituting equation (3.24) into equation (3.23) and in turn substituting the result into equation (3.10), we get

$$\frac{\partial^2 \hat{\varphi}_1}{\partial R^2} + \frac{2}{R}\frac{\partial \hat{\varphi}_1}{\partial R} + \frac{K^2}{B^2}\hat{\varphi}_1(R) = 0$$

where

$$K = \lambda \frac{M_\infty}{B} \tag{3.25}$$

A solution to this equation is

$$\hat{\varphi}_1(R) = \frac{1}{R}\cos\left(\frac{K}{B}R\right)$$

Therefore, the supersonic pulsating source potential for the delta wing is

$$\varphi(x_1, x_2, t) = \frac{1}{R}\cos\left(\frac{K}{B}R\right) e^{i\left(K\frac{M_\infty}{B}x_1\right)} e^{i\omega t} \tag{3.26}$$

where K is related to k by the following equation

$$k = -K\frac{M_\infty}{B} \tag{3.27}$$

Hence the potential of the source distribution on the plane of the wing, $x_3 = 0$, becomes

$$\hat{\varphi}(x_1, x_2) = -\frac{1}{\pi}\iint \hat{W}(x_{1s}, x_{2s}) e^{-ik(x_1 - x_{1s})} \cos\left(\frac{k}{M_\infty} R\right) \frac{dx_{1s} dx_{2s}}{R} \tag{3.28}$$

where $\hat{W}(x_{1s}, x_{2s})$ is the vertical velocity at any point on the plane of the wing and is also given by equation (3.22) in the case of oscillatory translation and rotation.

As a reminder, equation (3.13) which is the equation for the reduced coefficient of pressure can also be expressed as

$$\hat{C}_p(x_1, x_2) = -2[\cos(kx_1) + i\sin(kx_1)]\left[i(k+\lambda)\hat{\varphi} + \frac{\partial \hat{\varphi}}{\partial x_1}\right] \tag{3.29}$$

To solve equation (3.28) a new coordinate system (X, Y) is defined where

$$\begin{aligned} X &= x_1 - x_{1s} \\ Y &= \frac{x_2 - x_{2s}}{x_1 - x_{1s}} \end{aligned} \tag{3.30}$$

For a plane wing, $Z = 0$. Substituting the above into equation (3.24) we get

$$R = X\bar{R} \tag{3.31}$$

where

$$\bar{R} = \sqrt{1 - B^2 Y^2} \tag{3.32}$$

for a plane wing. Also using the Jacobian, $dx_{1s} dx_{2s}$ becomes $XdXdY$. Rewriting equations (3.28) in terms of the new coordinate system and simplifying, we get

$$\hat{\varphi}(x_1, x_2) = -\frac{1}{\pi}\iint \hat{W}(x_{1s}, x_{2s}) e^{-ikX} \cos\left(\frac{k}{M_\infty} X\bar{R}\right) \frac{dXdY}{\bar{R}} \tag{3.33}$$

The next step is to determine the limits of integration (please refer to Figure 3.2). The limits of integration in X inside the Mach cone are

- 0 to X_1 where the limits of integration in Y are $-\frac{1}{B} \le Y \le y$
- 0 to X_2 where the limits of integration in Y are $y \le Y \le \frac{1}{B}$

where

$$\begin{aligned} X_1 &= x_1 \frac{(l-y)}{(l-Y)} \\ X_2 &= x_1 \frac{(l+y)}{(l+Y)} \end{aligned} \tag{3.34}$$

Please refer to Appendix B for the derivation of equation (3.34). Integration in X is carried out analytically and the limits over X as defined in equation (3.34) are substituted in the result to give

$$\begin{aligned} \hat{\varphi} = &-\frac{1}{\pi}\int_{-\frac{1}{B}}^{y} \hat{W}(x_{1s}, x_{2s}) \frac{e^{-ikX_1}}{\left(\frac{K}{B}\bar{R}\right)^2 - k^2}\left[-ik\cos\left(\left(\frac{K}{B}\bar{R}X_1\right) + \left(\frac{K}{B}\bar{R}\right)\sin\left(\frac{K}{B}\bar{R}X_1\right)\right)\right]\frac{dY}{\sqrt{1-B^2Y^2}} \\ &-\frac{1}{\pi}\int_{y}^{\frac{1}{B}} \hat{W}(x_{1s}, x_{2s}) \frac{e^{-ikX_2}}{\left(\frac{K}{B}\bar{R}\right)^2 - k^2}\left[-ik\cos\left(\left(\frac{K}{B}\bar{R}X_2\right) + \left(\frac{K}{B}\bar{R}\right)\sin\left(\frac{K}{B}\bar{R}X_2\right)\right)\right]\frac{dY}{\sqrt{1-B^2Y^2}} \end{aligned} \tag{3.35}$$

Differentiating this equation of the reduced potential with respect to x_1, we get

$$\frac{\partial \hat{\varphi}}{\partial x_1} = -\frac{1}{\pi}\int_{-\frac{1}{B}}^{y} \hat{W}(x_{1s}, x_{2s})\frac{l}{(l-Y)}e^{-ikX_1}\cos\left(\frac{K}{B}\bar{R}X_1\right)\frac{dY}{\sqrt{1-B^2Y^2}} \qquad (3.36)$$
$$-\frac{1}{\pi}\int_{y}^{\frac{1}{B}} \hat{W}(x_{1s}, x_{2s})\frac{l}{(l+Y)}e^{-ikX_2}\cos\left(\frac{K}{B}\bar{R}X_2\right)\frac{dY}{\sqrt{1-B^2Y^2}}$$

where $\bar{R}$, X_1 and X_2 are defined by equations (3.32) and (3.34) respectively.

Unfortunately, at $Y = -\frac{1}{B}$ and at $Y = \frac{1}{B}$ a singularity exists and equations (3.35) and (3.36) cannot be solved purely numerically in the present form. To resolve this problem, the integration in Y is solved semi-analytically. The semi-analytical solution involves analytically integrating the two equations by parts, then solving the simplified equation using a 10-point Gaussian quadrature scheme.

The semi-analytical integration over Y of equations (3.35) and (3.36) involves the use of the following general form:

- when $-\frac{1}{B} \le Y \le y$, use the following:

$$\int_{-\frac{1}{B}}^{y} \mathcal{J}(Y)\frac{dY}{\sqrt{1-B^2Y^2}} = \int_{-\frac{1}{B}}^{y} \frac{\mathcal{J}(Y)-\mathcal{J}(-1/B)}{\sqrt{1-B^2Y^2}}dY + \int_{-\frac{1}{B}}^{y} \frac{\mathcal{J}(-1/B)}{\sqrt{1-B^2Y^2}}dY \qquad (3.37a)$$

- when $y \le Y \le \frac{1}{B}$, use the following:

$$\int_{y}^{\frac{1}{B}} \mathcal{J}(Y)\frac{dY}{\sqrt{1-B^2Y^2}} = \int_{y}^{\frac{1}{B}} \frac{\mathcal{J}(Y)-\mathcal{J}(1/B)}{\sqrt{1-B^2Y^2}}dY + \int_{y}^{\frac{1}{B}} \frac{\mathcal{J}(1/B)}{\sqrt{1-B^2Y^2}}dY \qquad (3.37b)$$

From equation (3.29), the final expression for $\hat{C}_p$ inside the Mach cone is written in complex form as:

$$\hat{C}_p = Real\ \hat{C}_p + i\ Imag\ \hat{C}_p \tag{3.38}$$

where

$$\begin{aligned} Real\ \hat{C}_p &= -\frac{2}{\pi}\{[Real\ F]\cos(kx_1) - [Imag\ F]\sin(kx_1)\} \\ Imag\ \hat{C}_p &= -\frac{2}{\pi}\{\ [Imag\ F]\cos(kx_1) + [Real\ F]\sin(kx_1)\} \end{aligned} \tag{3.39}$$

In equation (3.39),

$$F = i(k+\lambda)\hat{\varphi} + \frac{\partial\hat{\varphi}}{\partial x_1} \tag{3.40}$$

The above equation is also written in complex form as defined below:

$$F = Real\ F + i\ Imag\ F \tag{3.41}$$

where

$$\begin{aligned} Real\ F &= Real\ I_1 + Real\ I_2 \\ Imag\ F &= Imag\ I_1 + Imag\ I_2 \end{aligned} \tag{3.42}$$

In equation (3.42), we obtain $Real\ I_1$ and $Imag\ I_1$ from equations (3.35), (3.36), (3.37a), and (3.38) to (3.40) for $-\frac{1}{B} \le Y \le y$; and $Real\ I_2$ and $Imag\ I_2$ from equations (3.35), (3.36), (3.37b) and (3.38) to (3.40) for $y \le Y \le \frac{1}{B}$. Please see sections 3.3.2 and 3.4 for more details.

The analytically simplified expressions of equations (3.35) and (3.36), as given in section 3.3, are solved numerically using a 10-point Gaussian quadrature scheme written in the FORTRAN. The result is then substituted into equation (3.38) to find the reduced coefficient of pressure, $\hat{C}_p$. Hence the reduced pressure distribution on the delta wing for supersonic flow inside the Mach cone is obtained. Results of this method are compared against the method developed in Carafoli et al. (1969) in section 3.3. Equations (3.37a) and (3.37b)

are also used for simplifying the expressions for outside the Mach cone as will be seen later. First, however, to gain confidence in the *Present Method*, we will apply this method to the simpler case of steady flow in the following section.

3.2 Steady Flows

Steady flows are studied in the present research to gain confidence in the methodology adopted for dealing with oscillatory flows over the delta wing. These flows have a linear, simpler solution and the results can be validated using existing solutions (Carafoli et al., 1969).

When velocity and pressure do not vary with time, the flow is said to be steady. There are of course no harmonic oscillations present either ($\omega = 0$). Therefore, in this case equation (3.4) is satisfied. Again the wing is assumed to be at zero incidence and the air assumed to be compressible.

Let us consider the supersonic flow past a delta wing. The coefficient of pressure for this flow over the wing is given as

$$C_p = -2\frac{u}{U_\infty} \tag{3.43}$$

The supersonic source for this steady plane flow is

$$\varphi_1(x_1, x_2) = \frac{1}{R} \tag{3.44}$$

where R is given by equation (3.24).

The source distribution for this flow over the entire delta wing is

$$\varphi(x_1, x_2) = -\frac{1}{\pi}\int\int W(x_{1s}, x_{2s})\ \frac{dx_{1s}dx_{2s}}{R} \tag{3.45}$$

where $W(x_{1s}, x_{2s})$ is again the vertical velocity on the wing. Note that equation (3.45) can be obtained from equation (3.28) by introducing $\omega = 0$ and $k = 0$.

As was done in the unsteady case, a new coordinate system (X, Y) is introduced to solve for φ. The transformation from the (x_{1s}, x_{2s}) coordinate system to (X, Y) coordinate system is again given by equation (3.30). Also, the limits of integration over X and Y are the same as that used in section 3.1.

Now let x_{2s} be written as the following

- when $-\frac{1}{B} \le Y \le y$:

$$x_{2s} = x_2 - XY \tag{3.46}$$

- and when $y \le Y \le \frac{1}{B}$:

$$x_{2s} = -x_2 + XY \tag{3.47}$$

Equations (3.46) and (3.47) are substituted into equation (3.45) to give

$$\varphi = \pm\frac{1}{\pi}\int\int(x_2 - XY)\frac{dXdY}{\bar{R}} \tag{3.48}$$

Equation (3.48) is now integrated analytically over X as was done in the unsteady case. Therefore the velocity potential for a steady flow over the delta wing now becomes

$$\varphi = \pm\frac{x_2}{\pi}I(x_1,x_2) - \left(\frac{x_1^2(l-y)^2}{2\pi}\int_{-\frac{1}{B}}^{y}\frac{Y}{(l-Y)^2}\frac{dY}{\sqrt{1-B^2Y^2}}\right) + \left(\frac{x_1^2(l+y)^2}{2\pi}\int_{y}^{\frac{1}{B}}\frac{Y}{(l+Y)^2}\frac{dY}{\sqrt{1-B^2Y^2}}\right) \tag{3.49}$$

where

$$I(x_1,x_2) = x_1(l-y)\int_{-\frac{1}{B}}^{y}\frac{dY}{(l-Y)\sqrt{1-B^2Y^2}} + x_1(l+y)\int_{y}^{\frac{1}{B}}\frac{dY}{(l+Y)\sqrt{1-B^2Y^2}} \tag{3.50}$$

Again, as seen in the unsteady case, there exists a singularity at $Y = -\frac{1}{B}$ and at $Y = \frac{1}{B}$. Therefore, equation (3.48) is differentiated with respect to x_1 using *Lebnitz's Rule* and solved semi-analytically by parts using equation (3.37a) and (3.37b) as was done in the unsteady case. Thus the velocity is given as

$$u = u_1^* - \frac{x_1 l}{\pi}(u_2^* + u_3^*) \tag{3.51}$$

where u_1^*, u_2^*, and u_3^* are the components of the velocity given as

$$u_1^* = \frac{2x_1 yl}{\pi\sqrt{B^2l^2-1}}\left[\cos^{-1}\sqrt{\frac{(1-By)(1+Bl)}{2B(l-y)}} - \cos^{-1}\sqrt{\frac{(1+By)(1+Bl)}{2B(l+y)}}\right]$$

$$u_2^* = (l-y)\left\{\int_{-\frac{1}{B}}^{y}\left[\frac{Y}{(l-Y)^2} + \frac{B}{(Bl+1)^2}\right]\frac{dY}{\sqrt{1-B^2Y^2}} - \frac{B}{(Bl+1)^2}\left(\sin^{-1}(By) + \frac{\pi}{2}\right)\right\}$$

$$u_3^* = -(l+y)\left\{\int_{y}^{\frac{1}{B}}\left(\left[\frac{Y}{(l+Y)^2} - \frac{B}{(Bl+1)^2}\right]\frac{dY}{\sqrt{1-B^2Y^2}} + \frac{B}{(Bl+1)^2}\left(\frac{\pi}{2} - \sin^{-1}(By)\right)\right)\right\} \tag{3.52}$$

As was done in the previous section, the final integration in Y is solved numerically using a 10-point Gaussian quadrature scheme. The result is then substituted into equation (3.43) to obtain the coefficient of pressure distribution along the wing under steady flow.

In the next section, the values of C_p obtained from this section are compared to the values of C_p obtained under similar flow conditions by Carafoli et al. (1969). The data is given in tabular form in Appendix B.

3.3 Method Validation

The results obtained for the pressure distribution over the delta wing for steady and unsteady supersonic flow, as derived in the previous sections are compared with the results of Carafoli et al. (1969) inside the Mach cone under the following conditions:

- $l = 2$ m and $c = 1$ m;
- $x_1 = c$ and $-\frac{1}{B} \le x_2 \le \frac{1}{B}$; and
- $M_\infty = \sqrt{2.0}$, therefore, $B = 1.0$.

3.3.1 Results of Steady Supersonic Flow

Consider steady flow over the delta wing. Let the vertical velocity be

$$W(x_{1s}, x_{2s}) = -\alpha U_\infty$$

Substituting this vertical velocity in equation (3.45) and rewriting the result in the (X, Y) coordinate system we can solve for the coefficient of pressure distribution along the wing as discussed above. The results are shown in Table 1 of Appendix B and the graphical com-

parison is given in Figure 3.3. The results shown are for various points along the wing, that is, for various values of $y = \frac{x_2}{x_1}$, along the delta wing keeping $x_1 = c$.

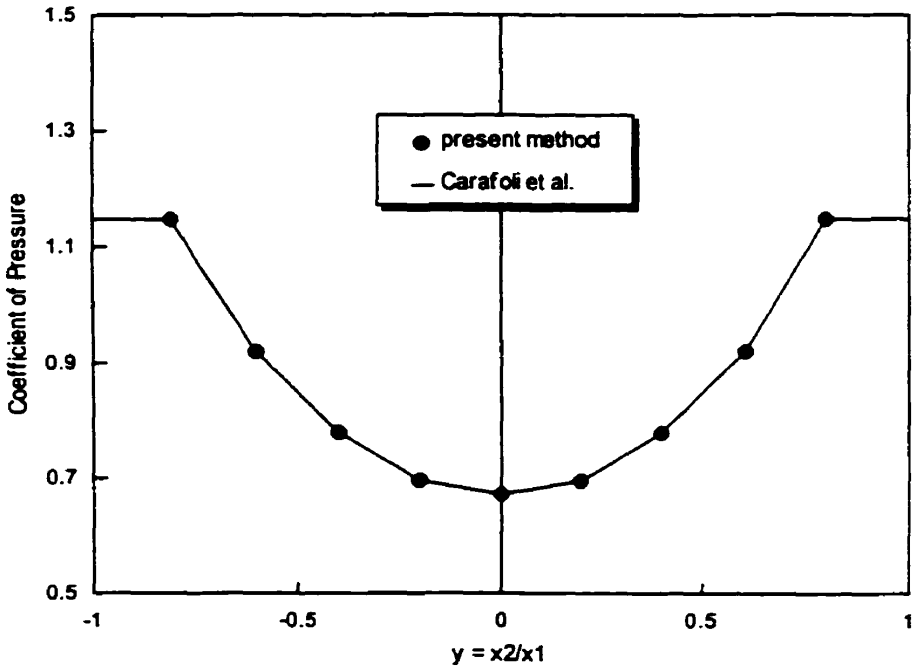

Figure 3.3: Comparison of C_p: Steady Flow

As seen from Figure 3.3 the two methods give identical results. As expected, the pressure distribution is symmetrical on either side of the central chord because of the symmetry of the wing. The coefficient of pressure is lowest at the fuselage, that is, when $y = 0$ and increases towards the leading edge. Hence, the *Present Method* when applied to a simple case like steady flows gives very good results for the pressure distribution, C_p, along the delta wing.

3.3.2 Results of Unsteady Supersonic Flow

The wing is assumed to have translational oscillations defined as

$$h(t) = c\hat{h}e^{i\omega t}$$

Thus, equation (3.22) becomes

$$\hat{W}(x_{1s}, x_{2s}) = i\lambda\hat{h} \tag{3.53}$$

where

- $\hat{h} = 0.1$;
- $\omega = 10$ rads/sec; and
- $\lambda = \frac{\omega c}{U_\infty}$.

The results obtained from the *Frequency Expansion Method* and the *Present Method* differ due to differences in the expansion of e^{-ikx_1}. To gain confidence in the pressure coefficient results obtained by the *Present Method*, as a first step, only the reduced axial velocity, $\hat{u}$, from both methods are compared because the velocity is independent of the expansion of e^{-ikx_1}.

The reduced velocity, $\hat{u}$ or $\frac{\partial\hat{\varphi}}{\partial x_1}$, in Carafoli et al. (1969) (equation 10.61b) is written as:

$$\hat{u} = \left(-\frac{2\hat{h}l}{\pi\sqrt{B^2l^2-1}}\right)\left\{\left[\cos^{-1}\sqrt{\frac{(1-By)(1+Bl)}{2B(l-y)}}\right]-\left[\cos^{-1}\sqrt{\frac{(1+By)(1+Bl)}{2B(l+y)}}\right]\right\} \tag{3.54}$$

The above equation is compared to the following:

$$\hat{u} = \frac{\partial\hat{\varphi}}{\partial x_1} = Real\,\hat{u} + i\,Imag\,\hat{u} \tag{3.55}$$

where

$$\begin{aligned} Real\,\hat{u} &= Real\,\hat{u}_1 + Real\,\hat{u}_2 \\ Imag\,\hat{u} &= Imag\,\hat{u}_1 + Imag\,\hat{u}_2 \end{aligned} \tag{3.56}$$

The components of equation (3.56) are obtained using equations (3.8), (3.32), and (3.36) to give:

$$\begin{aligned} Real\,\hat{u}_1 = \int_{-\frac{1}{B}}^{y} \left[\frac{l\sin(kX_1)\cos\left(\frac{K}{B}\bar{R}X_1\right)}{(l-Y)} - \frac{Bl\sin(kX_1B)}{(Bl+1)} \right] \frac{dY}{\sqrt{1-B^2Y^2}} \\ + \frac{Bl\sin(kX_1B)}{(Bl+1)}\left(\sin^{-1}(By) + \frac{\pi}{2}\right) \\ Imag\,\hat{u}_1 = \int_{-\frac{1}{B}}^{y} \left[\frac{l\cos(kX_1)\cos\left(\frac{K}{B}\bar{R}X_1\right)}{(l-Y)} - \frac{Bl\cos(kX_1B)}{(Bl+1)} \right] \frac{dY}{\sqrt{1-B^2Y^2}} \\ + \frac{Bl\cos(kX_1B)}{(Bl+1)}\left(\sin^{-1}(By) + \frac{\pi}{2}\right) \end{aligned} \tag{3.57}$$

$Real\ \hat{u}_2$ and $Imag\ \hat{u}_2$ can be similarly obtained. The real and imaginary expressions given above are substituted into equation (3.56) to obtain $Real\ \hat{u}$ and $Imag\ \hat{u}$. These are then substituted into equation (3.55) to obtain velocity, $\hat{u}$.

As seen in Figure 3.4(a), the imaginary part of the reduced velocity, $Imag\ \hat{u}$, obtained from the *Present Method* and the *Frequency Expansion Method* are identical (also see Table 2, Appendix B). Hence, it can be said that the methodology adopted in this study is acceptable. The real part of the reduced velocity, $Real\ \hat{u}$, obtained from the *Present Method* is presented in Figure 3.4(b). We cannot obtain $Real\ \hat{u}$ for the *Frequency Expansion Method* because as discussed earlier, this method is an approximate one which ignores the higher orders of k in the expansion of e^{-ikx_1}, unlike the *Present Method*. Therefore, $Real\ \hat{u}$ does not exist in the *Frequency Expansion Method* but exists for the *Present Method*.

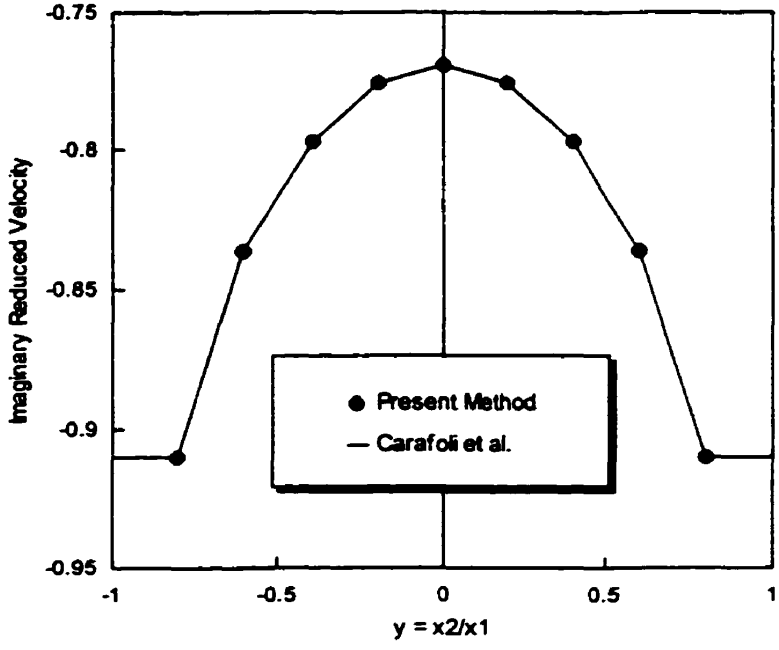

Figure 3.4(a): Comparison of Imaginary $\hat{u}$: Unsteady Flow

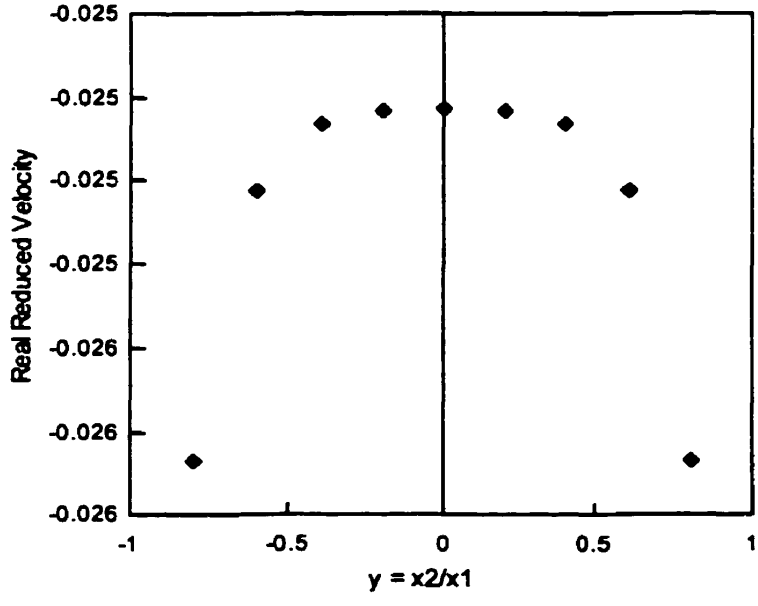

Figure 3.4(b): Real $\hat{u}$ Using *Present Method*: Unsteady Flow

The coefficient of pressure distribution along the delta wing is now obtained using both methods. To obtain this distribution, first substitute equation (3.53) into the equation for the reduced potential, $\hat{\varphi}$, and the reduced velocity, $\hat{u}$. Next expand e^{-ikX_1}. Finally, separate the real and imaginary parts of the result to get

$$Real\, I_1 = \int_{-\frac{1}{B}}^{y} \left\{ \frac{KB}{M_\infty(K^2\bar{R}^2 - k^2B^2)} \left[\frac{K}{B}\bar{R}\cos(kX_1)\sin\left(\frac{K}{B}\bar{R}X_1\right) - k\sin(kX_1)\cos\left(\frac{K}{B}\bar{R}X_1\right) \right] \right.$$
$$\left. + \frac{l\sin(kX_1)\cos\left(\frac{K}{B}\bar{R}X_1\right)}{(l-Y)} - \left[\left(\frac{K}{BM_\infty k} + \frac{Bl}{Bl+1} \right) \sin(X_1B) \right] \right\} \frac{dY}{\sqrt{1-B^2Y^2}}$$
$$+ \left[\left(\frac{K}{BM_\infty k} + \frac{Bl}{Bl+1} \right) \sin(X_1B) \right] \left(\sin^{-1}(By) + \frac{\pi}{2} \right) \tag{3.58a}$$

$$Imag\, I_1 = \int_{-\frac{1}{B}}^{y} \left\{ \frac{KB}{M_\infty(K^2\bar{R}^2 - k^2B^2)} \left[-k\cos(kX_1)\cos\left(\frac{K}{B}\bar{R}X_1\right) - \left(\frac{K}{B}\bar{R}\right)\sin(kX_1)\sin\left(\frac{K}{B}\bar{R}X_1\right) \right] \right.$$
$$\left. + \frac{l\cos(kX_1)\cos\left(\frac{K}{B}\bar{R}X_1\right)}{(l-Y)} - \left[\left(\frac{K}{BM_\infty k} + \frac{Bl}{Bl+1} \right) \cos(X_1B) \right] \right\} \frac{dY}{\sqrt{1-B^2Y^2}}$$
$$+ \left[\left(\frac{K}{BM_\infty k} + \frac{Bl}{Bl+1} \right) \cos(X_1B) \right] \left(\sin^{-1}(By) + \frac{\pi}{2} \right) \tag{3.58b}$$

Real I_2 and *Imag* I_2 are similarly obtained. The real and imaginary expressions given above are substituted into equation (3.42) to obtain *Real F* and *Imag F*. These are then substituted into equation (3.39) to obtain *Real* $\hat{C}_p$ and *Imag* $\hat{C}_p$.

The real and imaginary parts of $\hat{C}_p$ are listed in Table B.3 for various values of $y = \frac{x_2}{x_1}$. The solution for $\hat{C}_p$ is obtained with the *Present Method* equation (3.29) and with the *Frequency Expansion Method* of Carafoli et al. (1969: equation 10.64). The results obtained by the two methods are shown in Figure 3.5(a).

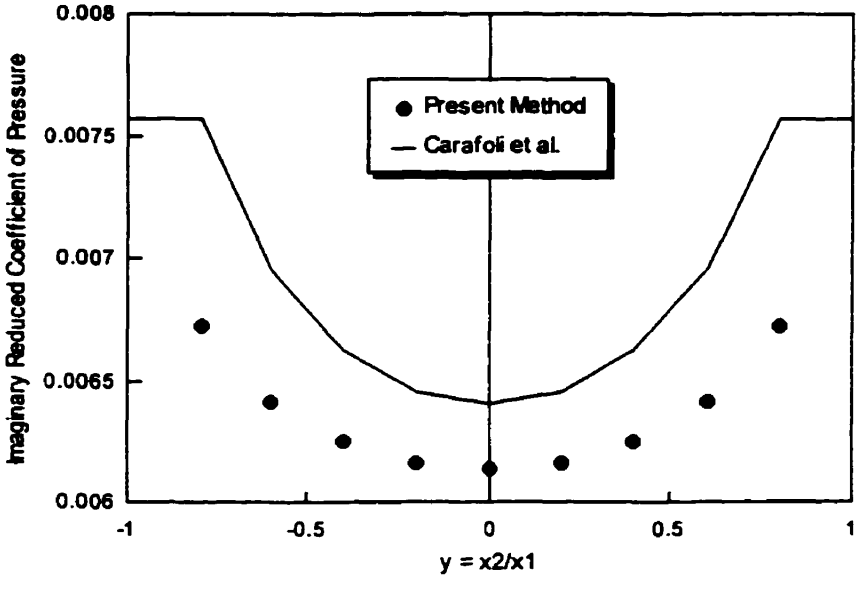

Figure 3.5(a): Comparison of Imaginary $\hat{C}_p$: Unsteady Flow

As seen from Figure 3.5(a), the expected trend for the pressure distribution along the wing in the unsteady case is obtained. Again, *Real* $\hat{C}_p$ does not exist in the *Frequency Expansion Method* but exists for the *Present Method*. The real part of $\hat{C}_p$ is hence only obtained for the *Present Method* which is presented in Figure 3.5(b) (also see Table B.3). However, the magnitudes of *Real* $\hat{C}_p$ obtained using the *Present Method* are seen to be small.

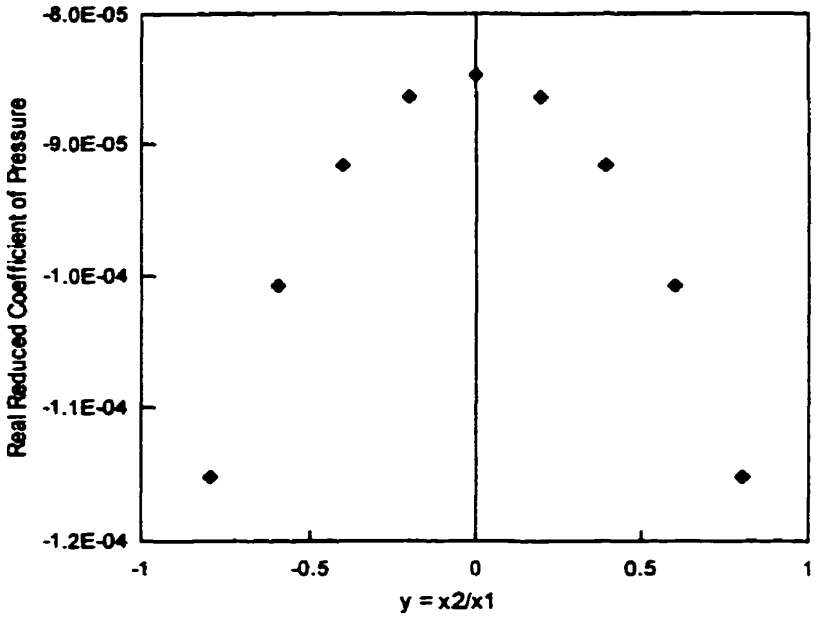

Figure 3.5(b): Real $\hat{C}_p$ Using *Present Method*: Unsteady Flow

Therefore, the coefficient of pressure, $\hat{C}_p$, for an unsteady supersonic flow along the wing obtained from the *Present Method* is acceptable and, due to its handling of the expansion term, e^{-ikx_1}, more accurate. Hence the hybrid analytical-numerical method developed in this section to determine the coefficient of pressure distribution along the delta wing will be used to determine the aerodynamic loading on the wing and the resultant generalized forces in the next section.

3.4 Generalized Forces due to Aerodynamic Loading

In the previous section a method to determine the pressure distribution for an unsteady flow over the wing was developed. In this section the generalized force, $\{Q_{aero}\}$, due to unsteady supersonic aerodynamic loading on the delta wing will be determined.

It is assumed that a flexular oscillation of the plane wing exists. The reduced potential of the source distribution on the plane of the wing is again given by equation (3.28) and the coefficient of pressure and the reduced coefficient of pressure are given by equations (3.12) and (3.29) respectively.

Now, h is the small transverse motion of the wing. The small transverse structural displacement, w, is in the z-axis (or in this case the x_3-axis) as defined in Chapter 2 and given by equation (2.4). A coordinate transformation from the (x, y) coordinate system to the (x_1, x_2) coordinate system on equation (2.4) is made and then h is set equal to w to get

$$h(x_1, x_2, t) = \sum_{r=1}^{M} \sum_{s=1}^{N} \Phi_r(x_2)\Psi_s(x_1)q_{rs}(t) \tag{3.59}$$

The reduced small transverse motion can now be denoted as $\hat{h}$. Let $\hat{h}$ be placed at a pulsating source point (x_{1s}, x_{2s}) to give

$$\hat{h} = \sum_{r=1}^{M} \sum_{s=1}^{N} \Phi_r(x_{2s})\Psi_s(x_{1s})\hat{q}_{rs} \tag{3.60}$$

where Φ_r and Ψ_s are the chosen shape functions as defined in Chapter 2 by equations (2.7) and (2.8) respectively. Also, $\hat{q}_{rs}$ are the reduced generalized displacements defined as

$$\hat{q}_{rs} = \frac{q_{rs}}{e^{i\omega t}} \tag{3.61}$$

where ω is the frequency of oscillation of the wing over time, t.

Therefore, for this case, the reduced vertical velocity from equation (3.18) can be written as

$$\hat{W}(x_1, x_2) = \frac{\partial \hat{h}}{\partial x_1} + i\lambda\hat{h} \tag{3.62}$$

where λ is defined by equation (3.11) and $\hat{h}$ is the small transverse motion of the wing given by equation (3.60).

The chosen shape functions are now rewritten in the new coordinate system as the following

$$\Phi_r(x_{2s}) = \left(\frac{x_{2s}}{l}\right)^{r+1} \tag{3.63}$$

$$\Psi_s(x_{1s}) = \left[\left(1 - \frac{x_{2s}}{l}\right)^2 \left(\frac{1}{2} - \frac{c - x_{1s}}{c\left(1 - \frac{x_{2s}}{l}\right)}\right)\right]^{s-1} \tag{3.64}$$

where l is the semi-span and c is the chord.

As was done in the previous section, the (x_{1s}, x_{2s}) coordinate system is transformed to the (X, Y) coordinate system using equation (3.30). Also, the reduced potential is again given by equation (3.33) and is rewritten below as a reminder

$$\hat{\varphi}(x_1, x_2) = -\frac{1}{\pi}\int\int \hat{W}(x_{1s}, x_{2s}) e^{-ikX} \cos\left(\frac{k}{M_\infty} X\bar{R}\right) \frac{dXdY}{\bar{R}} \tag{3.65}$$

where $\hat{W}(x_{1s}, x_{2s})$ is the vertical velocity, k is the reduced frequency defined by equation (3.8), and $\bar{R}$ is defined by equation (3.32).

Equations (3.63) and (3.64) are now respectively written in the (X,Y) coordinate system as

$$\Phi_r(x_2 - XY) = \left(\frac{x_2 - XY}{l}\right)^{r+1} \tag{3.66}$$

$$\Psi_s(x_1 - X) = \left[\frac{a + 2l(x_2 - l)X + 2(lx_1 - cx_2)XY - 2lX^2Y + cX^2Y^2}{2l^2c}\right]^{s-1} \tag{3.67}$$

where

$$a = -l^2c + cx_2^2 + 2l^2x_1 - 2lx_1x_2$$

The vertical velocity is expanded in terms of the modes of vibration. As seen from equation (3.67), expanding the free-free shape functions for more than two modes, that is $s > 2$, gives an extremely complicated expression for the same. Therefore, as a simplification we will consider expanding the vertical velocity in only two modes for both the clamped-free and free-free directions. As a result we get the following concise forms for equations (3.66) and (3.67):

$$\Phi_r(x_2 - XY) = \sum_{mh=0}^{r+1} \sum_{np=0}^{r+1} A_{mh,\,np} X^{mh} Y^{np} \tag{3.68}$$

$$\Psi_s(x_1 - X) = \sum_{ki=0}^{s} \sum_{mp=0}^{s} B_{ki,\,mp} X^{ki} Y^{mp} \tag{3.69}$$

where $A_{mh,\,np}$ and $B_{ki,\,mp}$ are the coefficients of X and Y in the expansion of the vertical velocity in terms of modes. These coefficients and their derivatives are listed in Tables 4(a)-4(d) of Appendix B for $r = 1$, $r = 2$, $s = 1$ and $s = 2$ respectively.

The vertical velocity from equations (3.60), (3.62), (3.68) and (3.69) of a plane wing for which a flexular oscillation exists is finally written as

$$\hat{W}(x_{1s}, x_{2s}) = S_u\{B_{21} + i\lambda B_2\}X^{mhk}Y^{mhp}\hat{q}_{rs} \tag{3.70}$$

where

$$S_u = \sum_{r=1}^{M}\sum_{s=1}^{N}\sum_{mh=0}^{r+1}\sum_{np=0}^{r+1}\sum_{ki=0}^{s}\sum_{mp=0}^{s} \tag{3.71}$$

$$B_2 = A_{mh,\,np}\,B_{ki,\,mp} \tag{3.72}$$

$$B_{21} = A_{mh,\,np}\frac{\partial B_{ki,\,mp}}{\partial x_1} \tag{3.73}$$

$$mhk = mh + ki \tag{3.74}$$

$$mhp = np + mp \tag{3.75}$$

where λ is defined by equation (3.11) and $\hat{q}_{rs}$ are the reduced generalized displacements given by equation (3.61).

Substituting (3.70) in (3.65), we get the reduced potential as

$$\hat{\varphi}(x_1, x_2) = -S_u\frac{(B_{21} + i\lambda B_2)}{2\pi}\left[\int\int X^{mhk}Y^{mhp}\{(\cos aX + \cos bX) - i\sin(aX + \sin bX)\}\frac{dXdY}{\bar{R}}\right]\hat{q}_{rs} \tag{3.76}$$

where

$$\begin{aligned} a &= k + \frac{K}{B}\bar{R} \\ b &= k - \frac{K}{B}\bar{R} \end{aligned} \tag{3.77}$$

Equation (3.76) is valid both inside and outside the Mach cone. We will first determine the

reduced potential and reduced velocity inside the Mach cone. As was done in Chapter 2, only one side of the wing is modelled, due to symmetry. However, inside the Mach cone, the source distribution on one side of the delta wing has an effect on the other side of the wing. Therefore, the limits of integration over X and Y, inside the Mach cone, are again given by equation (3.34).

To integrate over X we will use the following standard integral as given by Gradshteyn and Ryzhik (1994)

$$\int x^n \sin ax\, dx = -\sum_{k=0}^{n} k!\binom{n}{k}\frac{x^{n-k}}{a^{k+1}}\cos\left(ax+\frac{k\pi}{2}\right) \tag{3.78}$$

$$\int x^n \cos ax\, dx = \sum_{k=0}^{n} k!\binom{n}{k}\frac{x^{n-k}}{a^{k+1}}\sin\left(ax+\frac{k\pi}{2}\right) \tag{3.79}$$

Therefore,

$$\int_0^{X_1} X^{mhk}\sin ax\, dX = -\sum_{mj=0}^{mhk} mj!\binom{mhk}{mj}\left\{\frac{x_1(l-y)}{(l-Y)}\right\}^{mhk-mj}\frac{1}{a^{mj+1}}\cos\left(aX_1+\frac{mj\pi}{2}\right) \tag{3.80}$$

$$\int_0^{X_1} X^{mhk}\cos ax\, dX = \sum_{mj=0}^{mhk} mj!\binom{mhk}{mj}\left\{\frac{x_1(l-y)}{(l-Y)}\right\}^{mhk-mj}\frac{1}{a^{mj+1}}\sin\left(aX_1+\frac{mj\pi}{2}\right) \tag{3.81}$$

The other integrals in X in equation (3.76) are similarly solved using equations (3.78) and (3.79). The semi-analytical expression in Y is now determined using equations (3.37a) and (3.37b) as was done in section 3.2. Let

$$\begin{aligned} A_1 &= aX_1 + \frac{mj\pi}{2} \\ A_2 &= bX_1 + \frac{mj\pi}{2} \\ A_3 &= aX_2 + \frac{mj\pi}{2} \\ A_4 &= bX_2 + \frac{mj\pi}{2} \end{aligned} \tag{3.82}$$

where X_1 and X_2 are given by equation (3.34), and a and b are given by equation (3.77).

On evaluation and simplification of these equations, we can now write equation (3.76) as

$$\hat{\varphi}(x_1, x_2) = -S_u \frac{(B_{21} + i\lambda B_2)}{2\pi} \sum_{mj=0}^{mhk} \frac{mhk!}{(mhk - mj)!} [(I_1 + I_2) - i(I_3 + I_4)] \hat{q}_{rs} \qquad (3.83)$$

where

$$I_1 = \{x_1(l-y)\}^{mhk-mj} \int_{-\frac{1}{B}}^{y} \left\{ \frac{Y^{mhp}}{(l-Y)^{mhk-mj}} \left(\frac{\sin A_1}{a^{mj+1}} + \frac{\sin A_2}{b^{mj+1}} \right) - a_1 \right\} \frac{dY}{\bar{R}} \qquad (3.84a)$$

$$+ a_1 Q_1$$

$$I_2 = \{x_1(l+y)\}^{mhk-mj} \int_{y}^{\frac{1}{B}} \left\{ \frac{Y^{mhp}}{(l+Y)^{mhk-mj}} \left(\frac{\sin A_3}{a^{mj+1}} + \frac{\sin A_4}{b^{mj+1}} \right) - a_2 \right\} \frac{dY}{\bar{R}} \qquad (3.84b)$$

$$+ a_2 Q_2$$

$$I_3 = -\{x_1(l-y)\}^{mhk-mj} \int_{-\frac{1}{B}}^{y} \left\{ \frac{Y^{mhp}}{(l-Y)^{mhk-mj}} \left(\frac{\cos A_1}{a^{mj+1}} + \frac{\cos A_2}{b^{mj+1}} \right) - a_3 \right\} \frac{dY}{\bar{R}} \qquad (3.84c)$$

$$+ a_3 Q_1$$

$$I_4 = -\{x_1(l+y)\}^{mhk-mj} \int_{y}^{\frac{1}{B}} \left\{ \frac{Y^{mhp}}{(l+Y)^{mhk-mj}} \left(\frac{\cos A_3}{a^{mj+1}} + \frac{\cos A_4}{b^{mj+1}} \right) - a_4 \right\} \frac{dY}{\bar{R}} \qquad (3.84d)$$

$$+ a_4 Q_2$$

where l is again the semi-span of the wing; the constants a and b are given by equation

(3.77); B and $\bar{R}$ are defined by equations (3.9) and (3.32) respectively; and where

$$\begin{aligned} Q_1 &= \sin^{-1}(By) + \frac{\pi}{2} \\ Q_2 &= \frac{\pi}{2} - \sin^{-1}(By) \end{aligned} \tag{3.85}$$

The constants a_1, a_2, a_3 and a_4 in equations (3.84a) to (3.84d) are defined below

$$a_1 = \frac{2}{k^{mj+1}}\left(-\frac{1}{B}\right)^{mhp}\left(\frac{B}{Bl+1}\right)^{mhk-mj}\sin\left(\frac{Bkx_1(l-y)}{Bl+1} + \frac{mj\pi}{2}\right) \tag{3.86a}$$

$$a_2 = \frac{2}{k^{mj+1}}\left(\frac{1}{B}\right)^{mhp}\left(\frac{B}{Bl+1}\right)^{mhk-mj}\sin\left(\frac{Bkx_1(l+y)}{Bl+1} + \frac{mj\pi}{2}\right) \tag{3.86b}$$

$$a_3 = \frac{2}{k^{mj+1}}\left(-\frac{1}{B}\right)^{mhp}\left(\frac{B}{Bl+1}\right)^{mhk-mj}\cos\left(\frac{Bkx_1(l-y)}{Bl+1} + \frac{mj\pi}{2}\right) \tag{3.86c}$$

$$a_4 = \frac{2}{k^{mj+1}}\left(\frac{1}{B}\right)^{mhp}\left(\frac{B}{Bl+1}\right)^{mhk-mj}\cos\left(\frac{Bkx_1(l+y)}{Bl+1} + \frac{mj\pi}{2}\right) \tag{3.86d}$$

Differentiate the final equation for reduced potential, equation (3.83), to obtain $\hat{u}$. Therefore,

$$\begin{aligned} \frac{\partial\hat{\varphi}}{\partial x_1} = -\frac{1}{2\pi}S_u\Bigg\{&\left(\frac{\partial B_{21}}{\partial x_1} + i\lambda\frac{\partial B_2}{\partial x_1}\right)\sum_{mj=0}^{mhk}\frac{mhk!}{(mhk-mj)!}[(I_1+I_2) - i(I_3+I_4)] \\ &+ (B_{21} + i\lambda B_2)\sum_{mj=0}^{mhk}\frac{mhk!}{(mhk-mj)!}\left[\left(\frac{\partial I_1}{\partial x_1} + \frac{\partial I_2}{\partial x_1}\right) - i\left(\frac{\partial I_3}{\partial x_1} + \frac{\partial I_4}{\partial x_1}\right)\right]\Bigg\}\hat{q}_{rs} \end{aligned} \tag{3.87}$$

where

$$\frac{\partial B_2}{\partial x_1} = \frac{\partial A_{mh,\,np}}{\partial x_1}B_{ki,\,mp} + A_{mh,\,np}\frac{\partial B_{ki,\,mp}}{\partial x_1} \tag{3.88}$$

$$\frac{\partial B_{21}}{\partial x_1} = \frac{\partial A_{mh,\,np}}{\partial x_1}\frac{\partial B_{ki,\,mp}}{\partial x_1} + A_{mh,\,np}\frac{\partial^2 B_{ki,\,mp}}{\partial x_1^2} \tag{3.89}$$

In equation (3.87), I_1, I_2, I_3 and I_4 are given by equations (3.84a), (3.84b), (3.84c) and (3.84d) respectively. Expressions for $\frac{\partial I_1}{\partial x_1}$, $\frac{\partial I_2}{\partial x_1}$, $\frac{\partial I_3}{\partial x_1}$ and $\frac{\partial I_4}{\partial x_1}$ can be found in Appendix B. Hence, the reduced potential, $\hat{\varphi}$, and the reduced velocity, $\frac{\partial \hat{\varphi}}{\partial x_1}$, inside the Mach cone have been determined. The same can be similarly determined outside the Mach cone.

Outside the Mach cone, the source distribution on one side of the wing has no effect on the other side. The limits of integration outside the Mach cone therefore are

$$-1/B \text{ to } 1/B$$

Hence the equations for the reduced potential and the reduced velocity, equations (3.76) and (3.87), for outside the Mach cone respectively become

$$\hat{\varphi}(x_1, x_2) = -S_u \frac{(B_{21} + i\lambda B_2)}{2\pi} \sum_{mj=0}^{mhk} \frac{mhk!}{(mhk-mj)!}[I_{11} - iI_{12}]\hat{q}_{rs} \tag{3.90}$$

and

$$\frac{\partial \hat{\varphi}}{\partial x_1} = -\frac{1}{2\pi} S_u \left\{ \left(\frac{\partial B_{21}}{\partial x_1} + i\lambda \frac{\partial B_2}{\partial x_1}\right) \sum_{mj=0}^{mhk} \frac{mhk!}{(mhk-mj)!}[I_{11} - iI_{12}] \right. \tag{3.91}$$
$$\left. + (B_{21} + i\lambda B_2) \sum_{mj=0}^{mhk} \frac{mhk!}{(mhk-mj)!}\left[\frac{\partial I_{11}}{\partial x_1} - i\frac{\partial I_{12}}{\partial x_1}\right] \right\} \hat{q}_{rs}$$

where B_2, B_{21}, $\frac{\partial B_2}{\partial x_1}$, and $\frac{\partial B_{21}}{\partial x_1}$ are given by equations (3.72), (3.73), (3.88), and (3.89), respectively. The values for the same for various modes are listed in Table 4 of Appendix B. Additionally, λ is given by equation (3.11), and

$$I_{11} = \{x_1(l-y)\}^{mhk-mj} \int_{-\frac{1}{B}}^{\frac{1}{B}} \left\{ \frac{Y^{mhp}}{(l-Y)^{mhk-mj}} \left(\frac{\sin A_1}{a^{mj+1}} + \frac{\sin A_2}{b^{mj+1}} \right) - a_1 - a_5 \right\} \frac{dY}{\bar{R}} \qquad (3.92a)$$

$$+ (a_1 + a_5)\pi$$

$$I_{12} = -\{x_1(l-y)\}^{mhk-mj} \int_{-\frac{1}{B}}^{\frac{1}{B}} \left\{ \frac{Y^{mhp}}{(l-Y)^{mhk-mj}} \left(\frac{\cos A_1}{a^{mj+1}} + \frac{\cos A_2}{b^{mj+1}} \right) - a_3 - a_6 \right\} \frac{dY}{\bar{R}} \qquad (3.92b)$$

$$+ (a_3 + a_6)\pi$$

where A_1 and A_2 are given by equation (3.82), and the constants a_1 and a_3 are defined by equations (3.86a) and (3.86c). Also,

$$a_5 = \frac{2}{k^{mj+1}} \left(\frac{1}{B} \right)^{mhp} \left(\frac{B}{Bl-1} \right)^{mhk-mj} \sin\left(\frac{Bkx_1(l-y)}{Bl-1} + \frac{mj\pi}{2} \right) \qquad (3.93a)$$

$$a_6 = \frac{2}{k^{mj+1}} \left(\frac{1}{B} \right)^{mhp} \left(\frac{B}{Bl-1} \right)^{mhk-mj} \cos\left(\frac{Bkx_1(l-y)}{Bl-1} + \frac{mj\pi}{2} \right) \qquad (3.93b)$$

Equations (3.92a) and (3.92b) are differentiated with respect to x_1 to yield $\frac{\partial I_{11}}{\partial x_1}$ and $\frac{\partial I_{12}}{\partial x_1}$. Please see Appendix B for these expressions.

Now that the equations of the reduced potential and reduced velocity both inside and outside the Mach cone have been determined, the reduced coefficient of pressure distribution, $\hat{C}_p$, on the entire wing can be obtained. Substituting equations (3.83) and (3.87) into equation (3.29), $\hat{C}_p$ is obtained inside the Mach cone. Similarly, by substituting equations (3.90) and (3.91) into (3.29), $\hat{C}_p$ is obtained outside the Mach cone. The reduced coefficient of pressure both inside and outside the Mach cone can again be written in the complex form given by equation (3.38). The steps needed to solve this complex form of the reduced coefficient of pressure are described in section 3.1.

The pressure distribution for the upper surface of the wing, in dimensional form, is given by the following

$$p(x_1, x_2) = \frac{1}{2}\rho_\infty U_\infty^2 C_p(x_1, x_2, t) + p_\infty$$

where ρ_∞ is the density of the free stream, p_∞ is the free stream pressure, U_∞ is the free stream velocity and $C_p(x_1, x_2, t)$ is given by equation (3.12). As the reduced coefficient of pressure for the delta wing has already been determined, the dimensional pressure distribution for one side the upper surface is now written as

$$p(x_1, x_2) = \frac{1}{2}\rho_\infty U_\infty^2 \hat{C}_p(x_1, x_2) e^{i\omega t} + p_\infty \tag{3.94}$$

Since $\hat{C}_{p,\,lower} = -\ \hat{C}_{p,\,upper}$, the net pressure on the wing is written as,

$$\Delta p(x_1, x_2) = 2\left[\frac{1}{2}\rho_\infty U_\infty^2 \hat{C}_p(x_1, x_2) e^{i\omega t}\right]$$

where $\hat{C}_p(x_1, x_2)$ is given by equation (3.38), and ω is the frequency of periodic motion over time, t.

The pressure distribution given by equation (3.94) is nothing but the aerodynamic loading on the wing. Therefore, the generalized forces due to this aerodynamic loading can be written as

$$\{Q_{aero}\} = \sum_{m=1}^{M}\sum_{n=1}^{N}\int_0^l\int_0^{c\left(1-\frac{x}{l}\right)} \rho_\infty U_\infty^2 C_p(x_1, x_2, t)\Phi_m(x)\Psi_n(y)dxdy \tag{3.95}$$

where m and n identify the shape functions in the clamped-free and free-free directions

respectively. In a non-dimensional form the above equation becomes

$$\{Q_{aero}\} = \sum_{m=1}^{M} \sum_{n=1}^{N} \int_0^1 \int_0^{(1-\xi)} \rho_\infty U_\infty^2 C_p(x_1, x_2, t) \Phi_m(\xi) \Psi_n(\eta) lc d\xi d\eta \qquad (3.96)$$

where $\Phi_m(\xi)$ and $\Psi_n(\eta)$ are defined by equations (2.7) and (2.8) respectively. The pressure distribution is calculated as shown earlier at various receiving points on the wing defined by (x_1, x_2). Now the shape functions are calculated on the same points as the pressure in order to couple the equations.

To solve equation (3.96), a numerical integration over the triangular element has to be carried out. The following general formula for numerical integration of a function G over a triangle area, as shown in both Cowper(1972) and Reddy (1993), is used to integrate equation (3.96):

$$\int_{\hat{\Omega}_t} G(\xi, \eta) d\xi d\eta = \int_{\Omega_t} \hat{G}(L_1, L_2, L_3) dL_1 dL_2 \qquad (3.97)$$

which can be approximated by the Gaussian quadrature formula as

$$\int_{\Omega_t} \hat{G}(L_1, L_2, L_3) dL_1 dL_2 \approx \frac{1}{2} \sum_{I=1}^{NIP} W_I \hat{G}(S_I) \qquad (3.98)$$

where (L_1, L_2, L_3) is the transformed coordinate system known as the area coordinate system (see Reddy (1993) for details); *NIP* are the total number of integration points; and W_I and S_I denote the weights and integration points of the quadrature rule respectively.

On transforming the non-dimensional coordinate system (ξ, η) to the area coordinate system (L_1, L_2, L_3), we get

$$\begin{aligned} \xi &= L_2 \\ \eta &= L_3 \\ L_1 &= 1 - L_2 - L_3 \end{aligned} \tag{3.99}$$

Hence, equation (3.96) remains unchanged as

$$\{Q_{aero}\} = \sum_{m=1}^{M} \sum_{n=1}^{N} \int_0^1 \int_0^{(1-\xi)} \rho_\infty U_\infty^2 C_p(x_1, x_2, t) \Phi_m(\xi) \Psi_n(\eta) lc d\xi d\eta \tag{3.100}$$

Rewriting equation (3.100) using the quadrature formula, we get

$$\{Q_{aero}\} = \sum_{i=1}^{MN} \left[\frac{1}{2} \sum_{l=1}^{NIP} W_l \hat{G}(S_l) \right] \tag{3.101}$$

where

$$\hat{G} = lc\rho_\infty U_\infty^2 C_p(x_1, x_2, t) \Phi_m(\xi) \Psi_n(\eta) \tag{3.102}$$

$C_p(x_1, x_2, t)$ is calculated using the 10-point Gaussian quadrature as was discussed earlier. The pressure calculated at various points (x_1, x_2) on the wing is multiplied by the shape functions calculated at the same points. The overall numerical integration is then carried out using a 13-point (and degree of precision 7) Gaussian quadrature formula for triangular areas as shown in Cowper (1972). The list of weights, W_l, and the location of the area coordinates (L_1, L_2, L_3) for this 13-point Gaussian quadrature can be found in Cowper (1972). This list is valid for triangles of any shape.

$\{Q_{aero}\}$ is a complicated function of ω and time t. Hence it cannot be broken down into simple coefficients of 1 , ω and ω^2. In other words, the matrix $[A]$ in the state-space equation for the present case is extremely complicated. However, we can still solve these generalized forces by first defining the generalized displacements using equation (3.61) as

$$\{\tilde{q}_{rs}\} = (\{q^c_{rs}\}\cos\omega t + \{q^s_{rs}\}\sin\omega t) + i(\{q^c_{rs}\}\sin\omega t - \{q^s_{rs}\}\cos\omega t) \qquad (3.103)$$

where '~' above $\{q_{rs}\}$ denotes that both the real and imaginary components of the generalized displacements are present, and $\{q^c_{rs}\}$ and $\{q^s_{rs}\}$ are the components of the vector, $\{\tilde{q}_{rs}\}$. Also let

$$D = Real(\hat{C}_p(x_1, x_2)) \qquad (3.104)$$

where

$$Real(\hat{C}_p(x_1, x_2)) = -\frac{1}{\pi}[\cos(kx_1)(Real\ \hat{\varphi} + Real\ \hat{u}) - \sin(kx_1)(Imag\ \hat{\varphi} + Imag\ \hat{u})] \qquad (3.105)$$

and where k is the reduced frequency. For convenience, we write the real and imaginary components of the reduced potential and velocity in the following format:

$$Real\ \hat{\varphi} = \sum_{r=1}^{M}\sum_{s=1}^{N} \hat{\varphi}_R\,\hat{q}_{rs} \qquad Real\ \hat{u} = \sum_{r=1}^{M}\sum_{s=1}^{N} \hat{u}_R\,\hat{q}_{rs}$$

$$Imag\ \hat{\varphi} = \sum_{r=1}^{M}\sum_{s=1}^{N} \hat{\varphi}_I\,\hat{q}_{rs} \qquad Imag\ \hat{u} = \sum_{r=1}^{M}\sum_{s=1}^{N} \hat{u}_I\,\hat{q}_{rs}$$

where the equations for $\hat{\varphi}_R$, $\hat{\varphi}_I$, $\hat{u}_R$ and $\hat{u}_I$ are given below for both inside and outside the Mach cone.

- Inside the Mach cone, the following equations are valid:

$$\hat{\varphi}_R = S_{u1}\frac{K}{BM_\infty}\left[B_{21}\sum_{mj=0}^{mhk} G(I_3 + I_4) - \lambda B_2 \sum_{mj=0}^{mhk} G(I_1 + I_2)\right] \qquad (3.106a)$$

$$\hat{\Phi}_I = S_{u1}\frac{K}{BM_\infty}\left[B_{21}\sum_{mj=0}^{mhk} G(I_1+I_2)+\lambda B_2\sum_{mj=0}^{mhk} G(I_3+I_4)\right] \tag{3.106b}$$

$$\hat{u}_R = S_{u1}\left\{\left[\frac{\partial B_{21}}{\partial x_1}\sum_{mj=0}^{mhk} G(I_1+I_2)+\lambda\frac{\partial B_2}{\partial x_1}\sum_{mj=0}^{mhk} G(I_3+I_4)\right]\right. \tag{3.106c}$$
$$\left.+\left[B_{21}\sum_{mj=0}^{mhk} G\left(\frac{\partial I_1}{\partial x_1}+\frac{\partial I_2}{\partial x_1}\right)+\lambda B_2\sum_{mj=0}^{mhk} G\left(\frac{\partial I_3}{\partial x_1}+\frac{\partial I_4}{\partial x_1}\right)\right]\right\}$$

$$\hat{u}_I = S_{u1}\left\{\left[-\frac{\partial B_{21}}{\partial x_1}\sum_{mj=0}^{mhk} G(I_3+I_4)+\lambda\frac{\partial B_2}{\partial x_1}\sum_{mj=0}^{mhk} G(I_1+I_2)\right]\right. \tag{3.106d}$$
$$\left.+\left[-B_{21}\sum_{mj=0}^{mhk} G\left(\frac{\partial I_3}{\partial x_1}+\frac{\partial I_4}{\partial x_1}\right)+\lambda B_2\sum_{mj=0}^{mhk} G\left(\frac{\partial I_1}{\partial x_1}+\frac{\partial I_2}{\partial x_1}\right)\right]\right\}$$

- For points outside the Mach cone, the following equations must be used:

$$\hat{\Phi}_R = S_{u1}\frac{K}{BM_\infty}\left[B_{21}\sum_{mj=0}^{mhk} G\,I_{12}-\lambda B_2\sum_{mj=0}^{mhk} G\,I_{11}\right] \tag{3.107a}$$

$$\hat{\Phi}_I = S_{u1}\frac{K}{BM_\infty}\left[B_{21}\sum_{mj=0}^{mhk} G\,I_{11}+\lambda B_2\sum_{mj=0}^{mhk} G\,I_{12}\right] \tag{3.107b}$$

$$\hat{u}_R = S_{u1}\left\{\left[\frac{\partial B_{21}}{\partial x_1}\sum_{mj=0}^{mhk} G\,I_{11}+\lambda\frac{\partial B_2}{\partial x_1}\sum_{mj=0}^{mhk} G\,I_{12}\right]\right. \tag{3.107c}$$
$$\left.+\left[B_{21}\sum_{mj=0}^{mhk} G\frac{\partial I_{11}}{\partial x_1}+\lambda B_2\sum_{mj=0}^{mhk} G\frac{\partial I_{12}}{\partial x_1}\right]\right\}$$

$$\hat{u}_I = S_{u1}\left\{\left[-\frac{\partial B_{21}}{\partial x_1}\sum_{mj=0}^{mhk} G\,I_{12}+\lambda\frac{\partial B_2}{\partial x_1}\sum_{mj=0}^{mhk} G\,I_{11}\right]\right. \tag{3.107d}$$
$$\left.+\left[-B_{21}\sum_{mj=0}^{mhk} G\frac{\partial I_{12}}{\partial x_1}+\lambda B_2\sum_{mj=0}^{mhk} G\frac{\partial I_{11}}{\partial x_1}\right]\right\}$$

where

$$S_{ul} = \sum_{mh=0}^{r+1} \sum_{np=0}^{r+1} \sum_{ki=0}^{s} \sum_{mp=0}^{s}$$

and

$$G = \frac{mhk!}{(mhk - mj)!}$$

As seen in equation (3.105), $Real(\hat{C}_p(x_1, x_2))$ depends on both the real and imaginary parts of the reduced potential, $\hat{\varphi}$, and the reduced velocity, $\hat{u}$. Therefore, let $\{Q_{aero}\}$ be written in terms of the real and imaginary parts of the reduced potential and reduced velocity. Hence the equation for generalized forces, equation (3.100), is rewritten as the following:

$$\{Q_{aero}\} = Real\,([Z_R(\omega)]\{\tilde{q}_{rs}\} + i[Z_I(\omega)]\{\tilde{q}_{rs}\}) \tag{3.108}$$

In the above equation, $[Z_R(\omega)]$ is of size MN x MN and is of the form

$$Z_{R_{mn,rs}} = \int_0^1 \int_0^{(1-\xi)} \rho_\infty U_\infty^2 D_{R_{rs}} \Phi_m(\xi) \Psi_n(\eta) lc d\xi d\eta \tag{3.109}$$

where

$$D_{R_{rs}} = -\frac{1}{\pi} \cos(kx_1)[\hat{\varphi}_R + \hat{u}_R]$$

Similarly, $[Z_I(\omega)]$ is also of size MN x MN and is defined as

$$Z_{I_{mn,rs}} = \int_0^1 \int_0^{(1-\xi)} \rho_\infty U_\infty^2 D_{I_{rs}} \Phi_m(\xi) \Psi_n(\eta) lc d\xi d\eta \tag{3.110}$$

where

$$D_{I_{rs}} = -\frac{1}{\pi}\sin(kx_1)[\hat{\varphi}_I + \hat{u}_I]$$

The solution of equations (3.109) and (3.110) involves the use of the quadrature formula shown in equation (3.101).

On substituting equation (3.103) in equation (3.108), we get

$$\begin{aligned}\{Q_{aero}\} = {} & [Z_R(\omega)](\{q_{rs}^c\}\cos\omega t + \{q_{rs}^s\}\sin\omega t) \\ & -[Z_I(\omega)](\{q_{rs}^c\}\sin\omega t - \{q_{rs}^s\}\cos\omega t)\end{aligned} \tag{3.111}$$

Hence the generalized forces due to aerodynamic loading have been obtained. The dynamic response of the delta wing due to these forces will be determined in Chapter 5.

In the following chapter the generalized forces due to piezoelectric strips will also be determined.

Chapter 4

Modelling of Piezoelectric Actuators

In the previous chapter a model of the uncontrolled delta wing under supersonic aerodynamic loading was formulated. In principle, piezoelectric actuators can be introduced on the wing in order to control the aeroelastic oscillations of the wing. However, the goal of the present research is only to study the response of the wing in the presence of these actuators but not to develop control schemes. Hence, the study is limited to the examination of the effects of introducing the piezoelectric actuators on the aeroelastic oscillations of the delta wing.

In this chapter, a mathematical model of the PVDF strips distributed on the surface of the wing is developed. The resulting model is appended to equation (2.28) in order to produce a state-space matrix equation of the well-known form,

$$\{\dot{x}\} = [A]\{x\} + [B]\{F\} \tag{4.1}$$

where $[B]$ depends on both the locations and geometric characteristics of the PVDF actuators while $\{F\}$ is the force input vector. Here $\{F\}$ depends on the voltage applied across the thickness of the piezoelectric actuators.

4.1. System Description

The piezoelectric actuators are modelled as PVDF strips bonded to the surface of the wing. The model contains the following assumptions:

- the PVDF strips are homogeneous and isotropic;

- the strips are polarized so as to produce uni-directional strains, i.e., if the piezoelectric constant $d_{31} \neq 0$, then d_{32} and d_{36} must be zero for that strip;
- the strips are perfectly bonded to the structure; and
- the thicknesses of all the PVDF strips are constant.

The assumptions listed above are the same as those given by van Poppel and Misra (1992). Figure 4.1 shows the approximate distribution of the five PVDF strips on the cantilevered triangular plate as used in the present study. Note that the axis convention is the same as

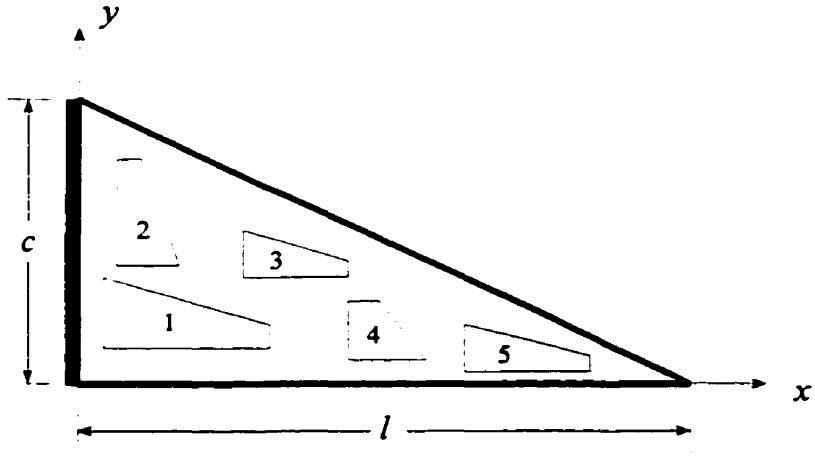

Figure 4.1: Distribution of PVDF Strips on Cantilevered Triangular Plate

that used for the structural analysis in Chapter 2. Also, note that the locations, sizes and number of PVDF strips can be varied so as to attain maximum control of the flutter. In the present study the shape of the strip was chosen to be trapezoidal because it is simpler to manufacture than a more irregular geometry. Also, the trapezoidal shape gives better flexibility in covering a triangular plate as opposed to a rectangular shape for the strips. As shown in Figure 4.2(a), the bottom left corner of the ith strip is located at (x_i, y_i) and the width of the PVDF strip, if polarized in the x-direction, is assumed to be a function of x, namely $b_i(x)$. Similarly, if the strip is polarized in the y-direction, the width of the strip is assumed to be a function of y, namely, $a_i(y)$ as shown in Figure 4.2(b).

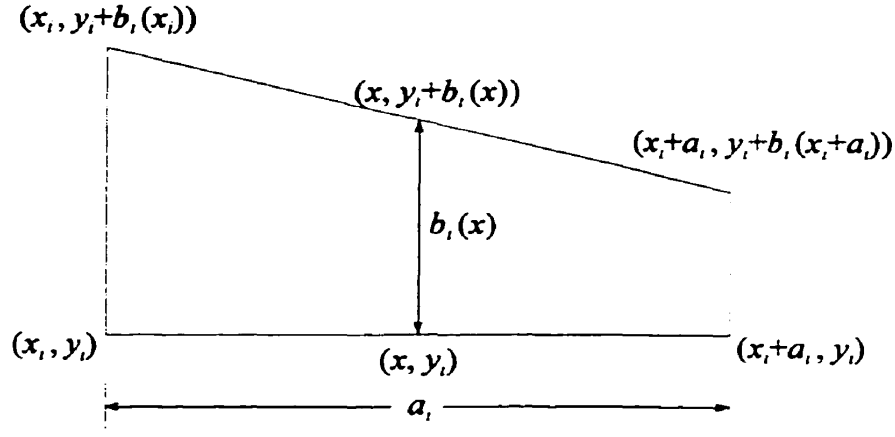

Figure 4.2(a): Shape of PVDF Strip Polarized in the x-direction

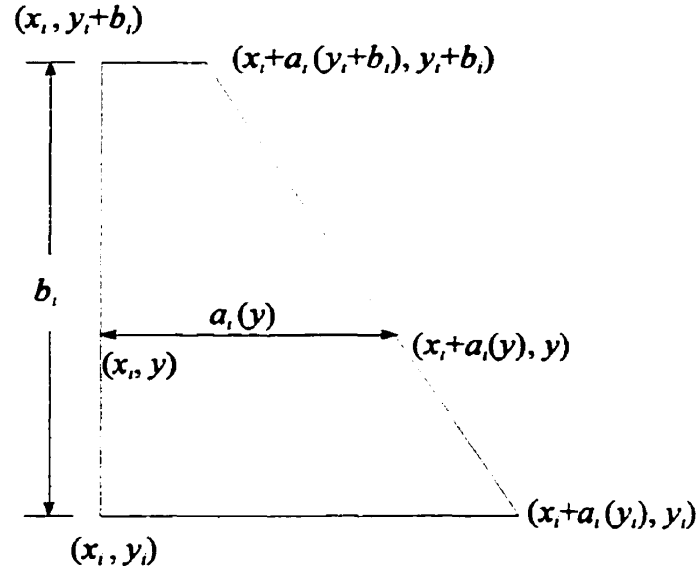

Figure 4.2(b): Shape of PVDF Strip Polarized in the y-direction

A strip aligned in the x-direction, for example strip 1 in Figure 4.1, is described by a shape function, $f(x)$, and is polarized to expand and contract in the x-direction. In our case, $f(x)$ represents the fraction of the maximum width of the strip at any location along the x-axis (refer to Figure 4.2(a)). The shape distribution function, $f(x)$, is hence mathematically defined as

$$f(x) = \frac{b_i(x)}{[b_i(x)]_{max}} \tag{4.2}$$

where $b_i(x)$ is the width of the PVDF strip at any location along the x-axis and $[b_i(x)]_{max}$ is the maximum width of the same strip. Now $b_i(x)$ from Figure 4.2(a) can be written as

$$b_i(x) = b_i(x_i)\left[1 - \left(\frac{x - x_i}{a_i}\right)\right] + b_i(x_i + a_i)\left[\frac{x - x_i}{a_i}\right] \tag{4.3}$$

where the constant a_i equals the length of the ith strip polarized in the x-direction, x_i is the x-coordinate of the bottom left corner of the strip, $b_i(x_i + a_i)$ is the minimum width of the PVDF strip, and $b_i(x_i)$ is the maximum width of the PVDF strip.

Substituting equation (4.3) into equation (4.2) and simplifying, we get

$$f(x) = 1 + \left[\frac{b_i(x_i + a_i) - b_i(x_i)}{a_i b_i(x_i)}\right][x - x_i] \tag{4.4}$$

Differentiating equation (4.4) with respect to x, we get

$$f'(x) = \frac{b_i(x_i + a_i) - b_i(x_i)}{a_i b_i(x_i)} \tag{4.5}$$

Similarly, a strip aligned in the y-direction, for example strip 2, is polarized to expand and contract in the y-direction. The shape distribution function, $g(y)$, for strips polarized in the y-direction is defined as

$$g(y) = \frac{a_i(y)}{[a_i(y)]_{max}} \tag{4.6}$$

where $a_i(y)$ is the width of the PVDF strip at any location along the y-axis and $[a_i(y)]_{max}$ is the maximum width of the same strip. Similar to the derivation of equation (4.4), we can obtain a modified expression for $g(y)$:

$$g(y) = 1 + \left[\frac{a_i(y_i + b_i) - a_i(y_i)}{b_i a_i(y_i)}\right][y - y_i] \tag{4.7}$$

Differentiating the result with respect to y, we get

$$g'(y) = \frac{a_i(y_i + b_i) - a_i(y_i)}{b_i a_i(y_i)} \tag{4.8}$$

4.2. Generalized Forces due to the Interaction between PVDF Strips and the Structure

Consider a composite element, that is, a plate element of width $b_p(x)$ covered with a piezoelectric strip of width $b_i(x)$ polarized in the x-direction. When a voltage is applied

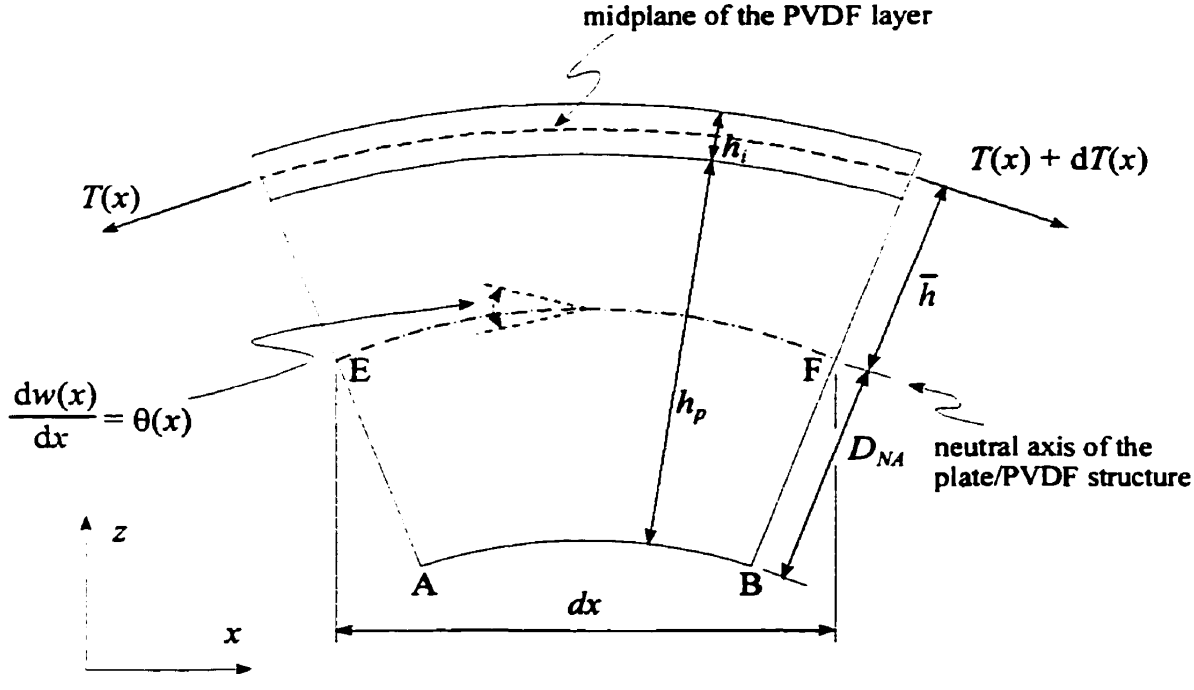

Figure 4.3: Cross-section of an Infinitesimal Plate Element of Area *dxdy*

across the thickness, h_i, of the ith PVDF strip, it introduces a strain, ε_s, in the PVDF strip. This strain is given by

$$\varepsilon_s = V_i(t)\frac{d_{31}}{h_i} \tag{4.9}$$

where $V_i(t)$ is the voltage applied across the thickness of the ith strip and d_{31} is a piezoelectric constant for the PVDF strip polarized in x-direction (see Table 5.1 for its value). ε_s in turn induces a longitudinal strain, ε_l, in the plate to insure a force equilibrium in the x-direction. To calculate the expression for ε_l, a force balance on the composite element is performed to obtain

$$E_p\varepsilon_l h_p b_p(x) + E_i(\varepsilon_s + \varepsilon_l)h_i b_i(x) = 0 \tag{4.10}$$

where the subscript 'p' refers to the plate and the subscript 'i' refers to the ith strip respectively. In the above equation, E is Young's Modulus of the material, b is the width, and h is the thickness. Writing equation (4.10) in terms of ε_l, we get

$$\varepsilon_l = -\frac{E_i h_i b_i(x)}{E_p h_p b_p(x) + E_i h_i b_i(x)}\varepsilon_s \tag{4.11}$$

Consider an elemental area, $dxdy$, of the composite element shown in Figure 4.3. When the force, i.e. the polarization, is in the x-direction, the tension per unit width is

$$T(x) \propto V_{ix}(t) \cdot f(x) \tag{4.12}$$

where $f(x)$ is given by equation (4.4) and $V_{ix}(t)$ is the voltage applied across the thickness of the ith strip polarized in the x-direction. Similarly, when the force is in the y-direction, the tension per unit width is

$$T(y) \propto V_{iy}(t) \cdot g(y) \tag{4.13}$$

where $g(y)$ is given by equation (4.7) and $V_{iy}(t)$ is the voltage applied across the thickness of the ith strip polarized in the y-direction.

The differential tension acting on the elemental area, $dxdy$, can be written as

$$dT(x) \propto V_{ix}(t) \cdot f'(x)dx \tag{4.14}$$

where $f'(x)$ is given by equation (4.5).

The tensions, $T(x)$ and $T(y)$ induce moments $M(x)$ and $M(y)$ respectively. The differential tension per unit width, $dT(x)$, acts through the moment arm $\bar{h}$, as shown in Figure 4.3, to create a net moment, dM_y, for width dy which can be written as,

$$dM_y = \bar{h} \cdot dT(x)dy$$

or,

$$dM_y \propto \bar{h} \cdot V_{ix}(t)\, f'(x)dxdy \tag{4.15}$$

Now the strains, ε_s and ε_l, are constant throughout the element. Thus, from Figure 4.3 and equations (4.10) and (4.15), the bending moment acting on the elemental area about +y-axis is further written as,

$$dM_y(x,t) = \frac{\partial}{\partial x}\Big[E_p h_p b_p(x)\varepsilon_l\Big(\frac{h_1}{2} - D_{NA}\Big) + E_i h_i b_i(x)(\varepsilon_s + \varepsilon_l)\Big(\frac{h_i}{2} + h_p - D_{NA}\Big)\Big]dxdy \tag{4.16}$$

where D_{NA} is the distance to the neutral axis of the composite plate (from AB to EF as shown in Figure 4.3).

In practice, $h_p b_p(x) \gg h_i b_i(x)$. Using this fact along with equation (4.11), we get,

$$\varepsilon_s + \varepsilon_l \approx \varepsilon_s \tag{4.17}$$

Using equations (4.2) and (4.9) and substituting equation (4.17) into equation (4.16), the expression for the bending moment about the y-axis in the elemental area becomes,

$$dM_y = \bar{c}_{x_i} V_{ix}(t) f'(x) dx dy \tag{4.18}$$

where

$$\bar{c}_{x_i} = E_i \left(\frac{h_p + h_i}{2} \right) d_{31} \tag{4.19}$$

where d_{31} is the piezoelectric constant for PVDF strips are polarized in the x-direction. $\bar{c}_{x_i}$ is referred to as the equivalent stiffness coefficient. It is a constant per unit width whose units are N/volt. This constant is based on the information taken from Bailey and Hubbard (1985) and from van Poppel and Misra (1992). It depends on the material properties and dimensions of the strip. This constant is similar to that given in Bailey and Hubbard (1985) for the beam because the small Poisson effect present for a plate has been neglected in this derivation. The difference is that here the constant is per unit width. In Bailey and Hubbard (1985), the width of the PVDF strip was assumed equal to the width of the beam and hence $\bar{c}_{x_i}$ was the same for all strips. Their units for the constant read Nm/volt.

Similarly, the bending moment about the x-axis is given by,

$$dM_x = -\bar{c}_{y_i} V_{iy}(t) g'(y) dx dy \tag{4.20}$$

where

$$\bar{c}_{y_i} = E_i \left(\frac{h_p + h_i}{2} \right) d_{32} \tag{4.21}$$

is again a constant per unit width and d_{32} is the piezoelectric constant for PVDF strips are polarized in the y-direction. The constant, $\bar{c}_{y_i}$, also has the units of N/volt.

The power acting on the elemental area covered by the strips is given as

$$dP = d(\overline{M} \cdot \overline{\omega}) \tag{4.22}$$

where

$$\overline{M} = M_x \overline{i} + M_y \overline{j} \tag{4.23}$$

and

$$\overline{\omega} = \dot{\theta}_x \overline{i} + \dot{\theta}_y \overline{j} \tag{4.24}$$

Hence, power on an elemental area of the wing covered by the strips can be expanded and written as

$$dP = \bar{c}_{x_i} V_{ix}(t) f'(x) \dot{\theta}_y dx dy - \bar{c}_{y_i} V_{iy}(t) g'(y) \dot{\theta}_x dx dy \tag{4.25}$$

where $\bar{c}_{x_i}$ is given by equation (4.19), $\bar{c}_{y_i}$ is given by equation (4.21), and

$$\dot{\theta}_x = \frac{\partial}{\partial t}\left(\frac{\partial w}{\partial y}\right) \quad \text{and} \quad \dot{\theta}_y = \frac{\partial}{\partial t}\left(-\frac{\partial w}{\partial x}\right) \tag{4.26}$$

Recall that the transverse displacement, w, can be expressed as

$$w(x, y, t) = \sum_{r=1}^{M} \sum_{s=1}^{N} \Phi_r(x) \Psi_s(y) q_{rs}(t) \tag{2.4}$$

Consider that the strips are unipolar. That is, at any given time a strip is polarized either in the x-direction or in the y-direction but not both. Let R_x be the total number of strips polar-

ized to expand and contract in the x-direction and R_y be the total number of strips polarized in the y-direction. Also, let

$$R_t = R_x + R_y$$

Hence, the total power acting on the total area covered by the strips, in non-dimensional form, can be written as

$$P = -\sum_{r=1}^{M}\sum_{s=1}^{N}\sum_{i=1}^{R_t}\left[\int_{\xi_i}^{\xi_i+\frac{a_i}{l}}\int_{\eta_i}^{\eta_i+\tilde{b}_i(\xi_i)} \bar{c}_{x_i} V_{ix}(t) f'(\xi)\frac{\partial(\Phi_r(\xi)\Psi_s(\eta))}{\partial\xi}\frac{c}{l}(1-\xi)\,d\xi\,d\eta + \int_{\eta_i}^{\eta_i+\frac{b_i}{c}}\int_{\xi_i}^{\xi_i+\tilde{a}_i(\eta_i)} \bar{c}_{y_i} V_{iy}(t) g'(\eta)\frac{\partial(\Phi_r(\xi)\Psi_s(\eta))}{\partial\eta}\frac{l}{c(1-\xi)}\,d\eta\,d\xi\right] \tag{4.27}$$

where

$$\tilde{b}_i(\xi_i) = \frac{b_i(x_i)}{c} \quad \text{and} \quad \tilde{a}_i(\eta_i) = \frac{a_i(y_i)}{l} \tag{4.28}$$

In these equations, l and c are the semi-span and the chord of the wing respectively, $b_i(x_i)$ and $a_i(y_i)$ are defined in Figures 4.2(a) and 4.2(b) respectively, $\Phi(\xi)$ and $\Psi(\eta)$ are the shape functions described in Chapter 2, and $V_{ix}(t)$ and $V_{iy}(t)$ are the voltages applied across the thickness of the ith strip aligned in the x-direction and y-direction respectively. Thus, the total power acting on the entire area of the wing by all the strips present is the summation of the power acting on the wing by the individual PVDF strips as seen in equation (4.27).

The total power can also be written as

$$P = \{1\}^T \{\tilde{P}\}$$

where $\{1\}$ is a $(R_t \times 1)$ unity vector and

$$\{\tilde{P}\} = [P_x]\{V_{ix}(t)\} + [P_y]\{V_{iy}(t)\} \tag{4.29}$$

The power components in equation (4.29) are defined as

$$\begin{aligned} P_{x_{irs}} &= \bar{c}_{x_i} \Omega_{irs} \\ P_{y_{irs}} &= \bar{c}_{y_i} \zeta_{irs} \end{aligned} \tag{4.30}$$

where

$$\Omega_{irs} = -\int_{\xi_i}^{\xi_i + \frac{a_i}{l}} \int_{\eta_i}^{\eta_i + \bar{b}_i(\xi_i)} f'(\xi) \frac{\partial(\Phi_r(\xi)\Psi_s(\eta))}{\partial \xi} \frac{c}{l}(1-\xi)\, d\xi\, d\eta \tag{4.31}$$

$$\zeta_{irs} = -\int_{\eta_i}^{\eta_i + \frac{b_i}{c}} \int_{\xi_i}^{\xi_i + \tilde{a}_i(\eta_i)} g'(\eta) \frac{\partial(\Phi_r(\xi)\Psi_s(\eta))}{\partial \eta} \frac{l}{c(1-\xi)} d\eta\, d\xi \tag{4.32}$$

Writing the matrices $[P_x]$ and $[P_y]$ in terms of their components, we obtain

$$[P_x] = \begin{bmatrix} \bar{c}_{x_1}\Omega_{111} & \bar{c}_{x_2}\Omega_{211} & \cdot & \cdot & \cdot & \bar{c}_{x_{R_t}}\Omega_{R_t 11} \\ \bar{c}_{x_1}\Omega_{112} & \bar{c}_{x_2}\Omega_{212} & \cdot & \cdot & \cdot & \cdot \\ \cdot & \cdot & \cdot & \cdot & \cdot & \cdot \\ \cdot & \cdot & \cdot & \cdot & \cdot & \cdot \\ \cdot & \cdot & \cdot & \cdot & \cdot & \cdot \\ \bar{c}_{x_1}\Omega_{1MN} & \bar{c}_{x_2}\Omega_{2MN} & \cdot & \cdot & \cdot & \bar{c}_{x_{R_t}}\Omega_{R_t MN} \end{bmatrix} \tag{4.33}$$

and

$$[P_y] = \begin{bmatrix} \bar{c}_{y_1}\zeta_{111} & \bar{c}_{y_2}\zeta_{211} & \cdot & \cdot & \cdot & \bar{c}_{y_{R_t}}\zeta_{R_t11} \\ \bar{c}_{y_1}\zeta_{112} & \bar{c}_{y_2}\zeta_{212} & \cdot & \cdot & \cdot & \cdot \\ \cdot & \cdot & \cdot & \cdot & \cdot & \cdot \\ \cdot & \cdot & \cdot & \cdot & \cdot & \cdot \\ \cdot & \cdot & \cdot & \cdot & \cdot & \cdot \\ \bar{c}_{y_1}\zeta_{1MN} & \bar{c}_{y_2}\zeta_{2MN} & \cdot & \cdot & \cdot & \bar{c}_{y_{R_t}}\zeta_{R_tMN} \end{bmatrix} \tag{4.34}$$

where MN is the total number of modes. The dimensions of the matrices on the right-hand-side of equation (4.29) are

$$\begin{aligned} dim[P_x] &= MN \text{ x } R_t \\ dim[P_y] &= MN \text{ x } R_t \\ dim\{V_{ix}(t)\} &= R_t \text{ x } 1 \\ dim\{V_{iy}(t)\} &= R_t \text{ x } 1 \end{aligned} \tag{4.35}$$

Substituting equation (4.29) into equation (4.1), we get

$$\{\dot{x}\} = [A]\{x\} + [B_x]\{V_{ix}(t)\} + [B_y]\{V_{iy}(t)\} \tag{4.36}$$

where the state vector $\{x\}$ and matrix $[A]$ have been previously defined in equations (2.29) and (2.30) respectively. The $[B_x]$ and $[B_y]$ matrices are written as

$$[B_x] = \begin{bmatrix} [0]_x \\ [P_x] \end{bmatrix} \tag{4.37}$$

$$[B_y] = \begin{bmatrix} [0]_y \\ [P_y] \end{bmatrix} \tag{4.38}$$

where $[0]_x$ is an (MN x R_t) null matrix and $[0]_y$ is an (MN x R_t) null matrix.

The generalized forces due to the interaction of the PVDF strips with the delta wing can now be written as

$$\{Q_{piezo}\} = [B_x]\{V_{ix}(t)\} + [B_y]\{V_{iy}(t)\} \tag{4.39}$$

Also, equation (4.36) can be further written as

$$\{\dot{x}\} = [A]\{x\} + \{Q_{piezo}\} \tag{4.40}$$

Now that the generalized forces, $\{Q_{piezo}\}$, due to the presence of the piezoelectric strips have been obtained, the transient response of the wing can be determined using equation (4.40) as will be shown in the next chapter. Furthermore, the dynamic response of the delta wing under unsteady, supersonic loading in the presence of these piezoelectric strips will be presented in the following chapter.

Chapter 5

Analysis of the Dynamics of the Wing under the Combined Piezoelectric and Aerodynamic Forces

This chapter is divided into two main sections. In the first section, a procedure to obtain the response of the delta wing, with and without aerodynamic loading, in the presence of PVDF actuators is discussed. To start with, we consider the wing under the influence of the piezoelectric strips alone. Following that the unsteady supersonic aerodynamic loading is introduced on the wing with piezoelectric strips present. The expressions for the generalized forces due to aerodynamic loading and the presence of piezoelectric strips are introduced into the general equation of motion for a dynamic system. These expressions are used to analyse the dynamic response of the system.

The second section presents and discusses the final results of the work presented in this thesis. This section is divided into three subsections. In the first subsection, the eigenvalues of a free-system are compared to existing results. The control effect of introducing piezoelectric strips at various locations on the delta wing, without aerodynamic loading, is studied in the second subsection. The dynamic responses of the wing, with and without unsteady supersonic aerodynamic loading, in the presence of piezoelectric strips are compared in the last subsection.

5.1 Dynamics of the System Under Piezoelectric and Aerodynamic Forces

The dynamics of the system under the combined piezoelectric and aerodynamic forces are analysed considering three locations on the delta wing shown in Figure 5.1.

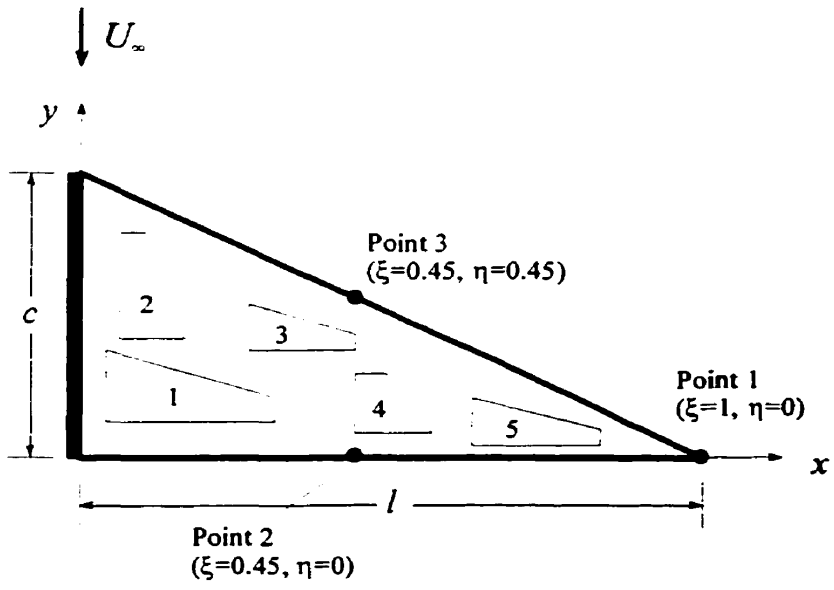

Figure 5.1: Locations of Points 1, 2 and 3 on the Delta Wing

The first location, Point 1, is placed at the tip, that is, $\xi = 1$ and $\eta = 0$; Point 2 is on the trailing edge of the wing at $\xi = 0.45$ and $\eta = 0$; and the third location, Point 3, is on the leading edge of the wing, placed at $\xi = 0.45$ and $\eta = 0.45$.

The plate is assumed to be made of aluminium alloy. The material properties of the plate as well as of the piezoelectric strips are listed in Table 5.1.

The response of the system under the influence of the piezoelectric strips, with and without aerodynamic loading, is now analysed.

Table 5.1: Physical Characteristics of the System

Physical Parameters	***Value***
Length of semi-span, l	2.0 m
Length of chord, c	1.0 m
Plate thickness, h_p	0.01 m
Density of Aluminium Alloy, ρ	2823.0 kg/m^3
Elastic modulus of the plate, E_p	70.0 x 10^9 Pa
Poisson's ratio, ν	0.334
PVDF film thickness, h_i	5.0 x 10^{-4} m
Elastic modulus of piezoelectric strips, E_i	60.0 x 10^9 Pa
Piezoelectric constant, d_{31}	250 x 10^{-12} m/volt

5.1.1 Transient Response of the Delta Wing

Piezoelectric strips, or PVDF strips, were introduced on the delta wing modelled as a cantilevered triangular plate in Chapter 4. The generalized forces, $\{Q_{piezo}\}$, produced due to the interaction of these PVDF strips with the delta wing are given by equation (4.39). The equation of motion for this PVDF-wing combination was written in a state-space form and is given by equation (4.40).

In this subsection, the PVDF strips are activated to damp out the oscillations of an unloaded delta wing. In other words, equation (4.40) is solved. The structural damping, namely *Rayleigh's damping*, C, given by equation (2.33) is also present. Once the generalized displacements and the generalized velocities for this forced system have been determined, the response of the plate at the point under consideration can be easily determined.

The equation for the generalized forces due to interaction of the PVDF strips with the plate is repeated below:

$$\{Q_{piezo}\} = [B_x]\{V_{ix}(t)\} + [B_y]\{V_{iy}(t)\} \tag{5.1}$$

where $V_{ix}(t)$ and $V_{iy}(t)$ are the voltages introduced across the thickness of the ith strip oriented in x- and y-directions respectively, and the matrices $[B_x]$ and $[B_y]$ are obtained by placing the five PVDF strips as shown in Figure 4.1 and using equations (4.37) and (4.38) respectively. The size, location, and orientation of each strip is given in Table 1 of Appendix *C*. As shown in Figure 4.1, strips 1, 3 and 5 are assumed to be oriented in the x-direction and strips 2 and 4 are assumed to be oriented in the y-direction. The matrices $[B_x]$ and $[B_y]$ can now be easily generated by writing a program in FORTRAN. The voltage is selected as the following

$$V_{i(x \text{ or } y)}(t) = -K_i \dot{w}_{tip} \tag{5.2}$$

where K_i is a constant and $\dot{w}_{tip}$ is the tip velocity.

Now that $\{Q_{piezo}\}$ has been determined, the state-space equation, equation (4.40), can be solved. As seen in equation (4.40), the equation for $\dot{x}$ is a first-order ordinary differential equation. This equation has to be integrated in order to determine both $\{q_{rs}\}$ and $\{\dot{q}_{rs}\}$. The Runge-Kutta method for integrating ordinary differential equations can be used for this purpose. A simple program is written in MATLAB to solve the state-space equations.

Having determined the generalized displacements and velocities, the transverse displacements, due to this tip velocity, at the three locations shown in Figure 5.1 can be determined for the following three conditions:

- Only x-aligned PVDF strips are active (only strips 1, 3 and 5 are active);
- Only y-aligned PVDF strips are active (only strips 2 and 4 are active); and
- All PVDF strips are active.

The results of this subsection are discussed in section 5.2.

5.1.2 Dynamic Response of the Delta Wing

In this subsection, the procedure to obtain the dynamic response of the wing under the combined forces of the unsteady supersonic aerodynamic loading and in the presence of the

piezoelectric strips will be discussed. The dynamic response of the delta wing is compared for the following two cases:

- Without aerodynamic loading, that is, $\{Q_{aero}\} = \{0\}$; and
- With aerodynamic loading, that is, $\{Q_{aero}\} \neq \{0\}$.

In both cases the piezoelectric strips are active, $\{Q_{piezo}\} \neq \{0\}$. When $\{Q_{aero}\} = \{0\}$, the only external force applied to the delta wing is the force generated by the PVDF strips. The forces generated by activating the PVDF strips are solely responsible for activating the wing oscillations. But when $\{Q_{aero}\} \neq \{0\}$, the piezoelectric and aerodynamic forces are simultaneously acting on the wing. The aim of this comparison is to determine whether or not the PVDF strips can counter the wing oscillations caused by the aerodynamic loading. Specifically, it has to be demonstrated that the forces due to the piezoelectric strips can effectively oppose the aerodynamic forces, thereby reducing the aeroelastic oscillations. The appropriate combination of PVDF strips and voltages applied across the individual strips has to be determined to obtain effective control of the wing oscillations when the unsteady supersonic aerodynamic loading is present. It should be noted that the magnitude of displacement of the wing has to be smaller when $\{Q_{aero}\} \neq \{0\}$ as compared to when $\{Q_{aero}\} = \{0\}$, in order to conclude that the PVDF strips are effective in controlling the aeroelastic oscillations of the delta wing. The appropriate combinations of active PVDF strips and the magnitudes of the voltages applied across these strips are determined by trial and error.

We start with the equation of motion for the dynamic system given by equation (2.36) which is repeated below:

$$[M]\{\ddot{q}_{rs}\} + [C]\{\dot{q}_{rs}\} + [K]\{q_{rs}\} = \{Q_{aero}\} + \{Q_{piezo}\} \tag{5.3}$$

where r and s identify the shape functions in the clamped-free and free-free directions respectively, $[M]$ is the mass matrix, $[C]$ is the structural damping matrix, $[K]$ is the stiffness matrix, $\{q_{rs}\}$ are the generalized displacements, $\{\dot{q}_{rs}\}$ are the generalized velocities, and $\{\ddot{q}_{rs}\}$ are the generalized accelerations. The equation for the complex generalized

displacements defined by equation (3.103) is repeated below:

$$\{\tilde{q}_{rs}\} = (\{q_{rs}^{c}\}\cos\omega t + \{q_{rs}^{s}\}\sin\omega t) + i\,(\{q_{rs}^{c}\}\sin\omega t - \{q_{rs}^{s}\}\cos\omega t) \tag{5.4}$$

where $\{q_{rs}^{c}\}$ and $\{q_{rs}^{s}\}$ are unique for each frequency and will be determined here. And, for convenience, $\{Q_{aero}\}$ is repeated below

$$\begin{aligned}\{Q_{aero}\} = {} & [Z_R(\omega)](\{q_{rs}^{c}\}\cos\omega t + \{q_{rs}^{s}\}\sin\omega t) \\ & - [Z_I(\omega)](\{q_{rs}^{c}\}\sin\omega t - \{q_{rs}^{s}\}\cos\omega t)\end{aligned} \tag{5.5}$$

where ω is the frequency of oscillation of the plate, while $[Z_R(\omega)]$ and $[Z_I(\omega)]$ are defined by equations (3.109) and (3.110), respectively.

In equation (5.1), let

$$\begin{aligned}V_{ix} &= \hat{V}_{ix}^{c}\cos\omega t + \hat{V}_{ix}^{s}\sin\omega t \\ V_{iy} &= \hat{V}_{iy}^{c}\cos\omega t + \hat{V}_{iy}^{s}\sin\omega t\end{aligned} \tag{5.6}$$

where $\hat{V}_{ix}^{c}$, $\hat{V}_{ix}^{s}$, $\hat{V}_{iy}^{c}$ and $\hat{V}_{iy}^{s}$ are the constant voltage amplitudes introduced across the thickness of the individual piezoelectric strips. Note that in equation (5.6), superscript '*c*' is used to denote that the voltage is a coefficient of $\cos\omega t$ and superscript '*s*' denotes that the voltage is a coefficient of $\sin\omega t$. Thus, in equation (5.6), $\hat{V}_{ix}^{c}$ and $\hat{V}_{iy}^{c}$ are called the *cosine* components and $\hat{V}_{ix}^{s}$ and $\hat{V}_{iy}^{s}$ are called the *sine* components.

As discussed in Chapter 3, the aerodynamic components of $\{Q_{aero}\}$, $[Z_R(\omega)]$ and $[Z_I(\omega)]$, are complicated functions of frequency, ω. Hence they cannot be broken down into simple coefficients of 1, ω and ω^2 as was done when solving for $\{Q_{piezo}\}$ in the previous section. In other words, the matrix $[A]$ for the state-space equation for the present case is extremely complicated. Thus, for this case, we will not be able to use the Runge-Kutta formulas for integrating ordinary differential equations. This is one of the limitations

of the present work. A feedback control law cannot be developed for the dynamic system under the combined forces of the piezoelectric and aerodynamic forces using the present model. The problem of complicated aerodynamic functions of frequency, namely $[Z_R(\omega)]$ and $[Z_I(\omega)]$, was encountered during the development process. Modifications to the aerodynamic analysis have to be made starting from first principles in order to develop an efficient feedback control law of the system, but such modifications are left to future investigations.

We can still, however, determine the transverse displacement of the delta wing by solving for the generalized displacements. These generalized displacements are assumed to be defined by equation (3.103). We are interested only in the real part of the generalized displacements which is given by

$$\{q_{rs}\} = Real\ \{\tilde{q}_{rs}\} = \{q_{rs}^c\}\cos\omega t + \{q_{rs}^s\}\sin\omega t \tag{5.7}$$

Hence, the generalized velocities become

$$\{\dot{q}_{rs}\} = \omega(-\{q_{rs}^c\}\sin\omega t + \{q_{rs}^s\}\cos\omega t) \tag{5.8}$$

and the generalized accelerations become

$$\{\ddot{q}_{rs}\} = -\omega^2(\{q_{rs}^c\}\cos\omega t + \{q_{rs}^s\}\sin\omega t) \tag{5.9}$$

Substituting equations (5.1), (5.5), (5.7), (5.8), and (5.9) in equation (5.3) and then combining coefficients of $\cos\omega t$ and $\sin\omega t$ from the left-hand-side and the right-hand-side of the resultant equation, one gets:

- coefficients of $\cos\omega t$:

$$-\omega^2[M]\{q_{rs}^c\} + \omega[C]\{q_{rs}^s\} + [K]\{q_{rs}^c\} - [Z_R(\omega)]\{q_{rs}^c\} - [Z_I(\omega)]\{q_{rs}^s\} = [P_x]\{\hat{V}_{ix}^c\} + [P_y]\{\hat{V}_{iy}^c\} \tag{5.10}$$

where $[P_x]$ and $[P_y]$ are defined by equations (4.33) and (4.34) respectively.

- coefficients of $\sin\omega t$:

$$-\omega^2[M]\{q_{rs}^s\} - \omega[C]\{q_{rs}^c\} + [K]\{q_{rs}^s\} - [Z_R(\omega)]\{q_{rs}^s\} + [Z_I(\omega)]\{q_{rs}^c\} = [P_x]\{\hat{V}_{ix}^s\} + [P_y]\{\hat{V}_{iy}^s\} \tag{5.11}$$

Now equations (5.10) and (5.11) are expressed in matrix form as

$$\begin{bmatrix} [A_{11}+B_{11}] & [A_{12}+B_{12}] \\ [A_{21}+B_{21}] & [A_{22}+B_{22}] \end{bmatrix} \begin{Bmatrix} q_{rs}^c \\ q_{rs}^s \end{Bmatrix} = \begin{bmatrix} [P_x] & [0] \\ [0] & [P_x] \end{bmatrix} \begin{Bmatrix} \hat{V}_{ix}^c \\ \hat{V}_{ix}^s \end{Bmatrix} + \begin{bmatrix} [P_y] & [0] \\ [0] & [P_y] \end{bmatrix} \begin{Bmatrix} \hat{V}_{iy}^c \\ \hat{V}_{iy}^s \end{Bmatrix} \tag{5.12}$$

where

$$\begin{aligned} A_{11} &= -\omega^2[M] + [K] \\ A_{12} &= \omega[C] \\ B_{11} &= -[Z_R(\omega)] \\ B_{12} &= -[Z_I(\omega)] \end{aligned} \tag{5.13}$$

$$\begin{aligned} A_{21} &= -\omega[C] \\ A_{22} &= -\omega^2[M] + [K] \\ B_{21} &= [Z_I(\omega)] \\ B_{22} &= -[Z_R(\omega)] \end{aligned} \tag{5.14}$$

Equation (5.12) can be written more compactly as

$$\begin{Bmatrix} q_{rs}^c \\ q_{rs}^s \end{Bmatrix} = [AB]^{-1}\{Q_{volt}\} \tag{5.15}$$

where

$$[AB] = \begin{bmatrix} [A_{11} + B_{11}] & [A_{12} + B_{12}] \\ [A_{21} + B_{21}] & [A_{22} + B_{22}] \end{bmatrix} \tag{5.16}$$

and

$$\{Q_{volt}\} = \begin{bmatrix} [P_x] & [0] \\ [0] & [P_x] \end{bmatrix} \begin{Bmatrix} \hat{V}_{ix}^c \\ \hat{V}_{ix}^s \end{Bmatrix} + \begin{bmatrix} [P_y] & [0] \\ [0] & [P_y] \end{bmatrix} \begin{Bmatrix} \hat{V}_{iy}^c \\ \hat{V}_{iy}^s \end{Bmatrix} \tag{5.17}$$

When $\{Q_{aero}\}$ is zero, equations (5.15) and (5.17) still hold, however equation (5.16) becomes

$$[AB] = \begin{bmatrix} [A_{11}] & [A_{12}] \\ [A_{21}] & [A_{22}] \end{bmatrix} \tag{5.18}$$

A program written in MATLAB is used to solve for $\{q_{rs}^c\}$ and $\{q_{rs}^s\}$. The results are substituted back into equation (5.7) to determine the generalized displacements, $\{q_{rs}\}$. Once the generalized displacements have been determined, these are in turn substituted into the equation for the non-dimensional transverse displacement, equation (2.5). The transverse displacements, w, are determined at the various locations shown in Figure 5.1.

The magnitude of the voltage applied across the thickness of the piezoelectric strips is varied to achieve maximum control of the aeroelastic oscillations. The results are discussed in section 5.2.4.

5.2 Results

This section presents the final results of the work presented in the thesis. The calculated eigenvalues of the free-system are compared to those obtained by an existing method in the first subsection, and the response of the free-system is discussed subsequently. Then, struc-

tural damping is introduced and the response of the delta wing again determined. Next the piezoelectric strips are introduced and the transient response of the delta wing is obtained and compared to the response when only structural damping is present. Finally, the response of the dynamic system when both the piezoelectric strips and aerodynamic loading are present is discussed.

5.2.1 Eigenvalues of the Free-System

The delta wing was modelled as a triangular cantilevered plate in Chapter 2. The eigenvalue problem for the free vibrating cantilevered triangular plate was formulated in section 2.3 of Chapter 2 and is given by equation (2.26). The mass and stiffness matrices were also derived in Chapter 2. In this section, the natural frequencies of the plate are compared to those given by Andersen (1954) for various modes of vibration to validate the structural model developed here. Andersen obtains the natural frequencies of a triangular plate using the *Ritz Approximation method.*

As a first step towards determining the eigenvalues of the free-system, the mass and stiffness matrices are generated by a program written in FORTRAN. For example, consider the matrices generated for two shape functions in the clamped-free direction, ($M = 2$); and three shape functions in the free-free direction, ($N = 3$). Hence, $MN = 6$. These matrices are imported into a simple program written in MATLAB to solve the eigenvalue problem.

Andersen (1954) non-dimensionalized the frequencies so that they would be independent of the size of the chosen plate but dependent on its shape. To compare the results obtained in the present study to those obtained by Andersen, we too non-dimensionalize the natural frequencies obtained here. Table 5.2 compares the non-dimensional natural frequencies for the free-system obtained by the *Present Method* to those obtained by Andersen (1954) for an unsymmetric cantilevered triangular plate. The results for ω_i, $i > 3$, are not available in Andersen (1954) for the unsymmetric plate. Hence only the first two natural frequencies are compared to the *Present Method* for $\frac{l}{c}$ of 2, 4 and 7.

Table 5.2(a): Comparison of Frequencies of the Free-System: Unsymmetric Plates

Mode	$\omega_n l^2\sqrt{\frac{\rho h_p}{D}}$ for $\frac{l}{c}=2$		$\omega_n l^2\sqrt{\frac{\rho h_p}{D}}$ for $\frac{l}{c}=4$		$\omega_n l^2\sqrt{\frac{\rho h_p}{D}}$ for $\frac{l}{c}=7$	
	Present Method $M=3, N=2$	Andersen	*Present Method* $M=3, N=2$	Andersen	*Present Method* $M=3, N=2$	Andersen
1	7.16	5.88	7.16	6.61	7.16	6.90
2	31.32	25.40	31.90	28.80	31.26	30.28
3	72.83	NA	103.63	NA	102.18	NA
4	111.71	NA	105.45	NA	155.38	NA
5	175.96	NA	311.09	NA	521.54	NA
6	302.51	NA	554.60	NA	906.26	NA

Table 5.2(b): Comparison of Frequencies for various values of *MN*: *Present Method*

Mode	$MN=4$ $M=2, N=2$	$MN=6$ $M=2, N=3$	$MN=6$ $M=3, N=2$	$MN=9$ $M=3, N=3$
1	7.16	7.16	7.16	7.16
2	37.04	37.04	31.32	31.82
3	87.84	78.73	72.83	47.37
4	185.80	206.77	111.71	109.90
5	--	239.90	175.96	166.03
6	--	564.98	302.51	318.71
7	--	--	--	441.96
8	--	--	--	849.00
9	--	--	--	1093.41

In Table 5.2(a), ω_n is the calculated natural frequency of the wing, l is the semi-span of the wing, D is flexular rigidity given by equation (2.3), ρ is the density of the plate material (in this case Aluminium Alloy), and h_p is the plate thickness. The values of the physical characteristics are listed in Table 5.1.

As seen from Tables 5.2(a) and 5.2(b), the frequencies (for $MN = 6$) are slightly different

when $M = 2$, $N = 3$ from when $M = 3$, $N = 2$ because there is one more clamped-free mode and there are no free modes active in the free-free direction in the latter case. As seen from Tables 5.2(a) and 5.2(b), the frequencies obtained using the *Present Method* have converged for the first two modes when $MN = 4$ and $MN = 6$.

As seen in Table 5.2(a), for larger $\frac{l}{c}$ ratios the values of the natural frequencies from the two methods are in good agreement. However, for smaller $\frac{l}{c}$ ratios the differences in the values of the natural frequencies are somewhat larger; this may be due to the deflection shapes chosen by Andersen (1954) for the *Ritz* method which may not give accurate results for small $\frac{l}{c}$. Barton (1951) made similar observations about his own implementation of the *Ritz* method.

Andersen's analysis is more reliable for symmetric plate cases. When the frequencies for the first two modes generated by the *Present Method* were compared to the first two modes for symmetric plate frequencies of Andersen (1954), it was found that the results were in very good agreement. The comparison is shown in Table 5.3.

Table 5.3: Comparison of Frequencies of the *Present Method* to Symmetric Plates

Mode	$\omega_n l^2 \sqrt{\frac{\rho h_p}{D}}$ for $\frac{l}{c} = 2$		$\omega_n l^2 \sqrt{\frac{\rho h_p}{D}}$ for $\frac{l}{c} = 8$		$\omega_n l^2 \sqrt{\frac{\rho h_p}{D}}$ for $\frac{l}{c} = 14$	
	Present Method	Andersen Symmetric	*Present Method*	Andersen Symmetric	*Present Method*	Andersen Symmetric
1	7.16	7.149	7.16	7.08	7.16	7.08
2	31.32	30.80	31.28	30.65	31.24	30.64

Thus, the structural dynamics model developed in this thesis can be used further with confidence. Now that the eigenvalues of a free-system have been determined, the response of this system can be obtained in the next subsection.

5.2.2 Response of the Undamped, Unforced Delta Wing

In this subsection, the structural damping, C, is assumed to be zero and the PVDF strips are deactivated. Hence, in this case, the state-space equation (2.28) representing the free-system holds well.

As a first step, the Runge-Kutta method is used to solve equation (2.28) in order to determine the generalized displacements, $\{q_{rs}\}$, and the generalized velocities, $\{\dot{q}_{rs}\}$, of the undamped, unforced cantilevered triangular plate.

Let us consider two modes of vibration each in the clamped-free and free-free directions. Hence $MN = 4$. Initial conditions for $\{q_{rs}\}$ and $\{\dot{q}_{rs}\}$ for all four modes of vibration are given as an input to excite the system. These initial conditions are listed in Table 5.4.

Table 5.4: Initial Inputs to the System

$\{q_{rs}(0)\}$	0.01	0.003	0.003	0.001
$\{\dot{q}_{rs}(0)\}$	0	0	0	0

In reality, the system will damp out eventually because of inherent material damping properties. However, in this subsection, it is assumed that there is no material damping present and matrix $[A]$ is given by equation (2.30). Thus, the oscillations of the plate will never damp out.

Once the generalized displacements, $\{q_{rs}\}$, have been determined for the system they are placed in the equation for transverse displacement for the plate, equation (2.5). The shape functions, $\Phi_r(\xi)$ and $\Psi_s(\eta)$, are given by equations (2.7) and (2.8) respectively. To determine the transverse displacement at any location, replace ξ and η by appropriate values for that location shown in Figure 5.1. All the components of equation (2.5) are now known and the transverse displacement can be determined easily.

The results of the undamped, unforced case for the three positions are shown in Figures 5.2(a), 5.3(a) and 5.4(a) respectively. Note that the scale is different for Point 1 as compared to Points 2 and 3 in all figures. As seen from the figures, the wing oscillations do not decay in the absence of damping, as expected. Also, the wing oscillations are largest at the wing tip as expected for a cantilever plate.

5.2.3 Structural Damping Alone Acting on the Delta Wing

In the previous subsection, the transverse displacement of an undamped free vibrating plate was determined. In this subsection, the structural damping given by equation (2.33) is introduced into the system. The corresponding matrix $[A]$ from equation (2.34) involving structural damping is used for solving the state-space equation, equation (2.28). In equation (2.33), let the damping material constants for the plate be $\alpha = 0$ and $\beta = 0.001$. All steps to determine the response of the plate are as described in section 5.2.2 using the initial conditions listed in Table 5.4.

The results from introducing the structural damping are shown for the three points in Figures 5.2(b), 5.3(b) and 5.4(b) respectively. As seen in the figures, the wing oscillations indeed damp out over time.

5.2.4 Results for the Transient Response of the Delta Wing under the Effect of Piezoelectric Forces

In the previous subsection, an acceptable response was obtained for an inherently damped system. The PVDF strips are now activated to obtain the transient response of the delta wing. Also, it is assumed that the system has an inherent damping.

In the first case, only the strips oriented in the x-direction, that is strips 1, 3 and 5, are activated. For this let $K_{i=1} = 1000$; $K_{i=3} = 700$; and $K_{i=5} = 800$. The results for all three positions are shown in Figures 5.2(c), 5.3(c) and 5.4(c) respectively.

As seen in the figures, activating the strips oriented in the x-direction has a significant effect on the damping out of the oscillations. The system damps out faster when the PVDF strips aligned in the x-direction are active as compared to the case when only structural damping is present, as seen in Figures 5.2(b), 5.3(b) and 5.4(b). Also, as seen in Figures 5.2(f), 5.3(f) and 5.4(f), the magnitude of damping due to the strip nearest the root, that is strip 1, is larger than that when structural damping alone is present. In other words, even one strip at the root (and aligned in the x-direction) has a significant contribution in damping out of the delta wing oscillations.

Next only the strips oriented in the y-direction, that is strips 2 and 4, are activated. For this let $K_{i=2} = 1000$; and $K_{i=4} = 700$. The results for all three positions are shown in Figures 5.2(d), 5.3(d) and 5.4(d). Comparing with Figures 5.2(b), 5.3(b) and 5.4(b) one notes that activating the strips oriented in the y-direction does not have a significant effect on the damping out of the oscillations. The magnitude of the wing oscillations are comparable to that of the case when only structural damping is present. Hence it can be said that the PVDF strips aligned in the y-direction have little or no effect on reducing the oscillations over time.

Finally, the strips aligned in both x- and y-directions are activated simultaneously. The values of K_i are the same as those used above. The results are shown in Figures 5.2(e), 5.3(e) and 5.4(e) for the three positions. As seen, the results are comparable to the case of activating the strips aligned in the x-direction only. Hence, it can be safely said that activating the x-direction strips alone has the most contribution in damping out the oscillations of the wing.

Thus by introducing the piezoelectric strips on the wing one can damp out the oscillations faster than by just having the structural damping present.

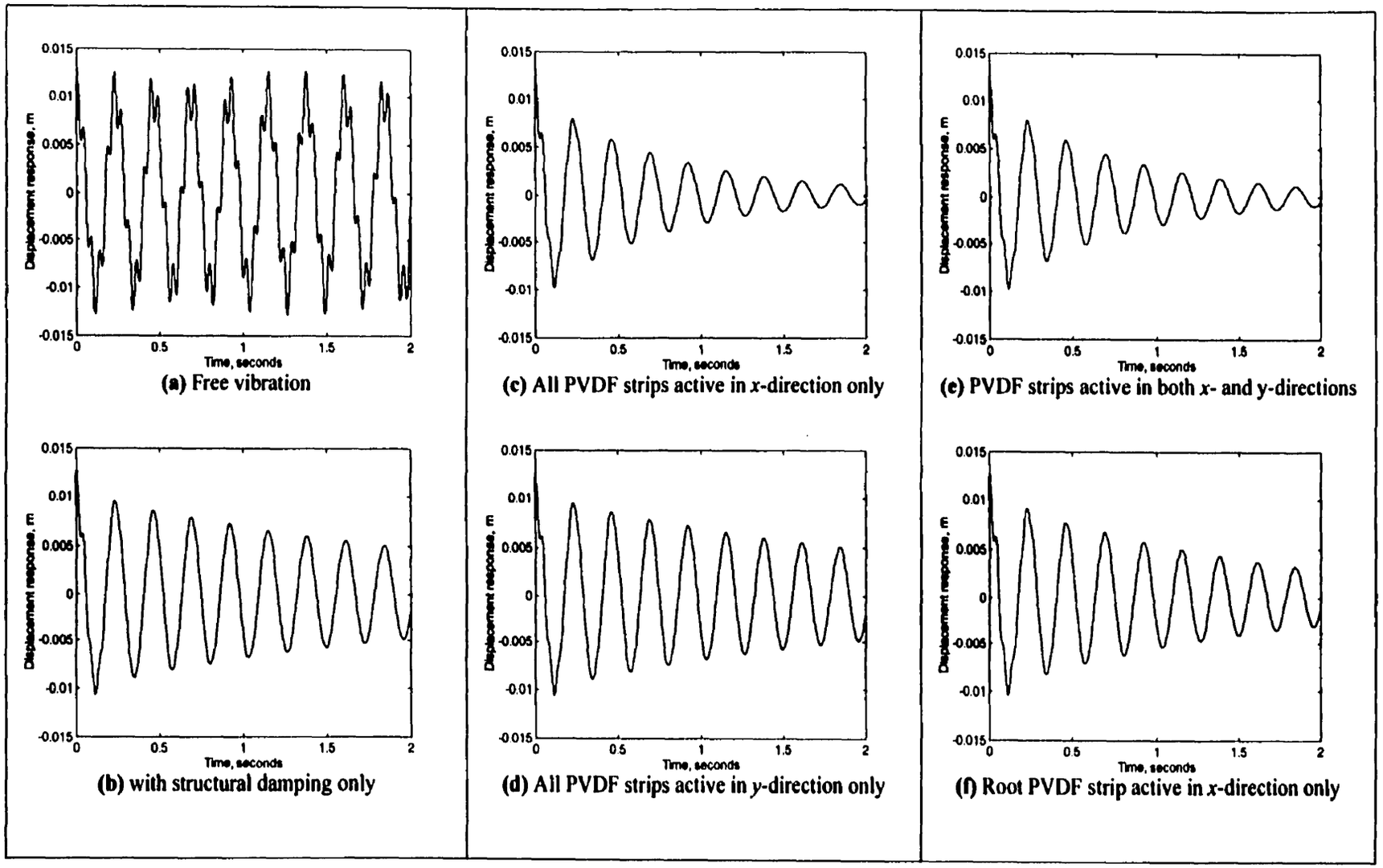

Figure 5.2: Transient Response of the Delta Wing at $\xi = 1.0$ and $\eta = 0$ ($M = 2$ and $N = 2$)

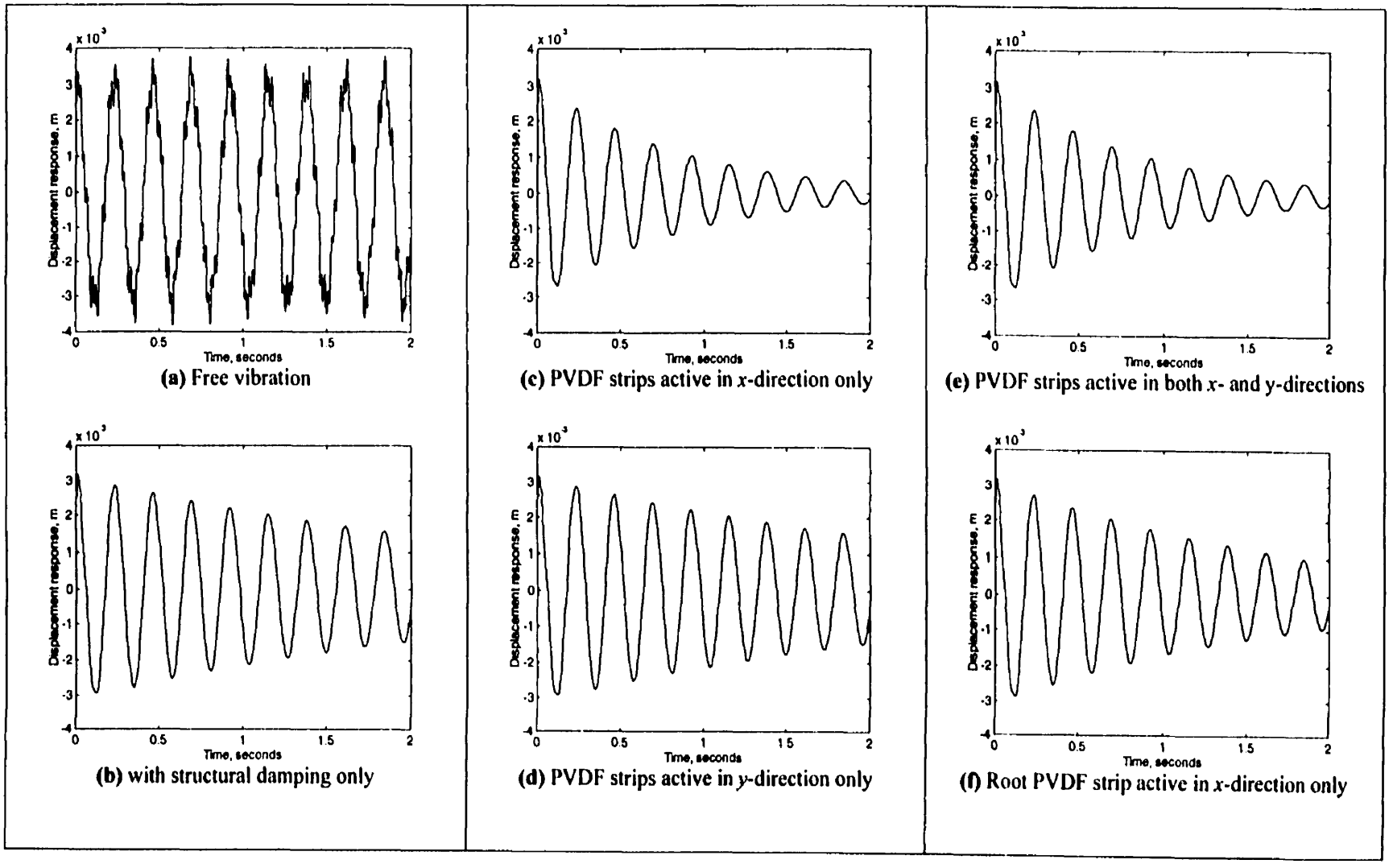

Figure 5.3: Transient Response of the Delta Wing at $\xi = 0.45$ and $\eta = 0$ ($M = 2$ and $N = 2$)

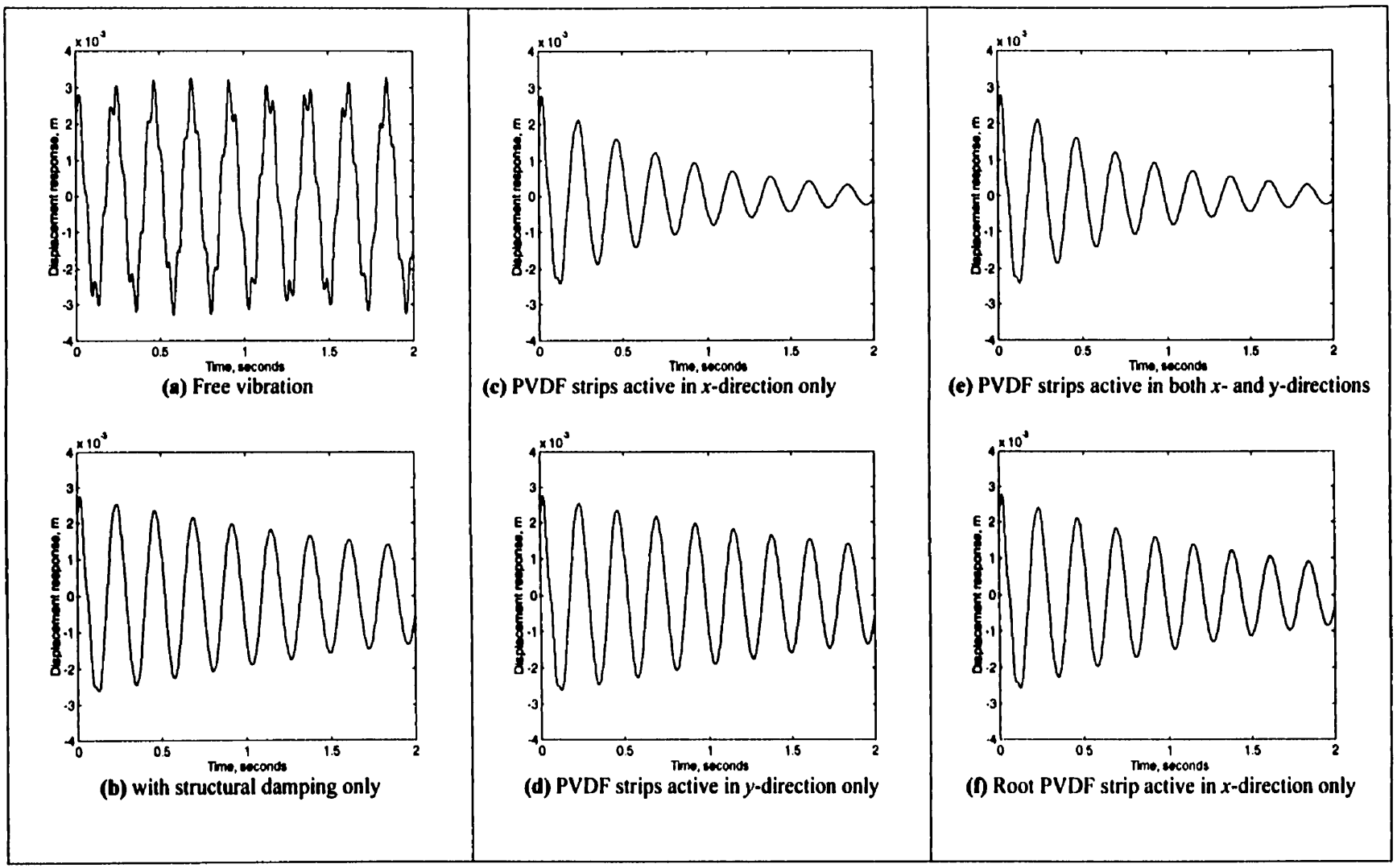

Figure 5.4: Transient Response of the Delta Wing at $\xi = 0.45$ and $\eta = 0.45$ ($M = 2$ and $N = 2$)

5.2.5 Results for the Dynamic Response of the Delta Wing under the Combined Effect of the Piezoelectric and Unsteady Aerodynamic Forces

In the preceding subsection, the response of the delta wing in the presence of PVDF strips alone was studied. It was concluded that the application of appropriate voltages to the PVDF strips effectively damps out the wing oscillations. The unsteady supersonic aerodynamic loading is now introduced on this structural-piezoelectric model to study the effects of the PVDF strips when the aerodynamic loading is present.

To obtain the response of this dynamic system, equation (5.15) is solved as discussed in section 5.1 for the three locations shown in Figure 5.1 using a periodic frequency, ω = 70 rads/sec. As a reminder, equation (5.16) is used in equation (5.15) when $\{Q_{aero}\} \neq \{0\}$ and equation (5.18) is used when $\{Q_{aero}\} = 0$. Two admissible functions considered in both the clamped-free and free-free directions. Thus, $MN = 4$ again. The values of the components of the generalized displacements, $\{q^c_{rs}\}$ and $\{q^s_{rs}\}$, are substituted back into the equation for the transverse displacement, w, as discussed in section 5.1. Hence the dynamic response is obtained for all locations shown in Figure 5.1.

A large number of numerical simulations were carried out to determine the best combinations of voltages applied across the various PVDF strips for effective reduction of the aeroelastic oscillations. However, only a handful of results are presented herein for brevity.

We will start by activating the PVDF strips one-by-one. To find the best combination of strips, the amplitudes of the oscillatory voltages introduced across the thickness of the individual piezoelectric strips, $\hat{V}^c_{ix}$, $\hat{V}^s_{ix}$, $\hat{V}^c_{iy}$ and $\hat{V}^s_{iy}$ in equation (5.6), are varied. In some cases the signs of $\hat{V}^c_{ix}$, etc. are also changed to determine whether or not the strips provide more control. As a reminder, the PVDF strips are deemed useful only if the wing oscillations are smaller in magnitude when $\{Q_{aero}\} \neq \{0\}$ as compared to when $\{Q_{aero}\} = \{0\}$ in equation (5.15) (implying that the aerodynamic and piezoelectric effects are opposing each other).

Cases Analysed

The following is a brief description of five of the cases considered in studying the dynamic response of the system:

Case 1: The root strip aligned in the *x*-direction, strip 1, is activated alone.

Case 2: Strips 1 and 3 are activated while the *y*-direction strips are deactivated, that is $\hat{V}_{iy}^{c}$ and $\hat{V}_{iy}^{s}$ are zero for all strips aligned in the *y*-direction. Also, $\hat{V}_{ix}^{s}$ is varied. In this case, the combinations listed in Table 5.5 are compared.

Case 3: The third strip aligned in the *x*-direction, strip 5, is activated. This strip is introduced into the best PVDF combination obtained from Case 2. The applied voltages are listed in Table 5.6.

Case 4: The *y*-direction strips are activated and are placed in the best PVDF combination obtained so far. The voltages, $\hat{V}_{iy}^{c}$ and $\hat{V}_{iy}^{s}$, across strips 2 and 4 are varied.

Case 5: A different periodic frequency, $\omega = 150$ rads/sec, is chosen to study the effects of varying the frequency on the combinations of piezoelectric strips required to reduce the aeroelastic oscillations. The aerodynamic matrices represented by $[Z_R(\omega)]$ and $[Z_I(\omega)]$ are recalculated for this frequency.

Results obtained for Cases 1 and 2

Case 1: The magnitude of the oscillations is larger at all three locations when $\{Q_{aero}\}$ is zero, that is, aeroelastic and piezoelectric loading do not oppose each other. The same behaviour is seen when $\hat{V}_{ix}^{c}$ was increased or decreased. As this is not acceptable behaviour, more strips have to activated.

Case 2: Please refer to Figures 5.5 to 5.11 for the results of the test conditions listed in Table 5.5. Figures 5.5, 5.6 and 5.7 show the response of the wing for case 2(i) at locations 1, 2 and 3 respectively. As seen from the results, the combination is effective only for Point 1, that is the magnitude of oscillation is smaller when aerodynamic loading is present as compared to when it is not. But this is not true for Points 2 and 3.

Figures 5.8, 5.9 and 5.10 represent case 2(ii) for the three locations on the wing. As seen from the figures, the magnitude of wing oscillation is smaller when $\{Q_{aero}\} \neq \{0\}$ as

Table 5.5: Amplitude of Voltage Applied across each PVDF Strip: Case 2

Case no.	Figure no.	Strip				
		1	2	3	4	5
2(i)	5.5 - 5.7: (a)	$\hat{V}_{ix}^{c}$ = -500	--	$\hat{V}_{ix}^{c}$ = -400, $\hat{V}_{ix}^{s}$ = +200	--	--
	5.5 - 5.7: (b)	$\hat{V}_{ix}^{c}$ = -500	--	$\hat{V}_{ix}^{c}$ = -400, $\hat{V}_{ix}^{s}$ = 0	--	--
	5.5 - 5.7: (c)	$\hat{V}_{ix}^{c}$ = -500	--	$\hat{V}_{ix}^{c}$ = -400, $\hat{V}_{ix}^{s}$ = -200	--	--
2(ii)	5.8 - 5.10: (a)	$\hat{V}_{ix}^{c}$ = -500	--	$\hat{V}_{ix}^{c}$ = -600, $\hat{V}_{ix}^{s}$ = +200	--	--
	5.8 - 5.10: (b)	$\hat{V}_{ix}^{c}$ = -500	--	$\hat{V}_{ix}^{c}$ = -600, $\hat{V}_{ix}^{s}$ = 0	--	--
	5.8 - 5.10: (c)	$\hat{V}_{ix}^{c}$ = -500	--	$\hat{V}_{ix}^{c}$ = -600, $\hat{V}_{ix}^{s}$ = -200	--	--
2(iii)	5.11: (a)-(c)	$\hat{V}_{ix}^{c}$ = -500, $\hat{V}_{ix}^{c}$ = -200	--	$\hat{V}_{ix}^{c}$ = -400	--	--

***Note**: Voltage components not mentioned above are set to zero.*

compared to when $\{Q_{aero}\} = \{0\}$ provided that $\hat{V}_{ix}^{s}$ is zero for all strips. Thus, the piezoelectric strips are beneficial under these conditions. Though the magnitude of oscillation when $\{Q_{aero}\} \neq \{0\}$ at Point 1 is slightly larger for case 2(ii) as compared to case 2(i), it is smaller for Points 2 and 3. Hence, overall case 2(ii) represents a better combination.

Figure 5.11 represents case 2(iii) and shows the response of the plate at Points 1, 2 and 3 when $\hat{V}_{ix}^{s}$ of strip 1 is non-zero. Here again the results for Points 2 and 3 are not good whereas for Point 1 the results are satisfactory.

Thus, we can say that only the *cosine* component of the voltage, $\hat{V}_{ix}^{c}$, is effective in controlling the wing oscillations when only two x-direction strips are active.

The best results obtained for cases 2(i) and 2(ii), that is when $\hat{V}_{ix}^{s} = 0$ for all strips, are compiled and shown in Figures 5.12 and 5.13 respectively. From these figures, we conclude that the magnitude of the voltage applied across strip 3 has to be greater than that applied to strip 1 when only two strips are active and the periodic frequency is 70 rads/sec. Hence the results from case 2(ii), presented in Figure 5.13, are the best.

Results obtained for Case 3

Strip 5 is introduced into both case 2(i) and case 2(ii). The results for all three locations are shown in Figures 5.14 and 5.15.

Table 5.6: Amplitude of Voltage Applied across each PVDF Strip: Case 3

Case no.	Figure no.	Strip				
		1	2	3	4	5
3(i)	5.14: (a)-(c)	$\hat{V}_{ix}^{c}$ = -500	--	$\hat{V}_{ix}^{c}$ = -400	--	$\hat{V}_{ix}^{c}$ = -300
3(ii)	5.15: (a)-(c)	$\hat{V}_{ix}^{c}$ = -500	--	$\hat{V}_{ix}^{c}$ = -600	--	$\hat{V}_{ix}^{c}$ = -300

***Note**: Voltage components not mentioned above are set to zero.*

As shown in Figure 5.14, when strip 5 is activated, the wing oscillations with aerodynamic loading present are smaller than when the loading is absent. In other words, our goal is achieved. Hence, to make the PVDF strip combination of case 2(i) work, strip 5 has to be activated. When Figure 5.12 is compared to Figure 5.14, we see that the magnitudes of the oscillations for $\{Q_{aero}\} \neq \{0\}$ are comparable. When strip 5 is activated in addition to the voltages applied in case 2(ii), we see from Figure 5.15 that the results are worse as compared to cases 2(ii) and 3(i). Therefore, for future test cases the PVDF strip combinations of either case 2(ii) or case 3(i) can be used as both give good results.

Results obtained for Case 4

The PVDF strips aligned in the y-direction are placed in one of the two best combinations obtained so far, namely, case 2(ii). By varying the voltages across strips 2 and 4, it was seen that either there was little or no effect in certain cases, while in some other cases the wing oscillations were increased. In other words, by introducing the strips aligned in the y-direction the response either changed very little or worsened. One set of results representing active y-direction PVDF strips is shown in Figure 5.16, for the voltage combinations given in Table 5.7.

Figure 5.16(a) refers to Point 1 on the wing. It is seen that the magnitude of oscillations

Table 5.7: Amplitude of Voltage Applied across each PVDF Strip: Case 4

Case no.	Figure no.	Strip				
		1	2	3	4	5
4(i)	5.16: (a)-(c)	$\hat{V}_{ix}^{c}$ = -500	$\hat{V}_{iy}^{c}$ = +100	$\hat{V}_{ix}^{c}$ = -600	--	--

***Note**: Voltage components not mentioned above are set to zero.*

when both aerodynamic and piezoelectric loading are present is the least for this combination. However, the combination is not suitable for Points 2 and 3 as seen in Figures 5.16(b) and 5.16(c) respectively. Please note that in the previous subsection it was found that the strips aligned in the *y*-direction have little or no effect as well.

As seen from the results obtained so far, locations 2 and 3 do not have a good response for most of the combinations of voltages that have been tried. The only way to ascertain the appropriate frequency magnitude for which all locations on the delta wing will respond well is by trial and error. This is one of the limitations of the present study. More work is required to find an efficient way to determine the appropriate periodic frequency. Due to the limitations of the scope of this thesis, this problem will not be dealt with here. However to demonstrate that a change in the magnitude of the chosen periodic frequency changes the response of the system, the following final test case is presented.

Results obtained for Case 5

Let the voltage magnitudes applied across the thickness of the PVDF strips be the same as those given in case 2(i). The results are shown in Figure 5.17. As seen from the figure, the magnitude of aeroelastic oscillation is smaller when $\{Q_{aero}\} = \{0\}$ as compared to when $\{Q_{aero}\} \neq \{0\}$ for all three locations, which is what we are aiming for. Comparing the results shown in Figure 5.17 to those in Figures 5.12, we see that the results for 150 rads/sec are quite good as opposed to those when the frequency is 70 rads/sec. Hence, it has been demonstrated that changing the periodic frequency can significantly affect the performance of the piezoelectric strips.

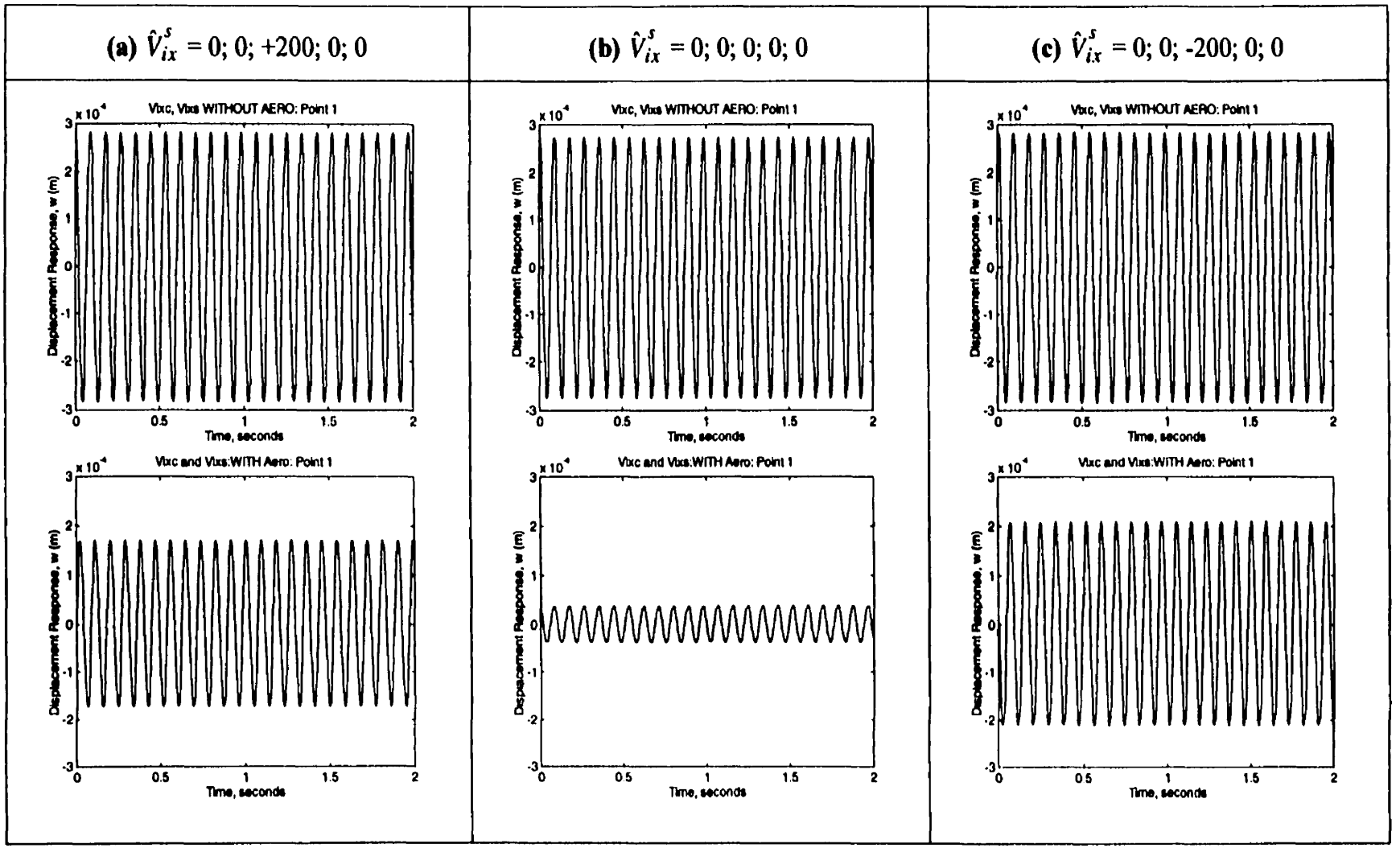

Figure 5.5: Dynamic Response at Point 1: $\hat{V}_{ix}^{c}$ = -500; 0; -400; 0; 0; $\hat{V}_{iy}^{c}$ = 0; 0; 0; 0; 0; $\hat{V}_{iy}^{s}$ = 0; 0; 0; 0; 0

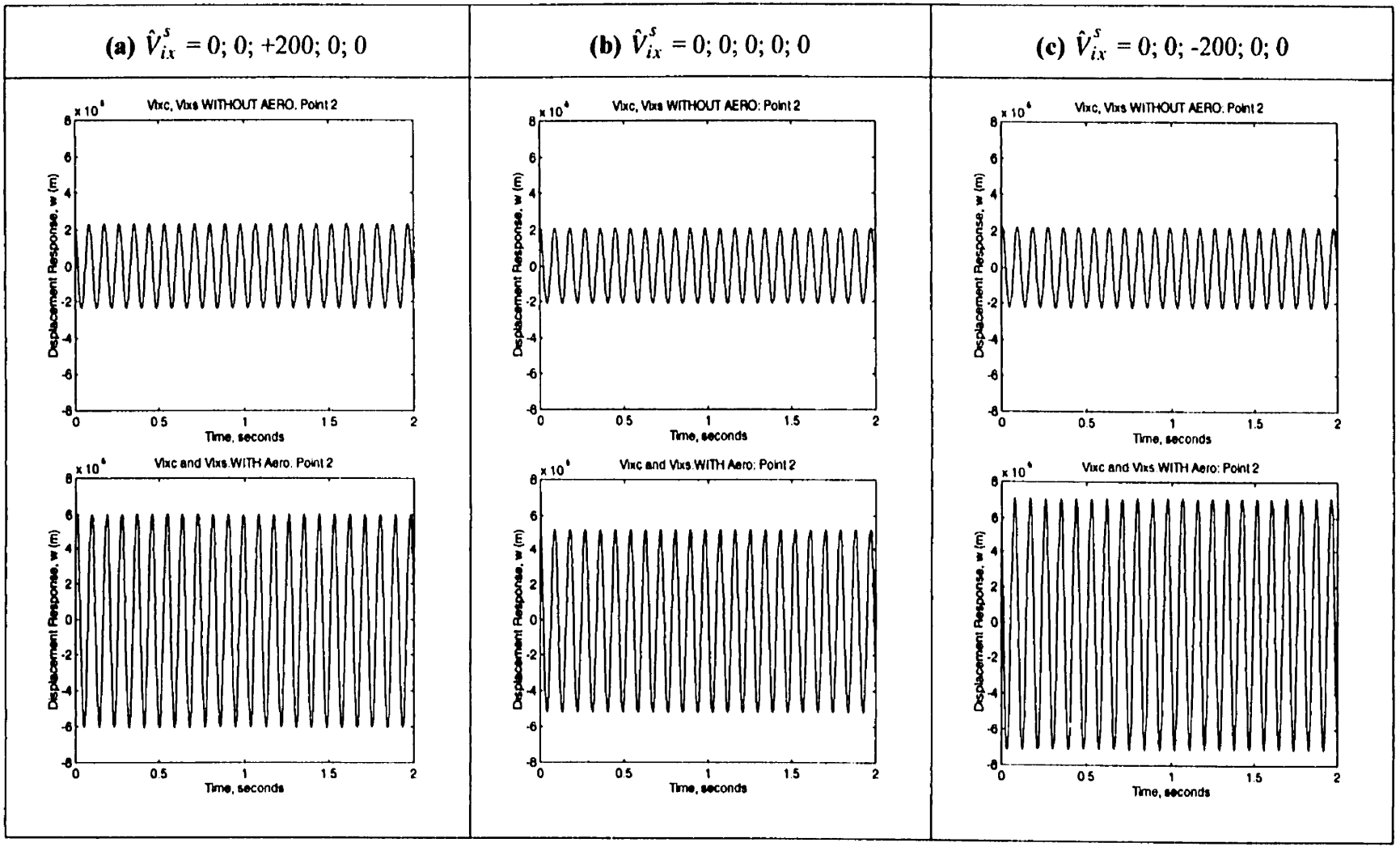

Figure 5.6: Dynamic Response at Point 2: $\hat{V}_{ix}^{c}$ = -500; 0; -400; 0; 0; $\hat{V}_{iy}^{c}$ = 0; 0; 0; 0; 0; $\hat{V}_{iy}^{s}$ = 0; 0; 0; 0; 0

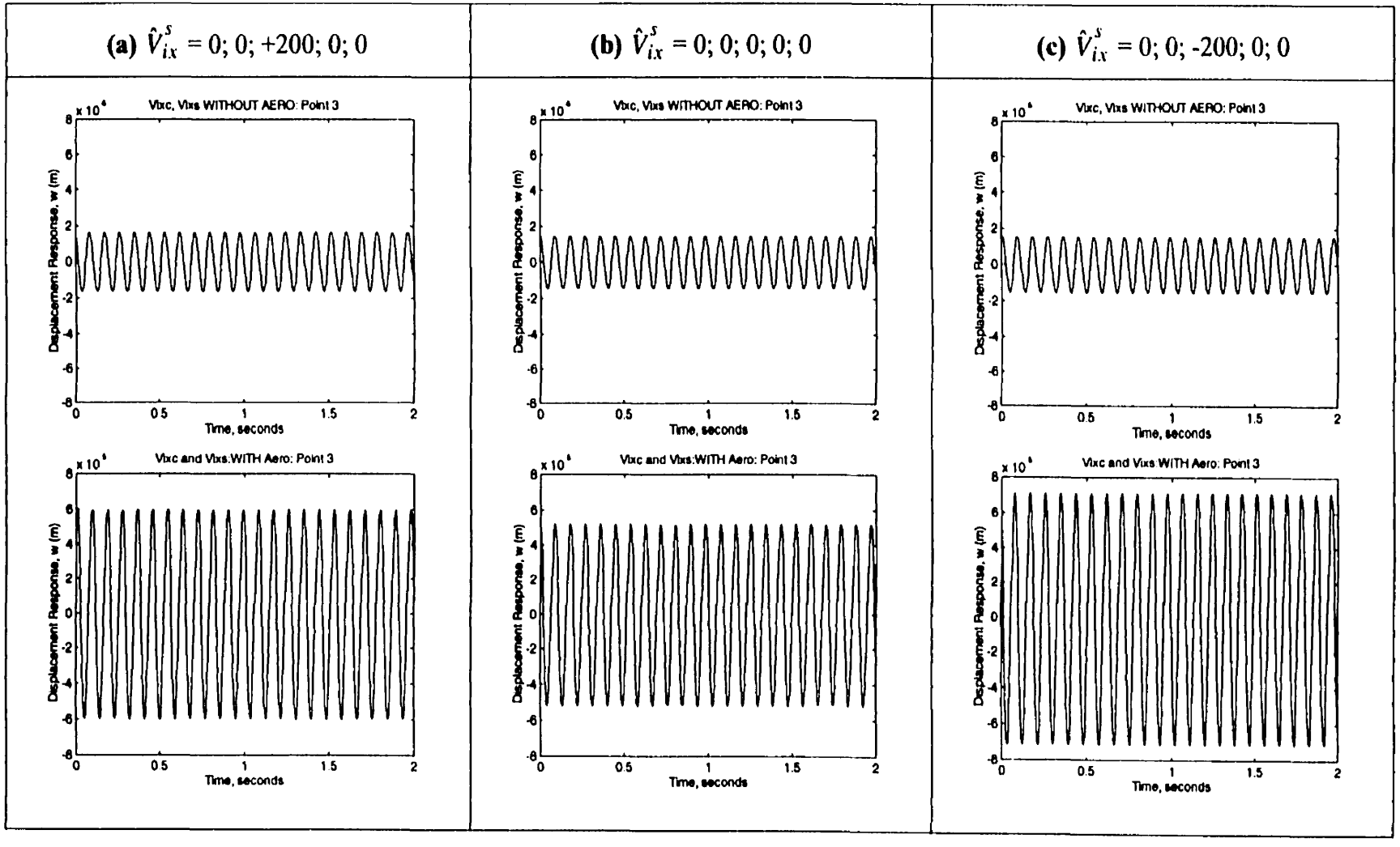

Figure 5.7: Dynamic Response at Point 3: $\hat{V}_{ix}^{c}$ = -500; 0; -400; 0; 0; $\hat{V}_{iy}^{c}$ = 0; 0; 0; 0; 0; $\hat{V}_{iy}^{s}$ = 0; 0; 0; 0; 0

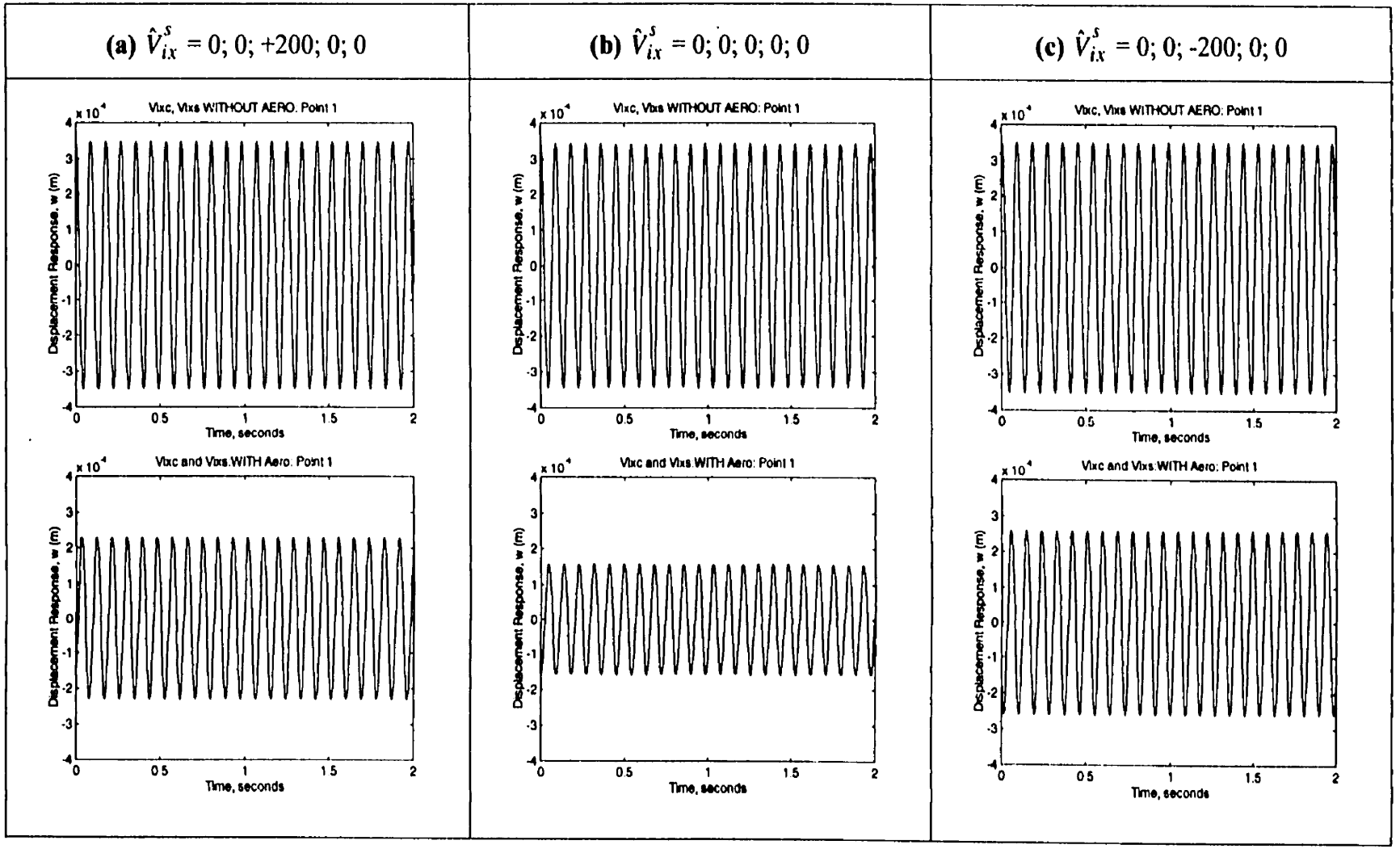

Figure 5.8: Dynamic Response at Point 1: $\hat{V}_{ix}^{c}$ = -500; 0; -600; 0; 0; $\hat{V}_{iy}^{c}$ = 0; 0; 0; 0; 0; $\hat{V}_{iy}^{s}$ = 0; 0; 0; 0; 0

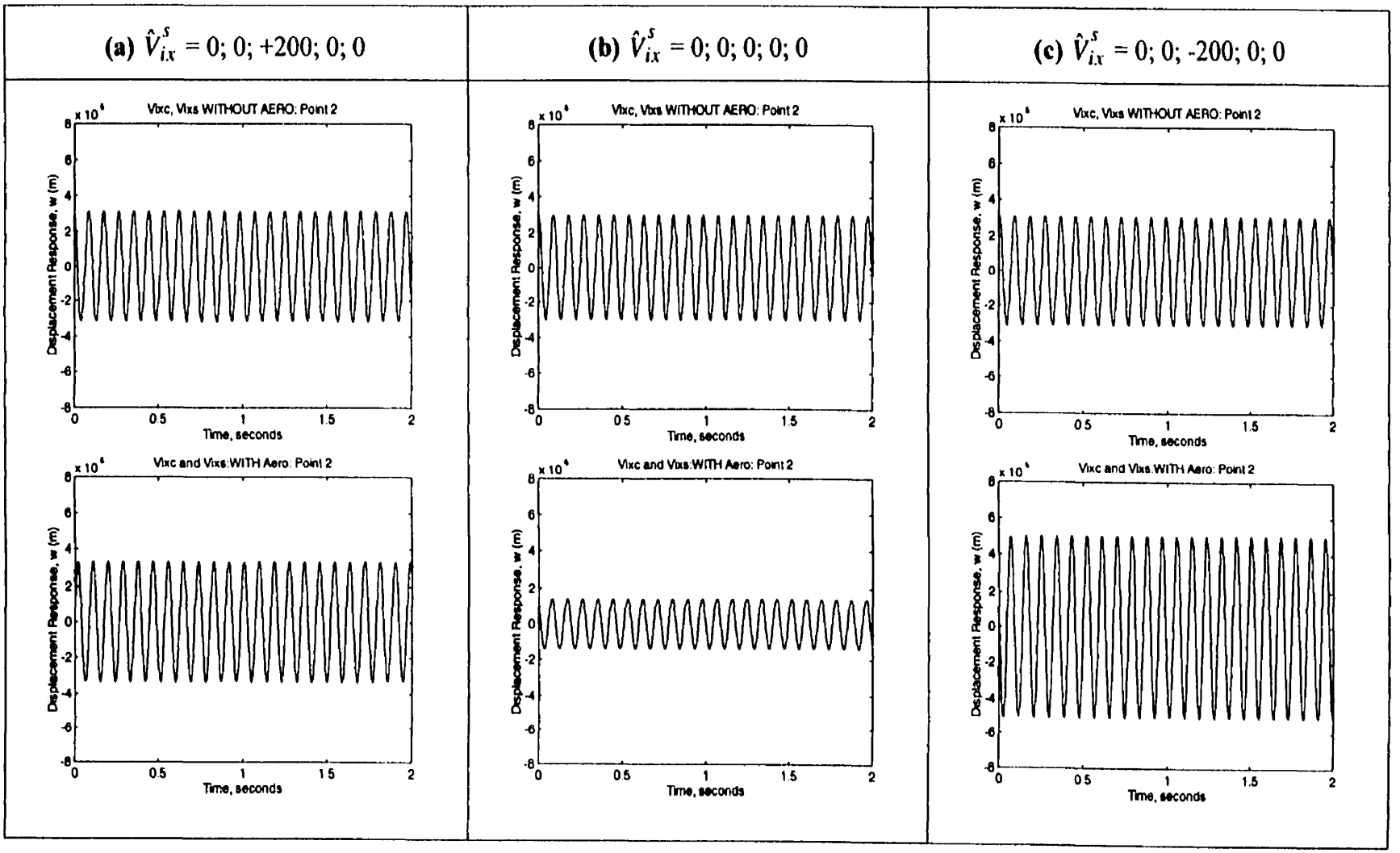

Figure 5.9: Dynamic Response at Point 2: $\hat{V}_{ix}^{c}$ = -500; 0; -600; 0; 0; $\hat{V}_{iy}^{c}$ = 0; 0; 0; 0; 0; $\hat{V}_{iy}^{s}$ = 0; 0; 0; 0; 0

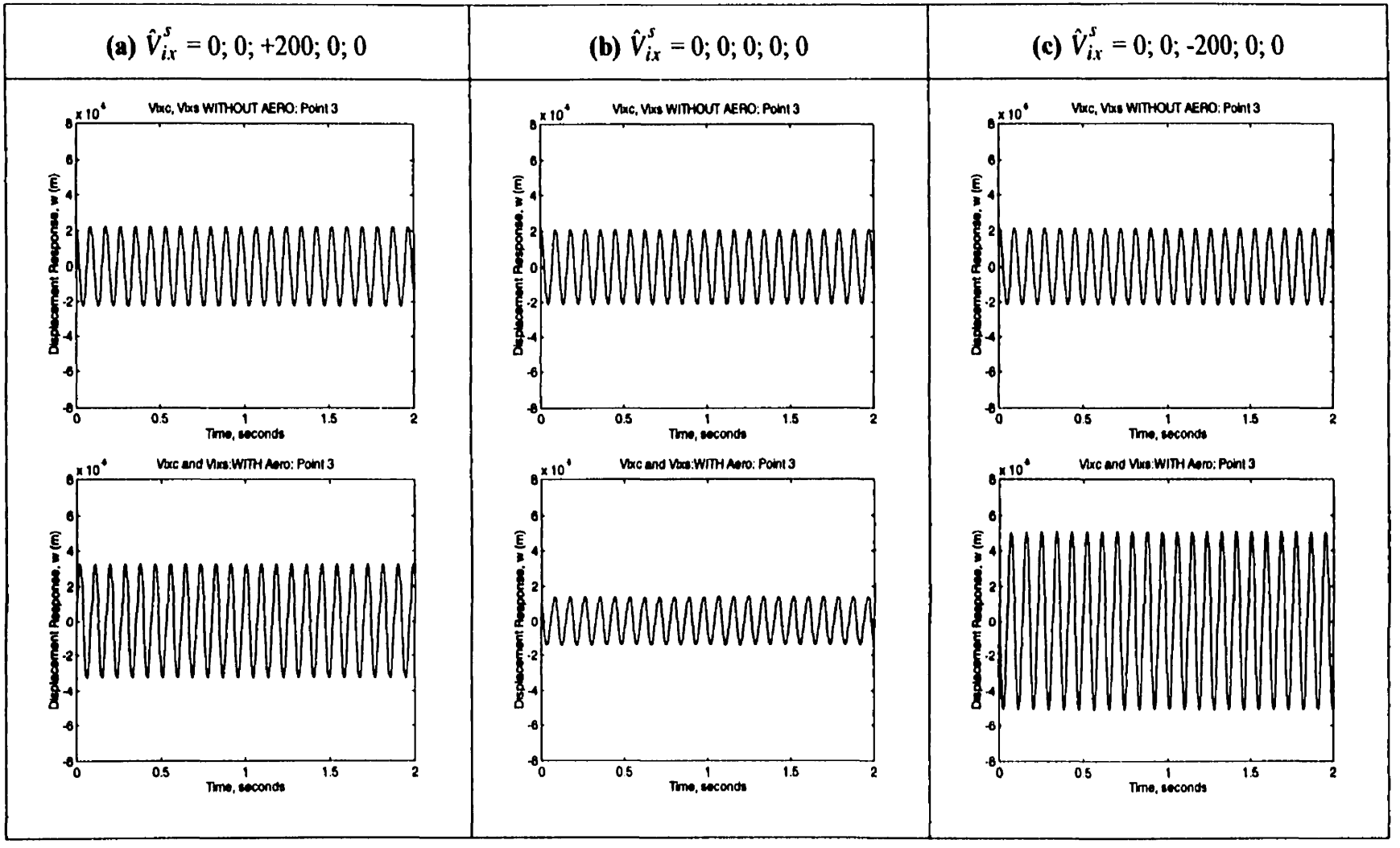

Figure 5.10: Dynamic Response at Point 3: $\hat{V}_{ix}^{c}$ = -500; 0; -600; 0; 0; $\hat{V}_{iy}^{c}$ = 0; 0; 0; 0; 0; $\hat{V}_{iy}^{s}$ = 0; 0; 0; 0; 0

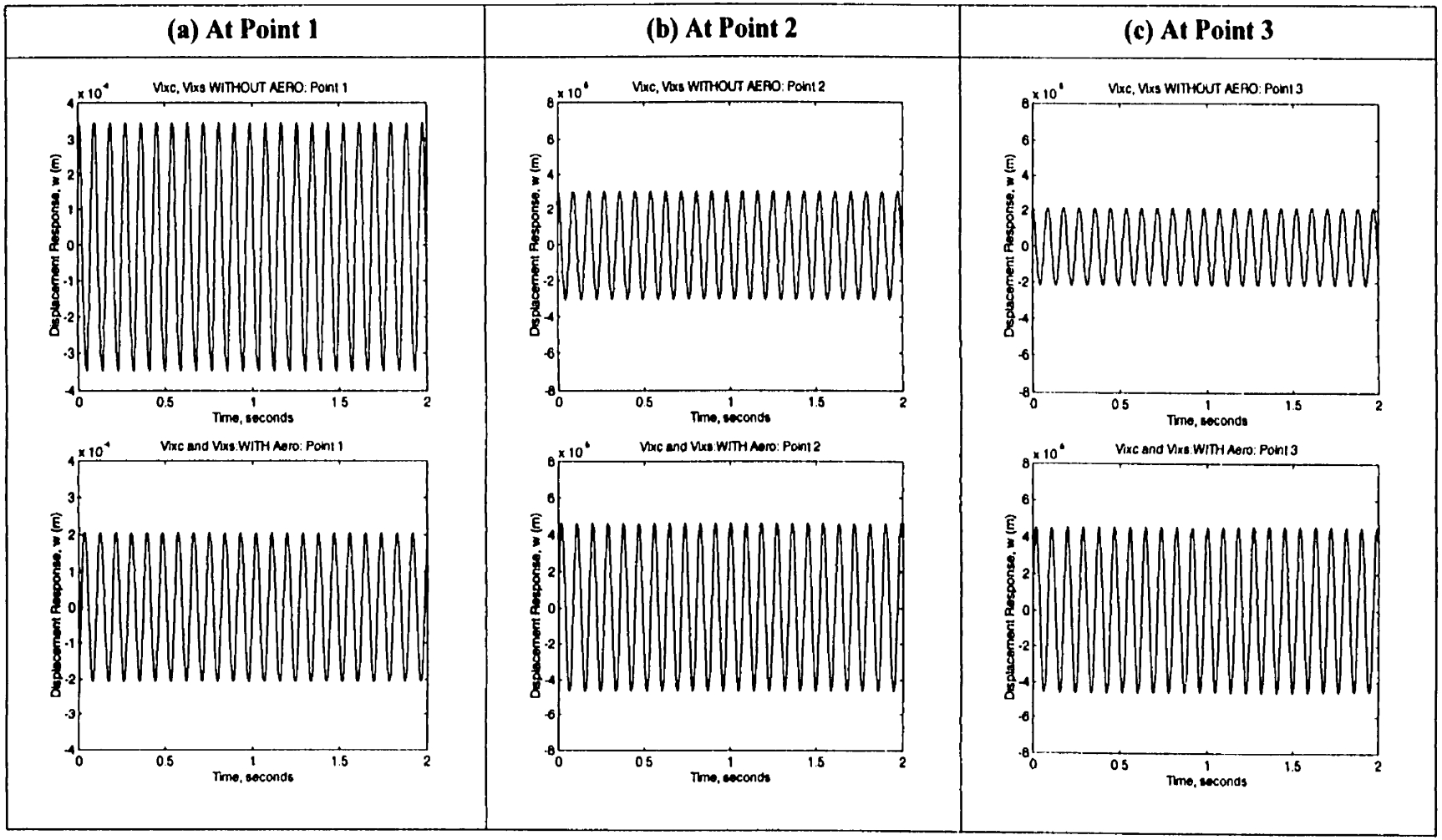

Figure 5.11: Dynamic Response: $\hat{V}_{ix}^{c}$ = -500; 0; -400; 0; 0; $\hat{V}_{ix}^{s}$ = -200; 0; 0; 0; 0; $\hat{V}_{iy}^{c}$ = 0; 0; 0; 0; 0; $\hat{V}_{iy}^{s}$ = 0; 0; 0; 0; 0

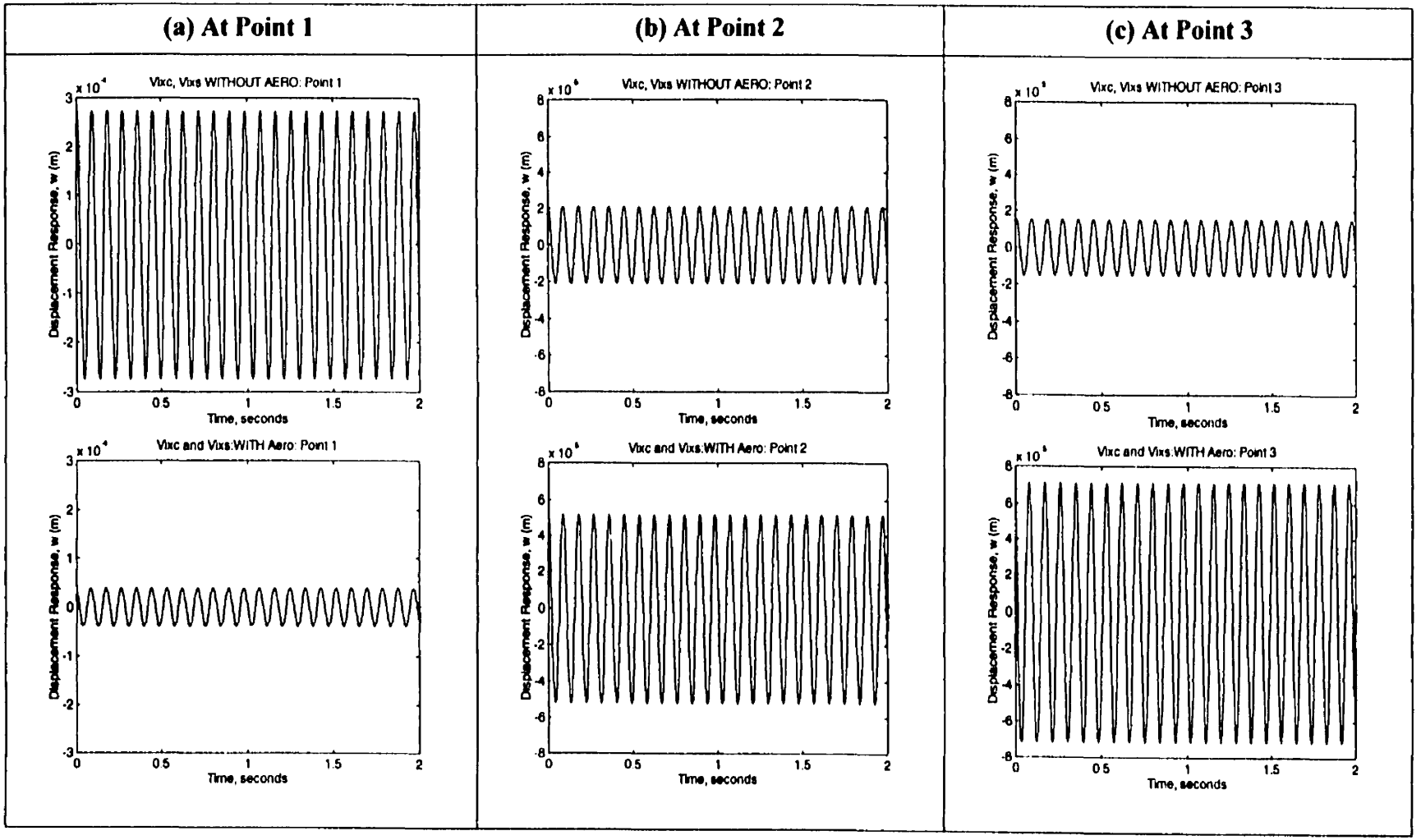

Figure 5.12: Dynamic Response: $\hat{V}_{ix}^{c}$ = -500; 0; -400; 0; 0; $\hat{V}_{ix}^{s}$ = 0; 0; 0; 0; 0; $\hat{V}_{iy}^{c}$ = 0; 0; 0; 0; 0; $\hat{V}_{iy}^{s}$ = 0; 0; 0; 0; 0

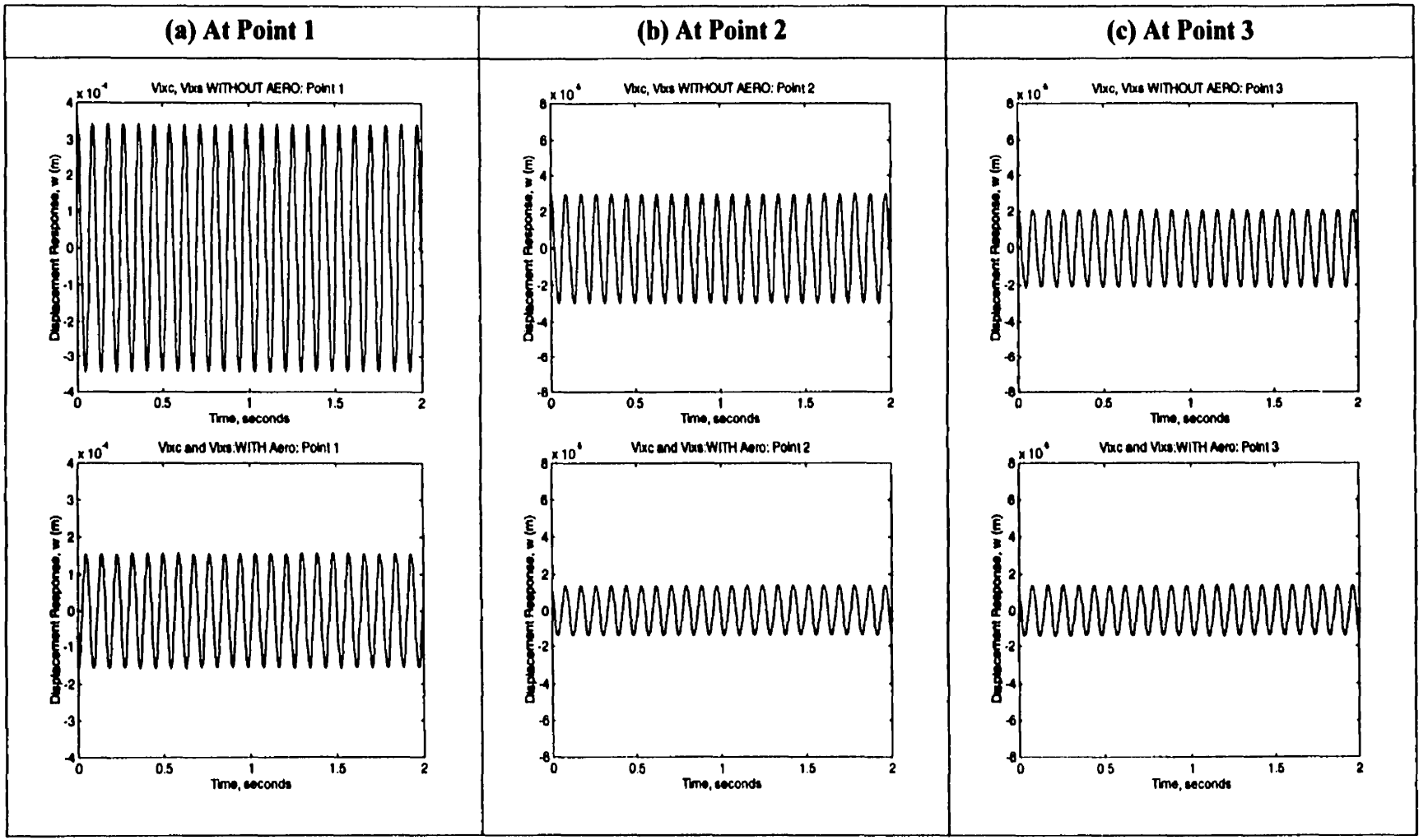

Figure 5.13: Dynamic Response: $\hat{V}_{ix}^{c}$ = -500; 0; -600; 0; 0; $\hat{V}_{ix}^{s}$ = 0; 0; 0; 0; 0; $\hat{V}_{iy}^{c}$ = 0; 0; 0; 0; 0; $\hat{V}_{iy}^{s}$ = 0; 0; 0; 0; 0

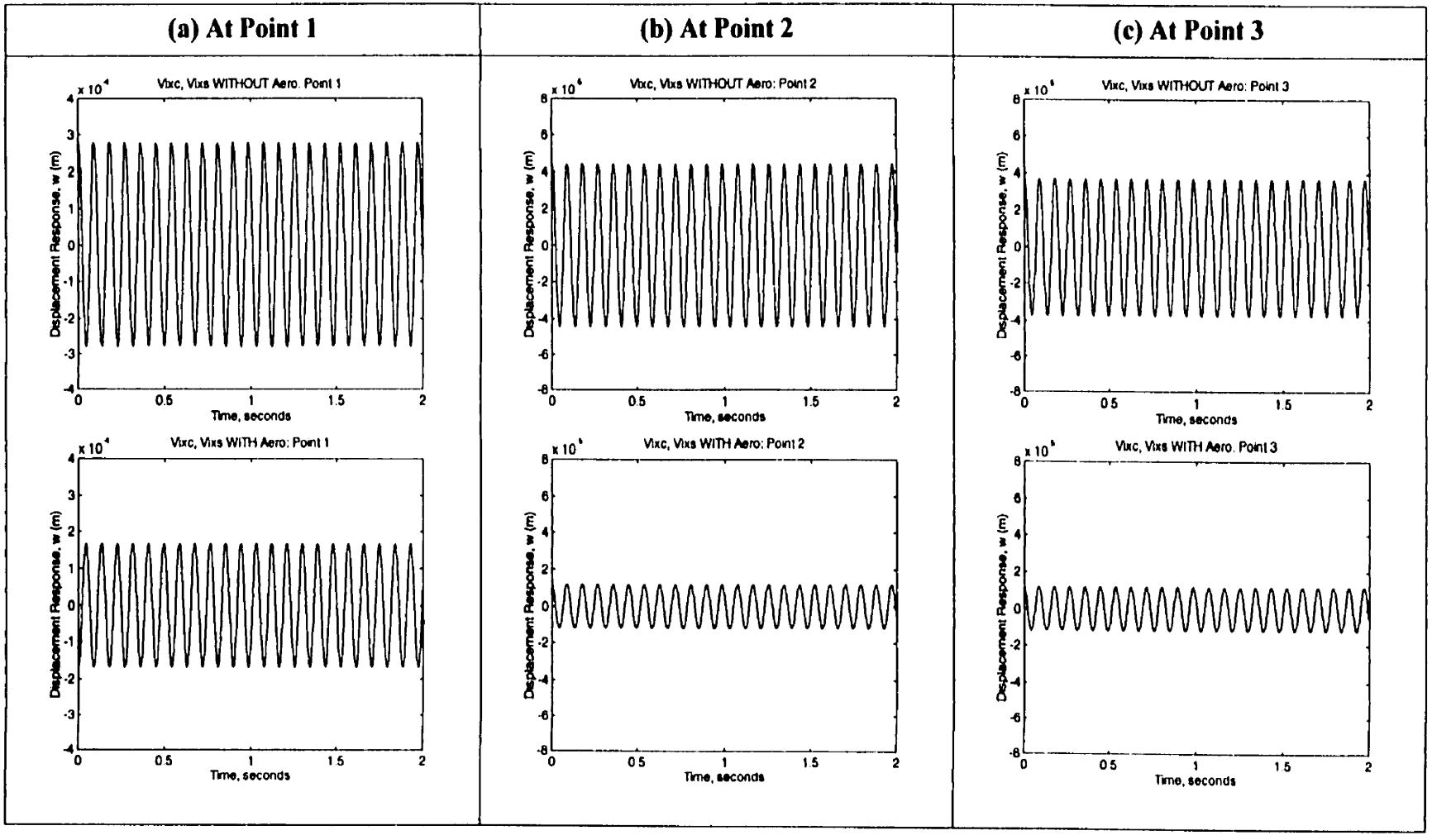

Figure 5.14: Dynamic Response: $\hat{V}_{ix}^{c}$ = -500; 0; -400; 0; -300; $\hat{V}_{ix}^{s}$ = 0; 0; 0; 0; 0; $\hat{V}_{iy}^{c}$ = 0; 0; 0; 0; 0; $\hat{V}_{iy}^{s}$ = 0; 0; 0; 0; 0

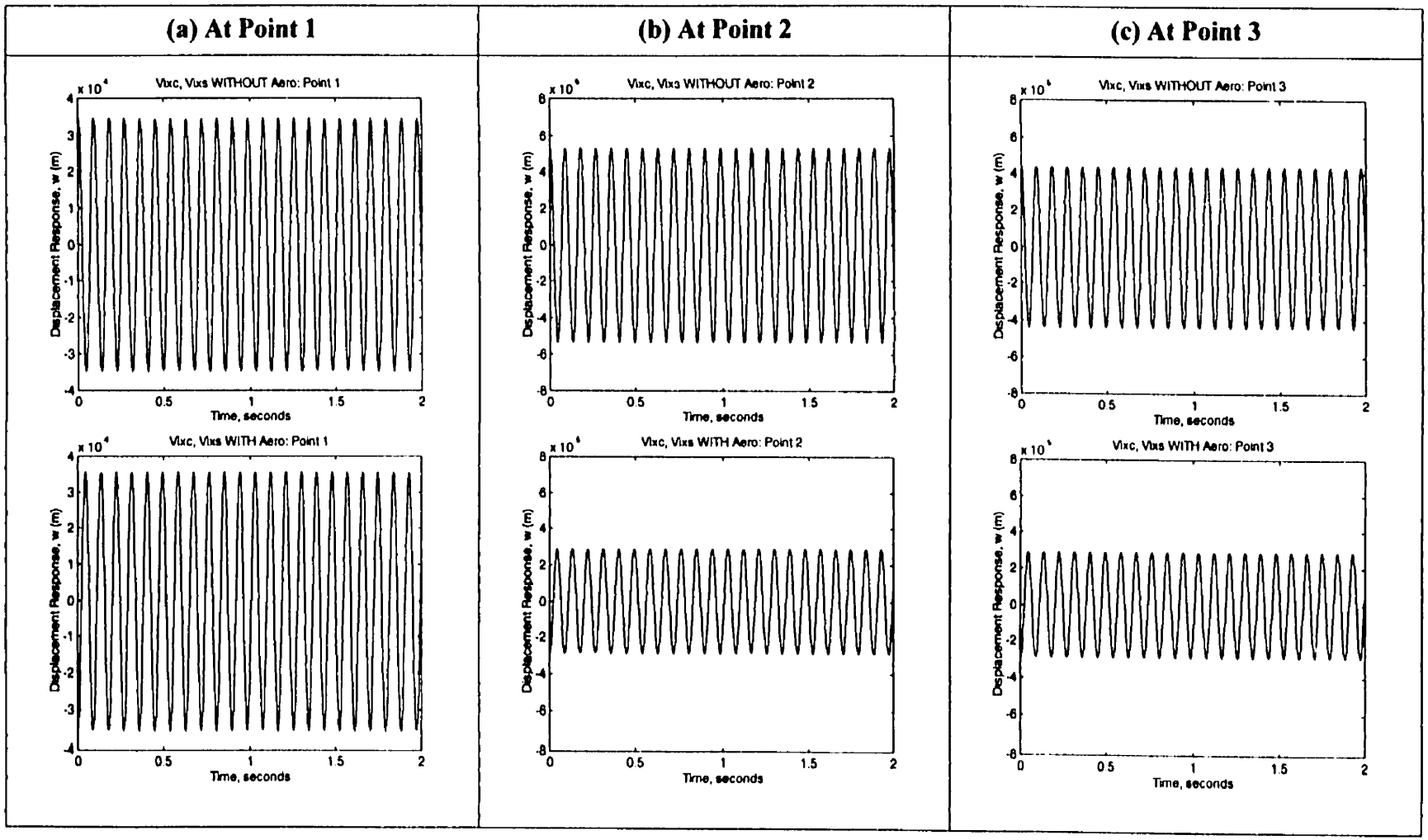

Figure 5.15: Dynamic Response: $\hat{V}_{ix}^{c}$ = -500; 0; -600; 0; -300; $\hat{V}_{ix}^{s}$ = 0; 0; 0; 0; 0; $\hat{V}_{iy}^{c}$ = 0; 0; 0; 0; 0; $\hat{V}_{iy}^{s}$ = 0; 0; 0; 0; 0

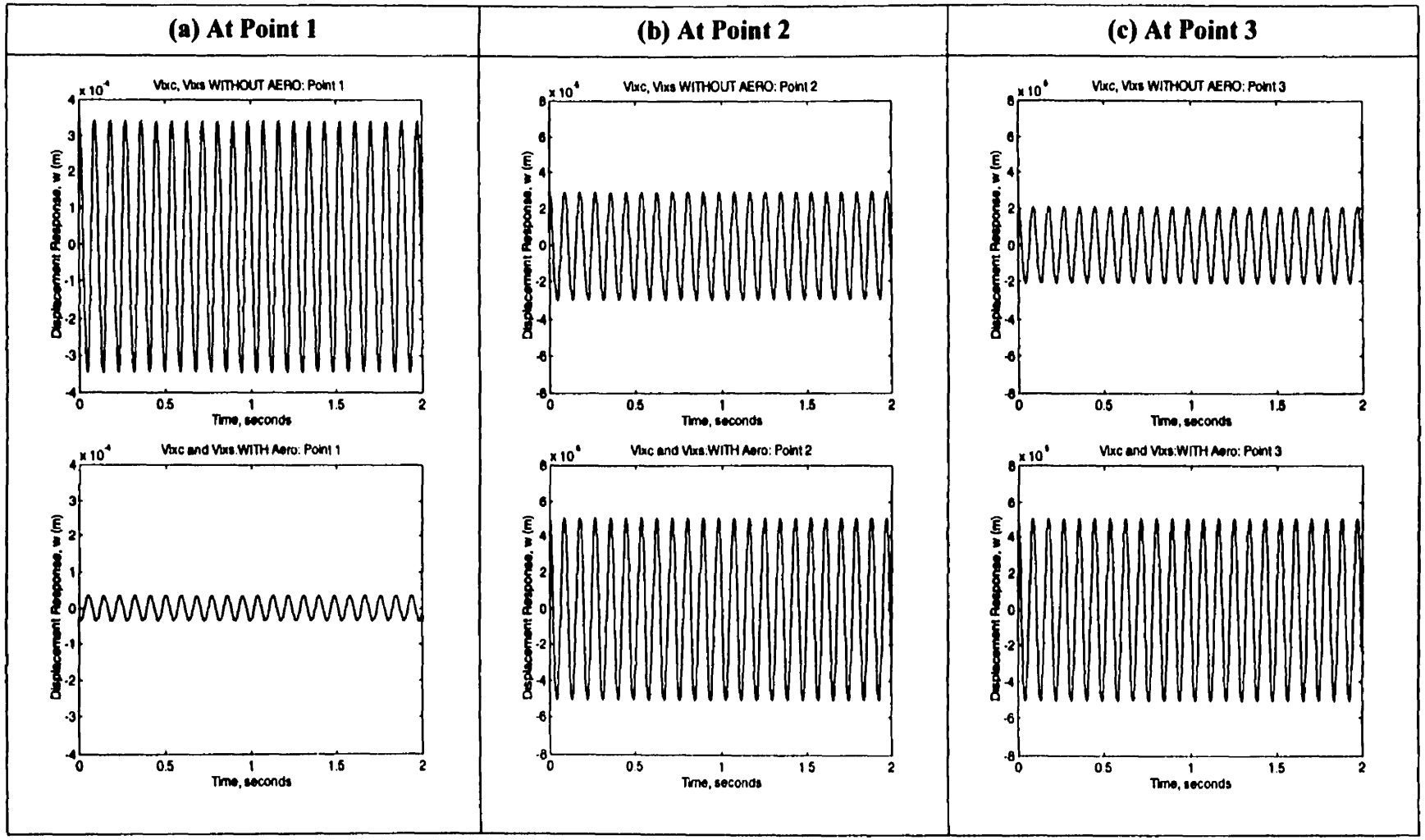

Figure 5.16: Dynamic Response: $\hat{V}_{ix}^{c}$ = -500; 0; -600; 0; 0; $\hat{V}_{ix}^{s}$ = 0; 0; 0; 0; 0; $\hat{V}_{iy}^{c}$ = 0; +100; 0; 0; 0; $\hat{V}_{iy}^{s}$ = 0; 0; 0; 0; 0;

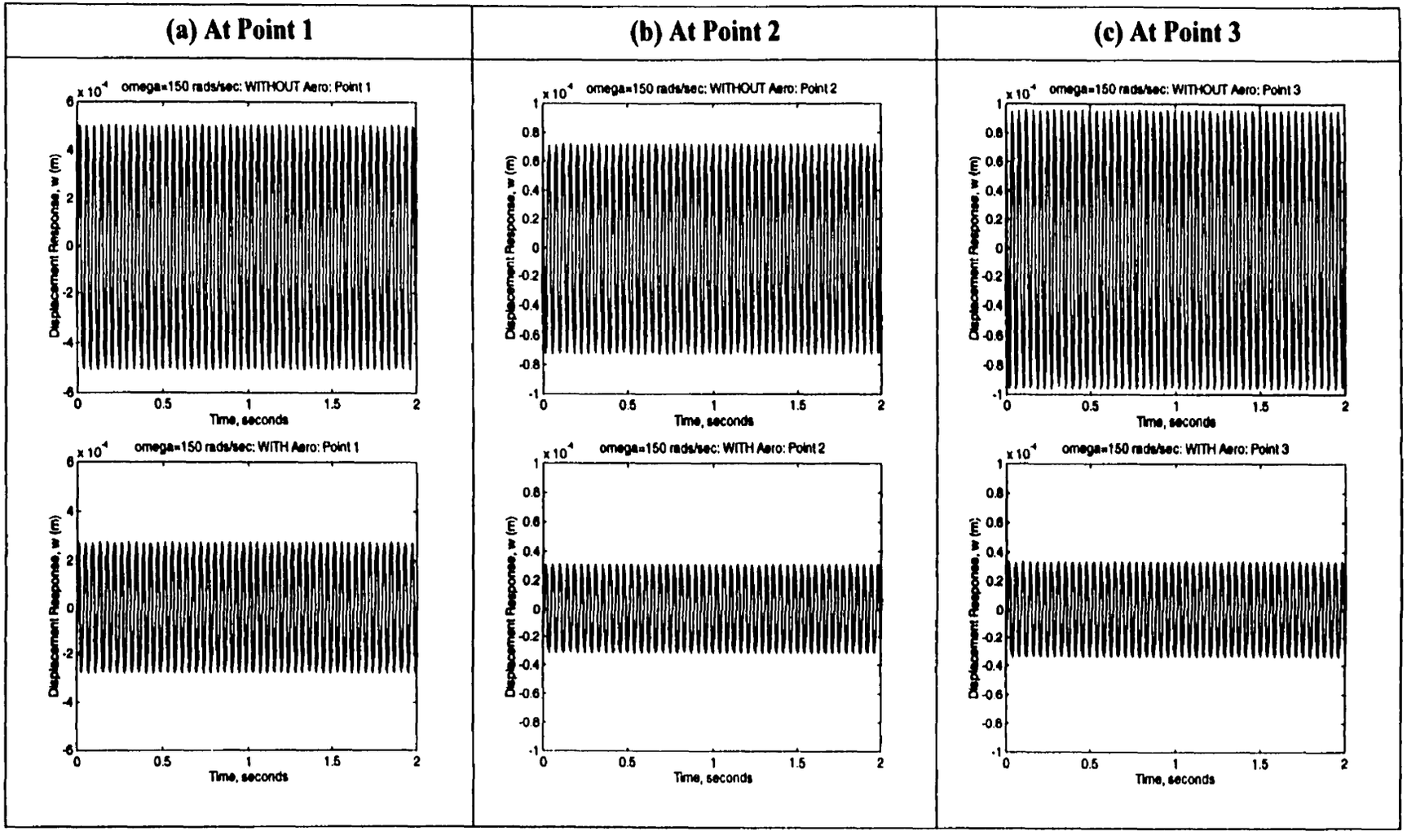

Figure 5.17: For ω = 150 rads/sec and $\hat{V}_{ix}^{c}$ = -500; 0; -400; 0; 0; $\hat{V}_{ix}^{s}$ = 0; 0; 0; 0; 0; $\hat{V}_{iy}^{c}$ = 0; 0; 0; 0; 0; $\hat{V}_{iy}^{s}$ = 0; 0; 0; 0; 0;

Chapter 6

Conclusions and Recommendations for Future Work

A study of the aeroelastic oscillations of a delta wing under unsteady supersonic aerodynamic loading in the presence of bonded piezoelectric strips has been presented in this thesis. The research work involved three major steps: development of an analytical-numerical model for structural analysis; aerodynamic modelling; and study of the system response in the presence of piezoelectric strips, with and without aerodynamic loading.

The natural frequencies for a free delta wing were compared to those published by Andersen (1954) in order to validate the structural dynamics model used in this work. It was found that the agreement between the results was good. In developing the aerodynamic model, a hybrid analytical-numerical method was developed to calculate the unsteady pressure distribution along the delta wing. The results obtained with this new hybrid method were found to be more accurate than those of the *Frequency Expansion* method. The computational efficiency of this hybrid method was found to be superior to that of the numerical methods based on the *Mach Box* approach. When the flow along the wing was made steady, the pressure distribution obtained by this method was a perfect match to that obtained by Carafoli et al. (1969) under the same conditions.

The response of the delta wing at three locations in the presence of piezoelectric strips with and without aerodynamic loading were studied. These strips were activated when an oscillatory voltage was applied across their thicknesses. Both transient and steady state response were obtained for the cases when no aerodynamic loading was present, while only

steady state response was obtained for the aerodynamic loading case under the assumption of small transverse wing displacements in an unsteady supersonic flow.

In the transient case, it was concluded that the wing oscillations damped out faster when the span-aligned piezoelectric strips were present. It was also found that the chord-aligned actuators had little or no effect.

While studying the dynamic response, it was implied that the aerodynamic and piezoelectric effects should oppose each other. In other words, the piezoelectric strips were deemed useful only if the delta wing oscillations were smaller when aerodynamic loading was present as compared to when it was absent. The number of strips and the voltage amplitudes required to achieve this goal were determined by trial and error. It was again concluded that the spanwise strips were more effective than the chordwise strips, which had little or no effect in reducing the amplitude of wing oscillations. Voltage amplitudes of the order of 10^2 volts were adequate to give acceptable reduction in the wing oscillations when aerodynamic loading was present as compared to when it was absent. In certain cases, with appropriate combinations of the piezoelectric strips, the amplitudes of delta wing oscillations were reduced by as much as half when aerodynamic loading was present as compared to when it was absent. It was found that only a small number of strips are needed to reduce the wing oscillations and that increasing the number of piezoelectric strips beyond this number does not produce further reductions. Paige et al. (1993) came to this conclusion as well when they studied square anisotropic panels. Under certain conditions (for the periodic frequency chosen), it was found that some of the piezoelectric combinations were able to reduce the wing oscillations at certain locations on the wing while these combinations were ineffective at other locations. Changing the periodic frequency altered this requirement. Hence, it was also established that changing the periodic frequency of the delta wing alters the response characteristics of the wing at the different locations.

A velocity feedback control scheme was developed in the present thesis for the structural-piezoelectric model. However, no feedback control scheme was developed in the presence of aerodynamic loading. This is because the generalized displacements for control must be

arbitrary functions of time whereas the displacements for the aerodynamics analysis are presently expressed as harmonic functions of time. To develop a control scheme for this case, one has to modify the aerodynamic analysis so that the equations can be expressed as arbitrary functions of time. Alternately, one can numerically expand the generalized aerodynamic forces as rational forces of ω and develop control laws in the *Laplace Transform* domain.

6.1 Recommendations for Future Work

- Modify the aerodynamic analysis to make the transverse displacement an arbitrary function of time so that one can express the structural-aerodynamic-piezoelectric equations of motion as state-space equations. This will enable the development of a feedback control law.

- Use other feedback control schemes, such as the pole-placement technique or LQR, to analyse the response of the delta wing with and without aerodynamic loading.

- Perform flutter analysis of the wing with and without the PVDF strips to see if they are capable of increasing the flutter speed.

- Carry out experiments to validate the analytical findings.

References

Andersen, B. W., 1954, "Vibration of Triangular Cantilever Plates by the Ritz Method", *Journal of Applied Mechanics*, Vol. 21, pp. 365-370.

Bailey, T. and Hubbard, J. E., 1985, "Distributed Piezoelectric-Polymer Active Vibration Control of a Cantilever Beam", *Journal of Guidance, Control, and Dynamics*, Vol. 8, No. 5, pp. 605-611.

Barton, M. V., 1951, "Vibration of Rectangular and Skew Cantilever Plates", *Journal of Applied Mechanics*, Vol. 18, pp. 129-134.

Burke, S. and Hubbard, J. E., 1987, "Active Vibration Control of a Simply-Supported Beam using a Spatially Distributed Actuator", *IEEE Control Systems Magazine*, Vol. 7, No. 6, pp. 25-30.

Carafoli, E., Mateescu, D., and Nastase, A., 1969, *Wing Theory in Supersonic Flow*, 1st Edition, Pergamon Press, Oxford.

Carafoli, E. and Mateescu, D., 1970, "Oscillations of the Wings Fitted with Conical Bodies of Arbitrary Cross-Section in Supersonic Flow", *Revue de Mécanique Appliquée*, No. 4, pp. 899-911.

Chiang, W.-W. and Lee, C.-K., 1989, "Critical Active Damping Control of a Flexible Slender Plate Using a Distributed Modal Actuator and Sensor", *Proceedings of the American Control Conference*, Vol. 1, pp. 700-705.

Chipman, R. R., 1976, "An Improved Mach-Box Approach for the Calculation of Supersonic Oscillatory Pressure Distributions", *Proceedings AIAA/ASME/SAE, 17th Structures, Structural Dynamics, and Materials Conference*, pp. 615-625.

Cowper, G. R., 1973, "Gaussian Quadrature Formulas for Triangles", *International Journal for Numerical Methods in Engineering*, Vol. 7, pp. 405-408.

Crawley, E. F. and de Luis, J., 1987, "Use of Piezoelectric Actuators as Elements of Intelligent Structures", *AIAA Journal*, Vol. 25, No. 10, pp. 1373-1385.

Doe, R. H., 1985, "Linearised Methods in Supersonic Flow", *Unsteady Aerodynamics: Fundamentals and Applications to Aircraft Dynamics*, Neuilly-sur-Seine, France, AGARD, pp. 17-1 to 17-19.

Gradshteyn, I. S. and Ryzhik, I. M., 1994, *Table of Integrals, Series, and Products*, 5th Edition, Academic Press, San Diego.

Gustafson, P. N., Stokey, W. F., and Zorowski, C. F., 1953, "An Experimental Study of Natural Vibrations of Cantilevered Triangular Plates", *Journal of the Aeronautical Sciences*, Vol. 20, pp. 331-337.

Lee, C.-K., Chiang, W.-W., and O'Sullivan, T. C., 1989, "Piezoelectric Modal Sensors and Actuators Achieving Critical Active Damping on a Cantilever Plate", *AIAA/ASME/ASCE/AHS/ASC 30th Structures, Structural Dynamics and Materials Conference*, pp. 2018-2026.

Lin, C. Y., Crawley, E. F., and Heeg, J., 1995, "Open Loop and Preliminary Closed Loop Results of a Strain Actuated Active Aeroelastic Wing", *AIAA/ASME/ASCE/AHS/ASC 36th Structures, Structural Dynamics and Materials Conference*, pp. 1-11.

Mateescu, D., 1969, "Low Frequency Oscillations of the Tail-Body System in Supersonic Flow", *Revue de Mécanique Appliquée*, No. 1, pp. 1225-1244.

Mateescu, D., 1970, "Oscillatory motions of the Polygonal Wings in Supersonic Flow", *Revue de Mécanique Appliquée*, No. 1, pp. 105-129.

Mateescu, D., 1989, *Unsteady Aerodynamics* (*Course Notes*), McGill University, Montréal, Canada.

Meirovitch, L., 1967, *Analytical Methods in Vibration*, MacMillan, New York.

Meirovitch, L., 1975, *Elements of Vibration Analysis*, McGraw-Hill, New York.

Miller, S. E. and Hubbard, J. E., 1988, "Smart Components for Structural Vibration Control", *Proceedings of the American Control Conference*, Vol. 3., pp. 1897-1902.

Nam, C., Kim, Y., and Lee, K.-M., 1996, "Optimal Wing Design for Flutter Suppression with PZT Actuators Including Power Requirement", *6th AIAA/NASA/ISSMO Symposium on Multidisciplinary Analysis and Optimization*, Part 1, Bellevue, WA, pp. 36-46.

Paige, D. A., Scott, R. C., and Weisshaar, T. A., 1993, "Active Control of Composite Panel Flutter Using Piezoelectric Materials", *Proceeding of Smart Structures and Materials, Smart Structures and Intelligent Systems*, Vol. 1917, SPIE, Bellingham, WA, pp. 84-97.

Pines, S., Dugundji, J., and Neuringer, J., 1955, "Aerodynamic Flutter Derivatives for a Flexible Wing with Supersonic and Subsonic Edges", *Journal of the Aeronautical Sciences*, Vol. 22, No. 10, pp. 693-700.

Reddy, J. N., 1993, *Finite Element Method*, 2nd Edition, McGraw-Hill, New York.

Reich, G. W. and Crawley, E. F., 1994, "Design and Modeling of an Active Aeroelastic Wing", SERC Report #4-94, Massachusetts Institute of Technology, Cambridge, MA.

Shen, I. Y., 1994, "Bending-Vibration Control of Composite and Isotropic Plates through Intelligent Constrained-Layer Treatments", *Journal of Smart Materials and Structures*, Vol. 3, pp. 59-70.

Suleman, A. and Venkayya, V. B., 1996, "Flutter Control of an Adaptive Laminated Composite Panel with Piezoelectric Layers", *6th AIAA/NASA/ISSMO Symposium on Multidisciplinary Analysis and Optimization*, Part 1, Bellevue, WA, pp. 141-151.

Van Poppel, J. and Misra, A. K., 1992, "Active Control of Space Structures Using Bonded Piezoelectric Film Actuators", *Proceedings of the AIAA/AAS Astrodynamics Conference*, Hilton Head Island, SC, pp. 328-341.

Venneri, S. L. and Wada, B. K., 1993, "Overview of NASA's Adaptive Structures Program", *44th Congress of the International Astronautical Federation*, Austria, pp. 1-13.

Appendix A

Elements of the Stiffness Matrix: k_{ij}

The elements of the stiffness matrix as defined in Chapter 2, equation (2.22) are k_{ij}. The following gives the expressions of these elements as used in this thesis.

Let the elements of the stiffness matrix be written as

$$k_{ij} = \frac{c}{l^3}\int_0^1\int_0^1 \{k_{ij_1} + k_{ij_2} + k_{ij_3} + k_{ij_4} + k_{ij_5}\}\, d\xi d\eta \tag{A.1}$$

The elements k_{ij} are extracted from the equation for the potential energy given by equation (2.21). To do this we have to start with the non-dimensional transverse displacement given by equation (2.5) which is repeated below

$$w(\xi, \eta, t) = \sum_{r=1}^{M}\sum_{s=1}^{N} \Phi_r(\xi)\Psi_s(\eta)q_{rs}(t) \tag{A.2}$$

where Φ_r and Ψ_s are the shape functions given by equations (2.7) and (2.8) respectively. The transverse displacement is similarly written for the '*kp*' pair. Expanding equation (A.2) in equation (2.21), we get

$$a_1 = \frac{\partial^2 w}{\partial \xi^2} = \frac{\partial^2 \Phi_r}{\partial \xi^2}\Psi_s + 2\frac{\partial \Phi_r}{\partial \xi}\frac{\partial \Psi_s}{\partial \xi} + \Phi_r\frac{\partial^2 \Psi_s}{\partial \xi^2} \tag{A.3}$$

$$a_2 = \frac{\partial w}{\partial \eta} = \Phi_r\frac{\partial \Psi_s}{\partial \eta} \tag{A.4}$$

$$a_3 = \frac{\partial^2 w}{\partial \eta^2} = \Phi_r\frac{\partial^2 \Psi_s}{\partial \eta^2} \tag{A.5}$$

$$a_4 = \frac{\partial^2 w}{\partial \xi \partial \eta} = \frac{\partial \Phi_r}{\partial \xi}\frac{\partial \Psi_s}{\partial \eta} + \Phi_r \frac{\partial^2 \Psi_s}{\partial \xi \partial \eta} \tag{A.6}$$

$$b_1 = \frac{\partial^2 w}{\partial \xi^2} = \frac{\partial^2 \Phi_k}{\partial \xi^2}\Psi_p + 2\frac{\partial \Phi_k}{\partial \xi}\frac{\partial \Psi_p}{\partial \xi} + \Phi_k \frac{\partial^2 \Psi_p}{\partial \xi^2} \tag{A.7}$$

$$b_2 = \frac{\partial w}{\partial \eta} = \Phi_k \frac{\partial \Psi_p}{\partial \eta} \tag{A.8}$$

$$b_3 = \frac{\partial^2 w}{\partial \eta^2} = \Phi_k \frac{\partial^2 \Psi_p}{\partial \eta^2} \tag{A.9}$$

$$b_4 = \frac{\partial^2 w}{\partial \xi \partial \eta} = \frac{\partial \Phi_k}{\partial \xi}\frac{\partial \Psi_p}{\partial \eta} + \Phi_k \frac{\partial^2 \Psi_p}{\partial \xi \partial \eta} \tag{A.10}$$

Substituting equations (A.3) to (A.10) in the equation for potential energy, equation (2.21), the individual components of equation (A.1) can be written as the following:

$$k_{ij_1} = (1-\xi)a_1 b_1 \tag{A.11}$$

$$k_{ij_2} = 4\eta a_1 b_4 \tag{A.12}$$

$$k_{ij_3} = \frac{2}{(1-\xi)}\{[2\eta^2 + k^2(1-\nu)]a_4 b_4 + (\eta^2 + \nu k^2)a_1 b_3 + 2\eta a_1 b_2\} \tag{A.13}$$

$$k_{ij_4} = \frac{4}{(1-\xi)^2}\{[2\eta^2 + k^2(1-\nu)]a_2 b_4 + (\eta^3 + k^2\eta)a_3 b_4\} \tag{A.14}$$

$$k_{ij_5} = \frac{1}{(1-\xi)^3}\{2[2\eta^2 + k^2(1-\nu)]a_2 b_2 + 4(\eta^3 + (1-\nu)k^2\eta)a_2 b_3 + (\eta^4 + k^4 + 2(1-\nu)k^2\eta^2)a_3 b_3\} \tag{A.15}$$

Equations (A.11) to (A.15) are substituted into equation (A.1) to obtain k_{ij}.

Appendix B

Aerodynamic Model Details

This appendix contains additional details and results pertaining to the Aerodynamic Model.

B.1 Limits of Integration Inside the Mach Cone-Derivation of Equation (3.34)

Please refer to Figure 3.2. Let us start from the coordinate transformation which is given as

$$X = x_1 - x_{1s}$$

$$Y = \frac{x_2 - x_{2s}}{x_1 - x_{1s}}$$

As seen in the figure, (x_1, x_2) is the receiving point and (x_{1s}, x_{2s}) is the source point.

Now from equation (3.2),

$$y = \frac{x_2}{x_1}$$

and hence,

$$y_s = \frac{x_{2s}}{x_{1s}}$$

Substituting in Y we get,

$$Y = \frac{x_1 y - x_{1s} y_s}{x_1 - x_{1s}}$$

Solving for x_{1s} we get,

$$x_{1s} = x_1 \frac{y - Y}{y_s - Y}$$

Substituting in X we get,

$$X = x_1 - x_{1s} = x_1 \frac{y_s - y}{y_s - Y}$$

But on line OA_1 of Figure 3.2:

$$y_s = \frac{x_{2s}}{x_{1s}} = l$$

Hence,

$$X_1 = x_1 \frac{l - y}{l - Y}$$

Similarly on line OA_2:

$$X_2 = x_1 \frac{l + y}{l + Y}$$

This completes the derivation of equation (3.34).

B.2 Results of Chapter 3 (Section 3.3) in Tabular Format

Tables B.1 to B.3 list the numeric results which were presented graphically in Chapter 3 (Section 3.3) for the Delta Wing under steady and unsteady flow. These results compare the pressure distributions found using the *Present Method* and the method developed by Carafoli et al.(1969). The values in Tables B.1 to B.3 were used to produce Figures 3.3 to 3.5 respectively.

B.3 Coefficients $A_{mh,\,np}$ and $B_{ki,\,mp}$ and their Derivatives

Tables B.4 to B.7 list the coefficients $A_{mh,\,np}$ and $B_{ki,\,mp}$ and their derivatives respectively for the modes $r = 1$, $r = 2$, $s = 1$ and $s = 2$ as derived in Chapter 3.

Table B.1: Comparison of u and C_p : Steady Flow

$y = \frac{x_2}{x_1}$	*Present Method* u or $\frac{\partial \varphi}{\partial x_1}$	Carafoli et al. u or $\frac{\partial \varphi}{\partial x_1}$	*Present Method* Imaginary C_p	Carafoli et al. Imaginary C_p
-0.8	-.574980D+00	-.574980D+00	.114996D+01	.114996D+01
-0.6	-.460067D+00	-.460067D+00	.920176D+00	.920176D+00
-0.4	-.388353D+00	-.388353D+00	.776750D+00	.776750D+00
-0.2	-.348466D+00	-.348466D+00	.696932D+00	.696932D+00
0.0	-.335626D+00	-.335626D+00	.671252D+00	.671252D+00
0.2	-.348466D+00	-.348466D+00	.696932D+00	.696932D+00
0.4	-.388353D+00	-.388353D+00	.776750D+00	.776750D+00
0.6	-.460067D+00	-.460067D+00	.920176D+00	.920176D+00
0.8	-.574980D+00	-.574980D+00	.114996D+01	.114996D+01

Table B.2: Comparison of $\hat{u}$: Unsteady Flow

$y = \frac{x_2}{x_1}$	*Present Method* $\hat{u}$ or $\frac{\partial \hat{\varphi}}{\partial x_1}$	*Frequency Expansion* $\hat{u}$ or $\frac{\partial \hat{\varphi}}{\partial x_1}$
-0.8	-.909563D+00	-.909563D+00
-0.6	-.836628D+00	-.836628D+00
-0.4	-.796929D+00	-.796929D+00
-0.2	-.776264D+00	-.776264D+00
0.0	-.769800D+00	-.769800D+00
0.2	-.776264D+00	-.776264D+00
0.4	-.796929D+00	-.796929D+00
0.6	-.836628D+00	-.836628D+00
0.8	-.909563D+00	-.909563D+00

Table B.3: Comparison of $\hat{C}_p$: Unsteady Flow

$y = \frac{x_2}{x_1}$	*Present Method* Real $\hat{C}_p$	*Present Method* Imaginary $\hat{C}_p$	*Frequency Expansion* Imaginary $\hat{C}_p$
-0.8	-.115130D-03	.672151D-02	.756656D-02
-0.6	-.100685D-03	.641814D-02	.695983D-02
-0.4	-.915219D-04	.625307D-02	.662957D-02
-0.2	-.863804D-04	.616727D-02	.645767D-02
0.0	-.847247D-04	.614060D-02	.640389D-02
0.2	-.863804D-04	.616727D-02	.645767D-02
0.4	-.915219D-04	.625307D-02	.662957D-02
0.6	-.100685D-03	.641814D-02	.695983D-02
0.8	-.115130D-03	.672151D-02	.756656D-02

Table B.4: For $r = 1$: Coefficient $A_{mh,\,np}$ and its Derivatives

mh	*np*	$A_{mh,\,np}$	$\frac{\partial A_{mh,\,np}}{\partial x_1}$	$\frac{\partial^2 A_{mh,\,np}}{\partial x_1^2}$
0	0	$(x_1 y/l)^2$	0	0
1	0	0	0	0
2	0	0	0	0
0	1	0	0	0
1	1	$-2x_1 y/l^2$	0	0
2	1	0	0	0
0	2	0	0	0
1	2	0	0	0
2	2	$1/l^2$	0	0

Table B.5: For $r = 2$: Coefficient $A_{mh,\,np}$ and its Derivatives

mh	np	$A_{mh,\,np}$	$\frac{\partial A_{mh,\,np}}{\partial x_1}$	$\frac{\partial^2 A_{mh,\,np}}{\partial x_1^2}$
0	0	$(x_1 y/l)^3$	0	0
1	0	0	0	0
2	0	0	0	0
3	0	0	0	0
0	1	0	0	0
1	1	$-3(x_1 y)^2/l^3$	0	0
2	1	0	0	0
3	1	0	0	0
0	2	0	0	0
1	2	0	0	0
2	2	$3x_1 y/l^3$	0	0
3	2	0	0	0
0	3	0	0	0
1	3	0	0	0
2	3	0	0	0
3	3	$-1/l^3$	0	0

Table B.6: For $s = 1$: Coefficient $B_{ki,\,mp}$ and its Derivatives

ki	mp	$B_{ki,\,mp}$	$\frac{\partial B_{ki,\,mp}}{\partial x_1}$	$\frac{\partial^2 B_{ki,\,mp}}{\partial x_1^2}$
0	0	1	0	0
1	0	0	0	0
0	1	0	0	0
1	1	0	0	0

Table B.7: For $s = 2$: Coefficient $B_{ki,\,mp}$ and its Derivatives

ki	mp	$B_{ki,\,mp}$	$\frac{\partial B_{ki,\,mp}}{\partial x_1}$	$\frac{\partial^2 B_{ki,\,mp}}{\partial x_1^2}$
0	0	$(-l^2c + cx_1^2y^2 + 2l^2x_1 - 2lx_1^2y)$ $/2cl^2$	$(l-x_2)/cl$	0
1	0	$(x_1y - l)/cl$	0	0
2	0	0	0	0
0	1	0	0	0
1	1	$x_1(l-cy)/cl^2$	$1/cl$	0
2	1	$-1/cl$	0	0
0	2	0	0	0
1	2	0	0	0
2	2	$1/2l^2$	0	0

B.4 Derivatives of I_1, I_2, I_3, and I_4

The derivatives listed below are supplemental to the derivation for the reduced velocity presented in section 3.4 for inside the Mach cone.

$$\frac{\partial I_1}{\partial x_1} = \{x_1(l-y)\}^{mhk-mj-1} \int_{\frac{1}{B}}^{y} \left\{ \frac{Y^{mhp}}{(l-Y)^{mhk-mj}} \left[l(mhk-mj)\left(\frac{\sin A_1}{a^{mj+1}} + \frac{\sin A_2}{b^{mj+1}} \right) + \frac{lx_1(l-y)}{(l-Y)}\left(\frac{\cos A_1}{a^{mj}} + \frac{\cos A_2}{b^{mj}} \right) \right] - b_1 \right\} \frac{dY}{\bar{R}} + b_1 Q_1 \tag{B.1a}$$

$$\frac{\partial I_2}{\partial x_1} = \{x_1(l-y)\}^{mhk-mj-1} \int_{y}^{\frac{1}{\bar{B}}} \left\{ \frac{Y^{mhp}}{(l-Y)^{mhk-mj}} \left[l(mhk-mj)\left(\frac{\sin A_3}{a^{mj+1}} + \frac{\sin A_4}{b^{mj+1}} \right) + \frac{lx_1(l+y)}{(l+Y)}\left(\frac{\cos A_3}{a^{mj}} + \frac{\cos A_4}{b^{mj}} \right) \right] - b_2 \right\} \frac{dY}{\bar{R}} + b_2 Q_2 \tag{B.1b}$$

$$\frac{\partial I_3}{\partial x_1} = -\{x_1(l-y)\}^{mhk-mj-1}\int_{\frac{1}{B}}^{y}\left\{\frac{Y^{mhp}}{(l-Y)^{mhk-mj}}\left[l(mhk-mj)\left(\frac{\cos A_1}{a^{mj+1}} + \frac{\cos A_2}{b^{mj+1}}\right) - \frac{lx_1(l-y)}{(l-Y)}\left(\frac{\sin A_1}{a^{mj}} + \frac{\sin A_2}{b^{mj}}\right)\right] - b_3\right\}\frac{dY}{\bar{R}} + b_3 Q_1 \tag{B.1c}$$

$$\frac{\partial I_4}{\partial x_1} = -\{x_1(l-y)\}^{mhk-mj-1}\int_{y}^{\frac{1}{B}}\left\{\frac{Y^{mhp}}{(l-Y)^{mhk-mj}}\left[l(mhk-mj)\left(\frac{\cos A_3}{a^{mj+1}} + \frac{\cos A_4}{b^{mj+1}}\right) + \frac{lx_1(l+y)}{(l+Y)}\left(\frac{\sin A_1}{a^{mj}} + \frac{\sin A_2}{b^{mj}}\right)\right] - b_4\right\}\frac{dY}{\bar{R}} + b_4 Q_2 \tag{B.1d}$$

where A_1, A_2, A_3 and A_4 are given by equation (3.82), and Q_1 and Q_2 are given by equation (3.85). Also,

$$b_1 = \frac{2}{k^{mj}}\left(-\frac{1}{B}\right)^{mhp}\left(\frac{B}{Bl+1}\right)^{mhk-mj}\left\{\frac{l}{k}(mhk-mj)\sin\left(\frac{Bkx_1(l-y)}{Bl+1} + \frac{mj\pi}{2}\right) + \frac{Bkx_1(l-y)}{Bl+1}\cos\left(\frac{Bkx_1(l-y)}{Bl+1} + \frac{mj\pi}{2}\right)\right\} \tag{B.2a}$$

$$b_2 = \frac{2}{k^{mj}}\left(\frac{1}{B}\right)^{mhp}\left(\frac{B}{Bl+1}\right)^{mhk-mj}\left\{\frac{l}{k}(mhk-mj)\sin\left(\frac{Bkx_1(l+y)}{Bl+1} + \frac{mj\pi}{2}\right) + \frac{Bklx_1(l+y)}{Bl+1}\cos\left(\frac{Bkx_1(l+y)}{Bl+1} + \frac{mj\pi}{2}\right)\right\} \tag{B.2b}$$

$$b_3 = \frac{2}{k^{mj}}\left(-\frac{1}{B}\right)^{mhp}\left(\frac{B}{Bl+1}\right)^{mhk-mj}\left\{\frac{l}{k}(mhk-mj)\cos\left(\frac{Bkx_1(l-y)}{Bl+1} + \frac{mj\pi}{2}\right) - \frac{Bkx_1(l-y)}{Bl+1}\sin\left(\frac{Bkx_1(l-y)}{Bl+1} + \frac{mj\pi}{2}\right)\right\} \tag{B.2c}$$

$$b_4 = \frac{2}{k^{mj}}\left(\frac{1}{B}\right)^{mhp}\left(\frac{B}{Bl+1}\right)^{mhk-mj}\left\{\frac{l}{k}(mhk-mj)\cos\left(\frac{Bkx_1(l+y)}{Bl+1}+\frac{mj\pi}{2}\right)\right. \qquad \text{(B.2d)}$$
$$\left. -\frac{Bkx_1(l+y)}{Bl+1}\sin\left(\frac{Bkx_1(l+y)}{Bl+1}+\frac{mj\pi}{2}\right)\right\}$$

B.5 Derivatives of I_{11} and I_{12}

The derivatives listed below are supplemental to the derivation for the reduced velocity presented in section 3.4 for outside the Mach cone.

$$\frac{\partial I_{11}}{\partial x_1} = \{x_1(l-y)\}^{mhk-mj-1}\int_{-\frac{1}{B}}^{\frac{1}{B}}\left\{\frac{Y^{mhp}}{(l-Y)^{mhk-mj}}\left[l(mhk-mj)\left(\frac{\sin A_1}{a^{mj+1}}\right.\right.\right. \qquad \text{(B.3a)}$$
$$\left.\left.\left. +\frac{\sin A_2}{b^{mj+1}}\right)+\frac{lx_1(l-y)}{(l-Y)}\left(\frac{\cos A_1}{a^{mj}}+\frac{\cos A_2}{b^{mj}}\right)\right]-b_1-b_5\right\}\frac{dY}{\bar{R}}$$
$$+(b_1+b_5)\pi$$

$$\frac{\partial I_{12}}{\partial x_1} = -\{x_1(l-y)\}^{mhk-mj-1}\int_{-\frac{1}{B}}^{\frac{1}{B}}\left\{\frac{Y^{mhp}}{(l-Y)^{mhk-mj}}\left[l(mhk-mj)\left(\frac{\cos A_1}{a^{mj+1}}\right.\right.\right. \qquad \text{(B.3b)}$$
$$\left.\left.\left. +\frac{\cos A_2}{b^{mj+1}}\right)-\frac{lx_1(l-y)}{(l-Y)}\left(\frac{\sin A_1}{a^{mj}}+\frac{\sin A_2}{b^{mj}}\right)\right]-b_3-b_6\right\}\frac{dY}{\bar{R}}$$
$$+(b_3+b_6)\pi$$

where b_1 and b_3 are given by equations (B.2a) and (B.2c) respectively, and

$$b_5 = \frac{2}{k^{mj}}\left(\frac{1}{B}\right)^{mhp}\left(\frac{B}{Bl-1}\right)^{mhk-mj}\left\{\frac{l}{k}(mhk-mj)\sin\left(\frac{Bkx_1(l-y)}{Bl-1}+\frac{mj\pi}{2}\right)\right. \tag{B.4a}$$
$$\left. + \frac{Bkx_1(l-y)}{Bl-1}\cos\left(\frac{Bkx_1(l-y)}{Bl-1}+\frac{mj\pi}{2}\right)\right\}$$

$$b_6 = \frac{2}{k^{mj}}\left(\frac{1}{B}\right)^{mhp}\left(\frac{B}{Bl-1}\right)^{mhk-mj}\left\{\frac{l}{k}(mhk-mj)\cos\left(\frac{Bkx_1(l-y)}{Bl-1}+\frac{mj\pi}{2}\right)\right. \tag{B.4b}$$
$$\left. - \frac{Bkx_1(l-y)}{Bl-1}\sin\left(\frac{Bkx_1(l-y)}{Bl-1}+\frac{mj\pi}{2}\right)\right\}$$

Appendix C

Locations and Sizes of the Bonded Piezoelectric Strips

The following is a listing of the piezoelectric strip data used to generate the $[P_x]$ and $[P_y]$ matrices derived in Chapter 4. It describes the polarization direction, location and dimensions of the ith piezoelectric strip.

Table C.1: Polarization, Location, and Size of the Bonded Piezoelectric Strips

Strip no.	Polarization along	Location of bottom left corner of strip		Length of strip	
				x-direction	y-direction
		x_i	y_i	a_i	b_i
1	x-direction	0.1	0.1	0.3	0.1
2	y-direction	0.1	0.5	0.1	0.3
3	x-direction	0.5	0.4	0.3	0.1
4	y-direction	0.7	0.1	0.1	0.2
5	x-direction	1.10	0.1	0.3	0.1